Title

Application of the Material Point Method to the Stability and Runout Analysis of Vegetated Slopes

ISBN

9798190900941

Author

Aldakhil, Sultan

Publication Date

2026-09-02

Peer reviewed|Thesis/dissertation

UNIVERSITY OF CALIFORNIA

Los Angeles

Application of the Material Point Method to the Stability and Runout Analysis of Vegetated Slopes

A dissertation submitted in partial satisfaction of the requirements
for the degree Doctor of Philosophy in Civil Engineering

by

Sultan Khalid Aldakhil

2026

ABSTRACT OF THE DISSERTATION

Application of the Material Point Method to the Stability and Runout Analysis of Vegetated Slopes

by

Sultan Khalid Aldakhil
Doctor of Philosophy in Civil Engineering
University of California, Los Angeles, 2026
Professor Ertugrul Taciroglu, Chair

Slope failures cause severe human and economic losses worldwide, yet conventional stability methods describe them only up to the onset of failure. Limit equilibrium methods treat the failing mass as rigid and perfectly plastic, and the finite element method is restricted to small deformations, so neither follows the slide once it forms. The Material Point Method (MPM) avoids this limitation by discretizing soil into Lagrangian material points that move through a fixed background mesh, so no mesh distortion develops under large deformation. This dissertation applies MPM to the analysis of slope failures in two parts, the assessment of slope stability and the influence of vegetation on rainfall-induced failures. The one-phase and coupled two-phase formulations are first derived and verified against classical benchmark problems in poromechanics.

Next, MPM is applied to evaluate the stability of slopes using the strength reduction technique. For dry and unsaturated slopes, slip surfaces agree with finite element solutions and factors of safety differ by less than about 10%, reflecting the different criteria by which each method identifies failure. Unlike mesh-based methods, MPM continues past the onset of failure and captures the post-failure runout.

The effect of root reinforcement is then investigated. A multiple-hardening constitutive model for root-reinforced soil is implemented within the coupled formulation and validated against triaxial tests. Comparative analyses of bare and vegetated slopes under rainfall show that roots delay the initiation of failure, roughly halve the displacement, and change a retrogressive slide into the movement of a single block, although they do not prevent failure under continued rainfall.

Finally, the method is validated against a documented centrifuge slope test. The simulation reproduces the observed retrogressive block failure and the measured pore pressures at failure, and a rooted counterpart delays failure and reduces movement, consistent with reinforced tests. These results establish MPM as a practical tool for assessing both the stability of vegetated slopes and the consequences of their failure.

The dissertation of Sultan Khalid Aldakhil is approved.

Idil Deniz Akin

Scott Joseph Brandenberg

Pedro Arduino

Ertugrul Taciroglu, Committee Chair

University of California, Los Angeles

2026

To my parents, my wife, and my children.

Contents

List of Figures

List of Tables

ACKNOWLEDGMENTS

I am deeply grateful to my advisor and committee chair, Professor Ertugrul Taciroglu, for his patient guidance, encouragement, and support throughout this research. I also thank the members of my doctoral committee, Idil Deniz Akin, Scott Joseph Brandenberg, and Pedro Arduino, for their time and valuable feedback.

Chapter 3 is a version of: Aldakhil, S., and Taciroglu, E. "Stability Analysis of Dry and Unsaturated Soil Slopes Using the Material Point Method," in preparation for publication. Chapter 4 is a version of: Aldakhil, S., and Taciroglu, E. "Vegetation Effects on the Stability of Rainfall-Induced Landslides Using the Material Point Method," in preparation for publication. Simulations and analyses in these chapters were performed by the author, and supervised by Professor Taciroglu. I thank my co-author for his guidance and support in the preparation of these manuscripts.

Above all, I thank my parents, who always believed in me, encouraged me to give my best in everything, and inspired me to pursue the highest levels of education. My father, a professor himself, has been my inspiration. He encouraged me to take this path and supported me every step of the way. My mother's endless love and prayers have carried me farther than she will ever know. I thank my wife for her patience and support throughout the years we spent far away from home. I am grateful for my two children, who bring me the greatest joy in life and remind me every day why this work matters. Without my family's support, none of this would have been possible.

VITA

2017	Bachelor of Science in Civil Engineering, King Fahd University of Petroleum and Minerals.
2017–2018	Graduate Assistant, King Fahd University of Petroleum and Minerals.
2020	Master of Science in Civil Engineering, University of California, Los Angeles.

PUBLICATIONS AND PRESENTATIONS

Aldakhil, S., and Taciroglu, E. "Stability Analysis of Dry and Unsaturated Soil Slopes Using the Material Point Method." In preparation.

Aldakhil, S., and Taciroglu, E. "Vegetation Effects on the Stability of Rainfall-Induced Landslides Using the Material Point Method." In preparation.

Chapter 1

Introduction

1.1 Background and Motivation

Slope failures are among the most destructive natural hazards, causing thousands of deaths and extensive damage to property and infrastructure every year (Froude & Petley, 2018; Haque et al., 2019). Reliable assessment of slope stability, together with prediction of the movement that follows failure, is therefore of major practical importance.

Conventional analyses evaluate stability through a factor of safety. Limit equilibrium methods (LEMs) compute it along an assumed sliding surface, while the finite element method (FEM) reduces shear strength until equilibrium can no longer be satisfied. Both are well established, yet neither describes deformation adequately, since LEMs treat the failing mass as rigid and perfectly plastic and FEM is restricted to small deformations.

Post-failure response is governed by large deformation and rapid movement of the soil mass, and capturing it requires a method formulated for that regime. The Material Point Method (MPM) (Sulsky et al., 1994) discretizes soil into Lagrangian material points that carry all state variables, while equations of motion are solved on an Eulerian background mesh that is reset after each computational step. Material points are not tied to the mesh, so the method avoids the mesh distortion that limits FEM under large deformation. Consequently, MPM has become a principal tool for landslide and runout analysis (Ceccato et al., 2024; Soga et al., 2016), including back-analysis of documented failures such as the 2014 Oso landslide in Washington State (Yerro et al., 2019).

A sustainable defense against rainfall-induced shallow landslides is vegetation. Plant roots reinforce soil mechanically, by mobilizing tensile resistance that raises the apparent cohesion of the rooted zone, and hydrologically, by altering its retention and conductivity (Ni et al., 2018; Stokes et al., 2009). Roots concentrate near the surface, which makes them most effective against exactly the shallow failures that dominate rainfall-induced events. Nevertheless, vegetation has seldom been included in large-deformation analyses of slope failure (Cuomo et al., 2024), and its influence on failure initiation and post-failure behavior remains largely unexplored. This dissertation therefore applies MPM in two parts. The stability of dry and unsaturated slopes is first evaluated through the strength reduction technique, and the effect of vegetation on the initiation and runout of rainfall-induced failures is then investigated.

1.2 Objectives and Scope

The overall objective of this dissertation is to establish the Material Point Method as a unified framework capable of describing both the stability of a slope and its behavior after failure, and to apply this framework to investigate the influence of vegetation. The specific objectives are as follows.

1. To present the formulation of the one-phase and coupled two-phase Material Point Method and to verify its implementation against classical benchmark problems in poromechanics.

2. To evaluate the method for the slope stability analysis of dry and unsaturated slopes through the strength reduction technique, and to compare the computed factors of

safety and slip surfaces with finite element and limit equilibrium solutions.

3. To incorporate the reinforcing effect of vegetation by implementing and validating an advanced constitutive model for root-reinforced soil, and to apply it to the failure and runout of vegetated slopes, including the simulation of a documented centrifuge test.

Vegetation influences slope behavior in many ways that vary in space and time, and isolating each effect individually is not feasible. This study therefore focuses on the mechanical reinforcement provided by roots, represented by treating rooted soil as a homogeneous composite. Effects beyond this scope include the loss of reinforcement caused by root decay, the dependence of root strength on root age, and the extraction of water by evapotranspiration.

1.3 Organization of the Dissertation

The remainder of this dissertation is organized as follows. Chapter 2 presents the Material Point Method, developing the one-phase and coupled two-phase formulations and verifying them against undrained wave-propagation and one-dimensional consolidation benchmarks. Chapter 3 applies the method to the stability of dry and unsaturated slopes and compares the computed factors of safety and failure surfaces with finite element and limit equilibrium solutions. Chapter 4 investigates vegetated slopes by implementing a constitutive model for root-reinforced soil, validating it against triaxial tests, applying it to rainfall-induced failure and runout, and simulating a documented centrifuge experiment. Chapter 5 summarizes the principal findings and outlines directions for future research.

Chapter 2

The Material Point Method

2.1 Introduction

The standard Material Point Method (MPM) is a hybrid Eulerian–Lagrangian numerical technique originally proposed by Sulsky et al. (1994) as an extension of the Fluid-Implicit Particle (FLIP) method (Brackbill et al., 1988) to solid mechanics. FLIP is a variant of the Particle-in-Cell (PIC) method, developed primarily to overcome numerical artifacts found in PIC, and is typically used to simulate fluid flow. In the following, the terms *particle* and *material point* are used interchangeably.

In MPM, the continuum body is discretized into a finite set of particles that move as the body deforms. All history-dependent variables such as mass, density, velocity, stress, and strain are carried by the particles through the simulation. These variables are updated at every time step by considering the current configuration as the new reference frame, making it an updated Lagrangian formulation. In contrast, a total Lagrangian approach, such as the traditional FEM, always uses the initial undeformed configuration to update the variables. This implies that MPM can effectively simulate large deformations and extreme loading conditions without suffering from mesh distortion, which is typical in FEM under such conditions.

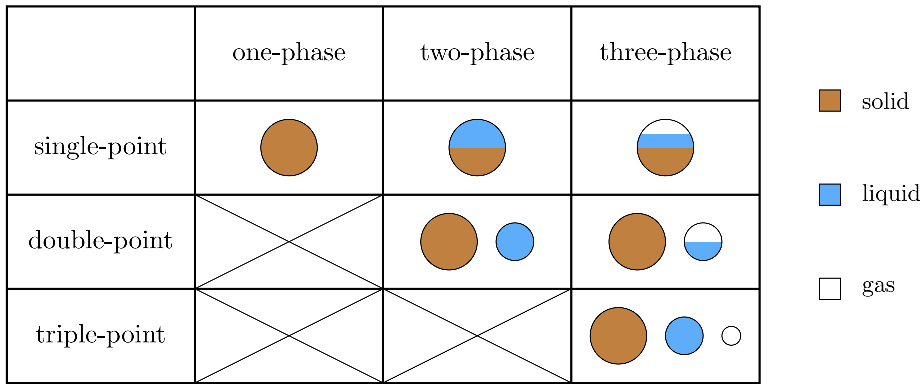

Figure 2.1: Multi-phase approaches in MPM: complexity and computational cost increase from left to right and top to bottom.

The Eulerian description is characterized by the presence of a computational mesh (also called background grid, cells, or elements) similar to the one used in FEM. It should, however, cover the entire space where particles are expected to move during the simulation. The elements used are typically quadrilateral or triangular in 2D, and hexahedral or tetrahedral in 3D.

Soil is a complex multi-phase material composed of a solid skeleton with pores filled by fluids such as water and air. When the scale of the physical interactions between individual grains is much smaller than the scale of the problem, continuum laws can be applied to describe the material response. In many geotechnical problems soil behavior is strongly influenced by the presence of pore fluids, and thus it is necessary to account for the interaction between different phases. Figure 2.1 shows various multi-phase approaches in MPM; our discussion, however, will be limited to the *one-phase* and *two-phase* single-point formulations.

In this chapter, we present the theoretical foundations of the Material Point Method. The one-phase formulation for dry soils and pure fluids is developed first, followed by its extension to the coupled two-phase formulation for saturated soils. The implementation is then verified against two classical benchmark problems in poromechanics, namely undrained wave propagation and one-dimensional consolidation.

2.2 One-Phase Formulation

The formulation of standard MPM (Sulsky et al., 1995) was originally developed for solid materials, but can be generally applied to fluids as well. Later we will discuss two-phase systems and the interaction between solid and pore water in saturated soils. The governing equations presented in this section follow the formulation presented in Al-Kafaji (2013) but omit many details and intermediate steps for brevity. Two fundamental balance laws are of interest, namely *balance of mass* and *balance of linear momentum*. The reader is referred to standard continuum mechanics textbooks, e.g. Anand and Govindjee (2020) and Bonet and Wood (2008), for a comprehensive treatment of balance laws.

2.2.1 Governing Equations

Balance of Mass

In a closed system with no mass exchange with the external environment, the rate of change of total mass with respect to time is zero. Mathematically, this can be expressed as

$$\frac{Dm}{Dt} = \frac{D}{Dt}\int_{\Omega} \rho \, \mathrm{d}V = 0 \tag{2.1}$$

where ρ is the density of the material, Ω is a region in the deformed body at any time instant, and $\mathrm{d}V$ is a differential volume element. The operator $D(\bullet)/Dt = \partial(\bullet)/\partial t + \mathrm{grad}(\bullet) \cdot \mathbf{v}$ is called the material derivative with respect to time. Applying Reynolds transport theorem gives

$$\frac{D}{Dt}\int_{\Omega} \rho \, \mathrm{d}V = \int_{\Omega} \left[\frac{D\rho}{Dt} + \rho \, \mathrm{div}(\mathbf{v})\right] \mathrm{d}V = 0 \tag{2.2}$$

Since Ω is arbitrary, the integrand must be zero for all points in the domain. This leads to a local form of mass balance law,

$$\frac{D\rho}{Dt} + \rho \, \mathrm{div}(\mathbf{v}) = 0 \tag{2.3}$$

where $\mathbf{v}$ is the velocity field vector. This equation is also known as the continuity equation in fluid mechanics applications.

Balance of Linear Momentum

The dynamic formulation of linear momentum (i.e., non-zero inertial term) states that the change in linear momentum of a continuum body, Ω, is equal to the sum of internal and external forces acting on it, i.e.,

$$\frac{D}{Dt}\int_{\Omega} \rho\mathbf{v}\,\mathrm{d}V = \int_{\partial\Omega} \boldsymbol{\sigma}\cdot\mathbf{n}\,\mathrm{d}S + \int_{\Omega} \rho\mathbf{b}\,\mathrm{d}V \tag{2.4}$$

where $\boldsymbol{\sigma}$ is the Cauchy stress tensor, $\mathbf{n}$ is the outward normal vector to the boundary $\partial\Omega$, and $\mathbf{b}$ is the body force per unit mass. In the sequel, only the gravitational acceleration is considered as the external driving force ($\mathbf{b} = \mathbf{g}$). The global form of linear momentum balance is given by Equation (2.4). It may also be reduced to a local form by applying Reynolds transport theorem. With some algebraic manipulation, the final form becomes

$$\rho\mathbf{a} = \mathrm{div}(\boldsymbol{\sigma}) + \rho\mathbf{g} \tag{2.5}$$

where $\mathbf{a} = D\mathbf{v}/Dt$ is the acceleration vector, which is typically the primary unknown to be determined at the grid nodes of non-empty elements.

Conservation of angular momentum is automatically satisfied in MPM due to the symmetry of Cauchy's stress tensor, $\boldsymbol{\sigma} = \boldsymbol{\sigma}^T$. Thus, no additional equation is required to enforce this condition.

In parts of the literature, the balance of linear momentum, equation (2.5), is referred to as the balance of forces, while the balance of moments refers to angular momentum. In this thesis, the term momentum refers to linear momentum only.

Boundary Conditions

For a continuum problem to satisfy the governing equations and be well-posed, specified boundary conditions must be applied at every point on the boundary $\partial\Omega$. An essential boundary condition is imposed on points where displacements are prescribed, i.e.,

$$\mathbf{u}(\mathbf{x},t) = \hat{\mathbf{u}}(t) \qquad \text{on} \qquad \partial\Omega^u \tag{2.6}$$

whereas a natural boundary condition is defined on parts where surface tractions are applied. Expressing the applied traction in terms of Cauchy's stress tensor and surface normal gives

$$\boldsymbol{\sigma}(\mathbf{x},t)\,\mathbf{n} = \hat{\boldsymbol{\tau}}(t) \qquad \text{on} \qquad \partial\Omega^\tau \tag{2.7}$$

Typically, a combination of different boundary conditions is necessary for most problems, in which case the condition $\partial\Omega^u \cap \partial\Omega^\tau = \emptyset$ must be satisfied. In other words, only one type of boundary condition may be prescribed at any given boundary point and instant in time.

Because the equations of motion are solved at the grid nodes, boundary conditions in MPM are imposed directly on the nodes, in the same way as in FEM. This gives MPM an advantage over purely mesh-free methods, where the absence of a background mesh means that boundary conditions must be enforced on the particles.

In many large-deformation problems, boundary conditions should be applied to material points instead of grid nodes. Consider, for example, a cantilever beam fixed at one end and subjected to a point load at the other. The fixed end does not move, so a zero-velocity condition can be imposed directly on the nodes. Under large deflections, however, the point load should be carried by material points, which move with the material and therefore keep the force attached to the tip and normal to the beam as it deforms.

Initial Conditions

The initial values of displacement, velocity, and stress are specified before the start of the simulation. These values are given by

$$\mathbf{u}(\mathbf{x}, t=0) = \mathbf{u}_0, \qquad \mathbf{v}(\mathbf{x}, t=0) = \mathbf{v}_0, \qquad \boldsymbol{\sigma}(\mathbf{x}, t=0) = \boldsymbol{\sigma}_0 \tag{2.8}$$

where $\mathbf{u}_0$, $\mathbf{v}_0$, and $\boldsymbol{\sigma}_0$ are the initial values of displacement, velocity, and stress, respectively. Further discussion on the initialization procedure of other quantities, such as mass, volume, and traction force, is provided in Section 2.2.3.

From Strong to Weak Form

To discretize the momentum balance equation, the strong form given in Equation (2.5) must first be transformed into a weak form. This is achieved by multiplying it by a weighting function, $\delta\mathbf{v}$, and integrating over the entire domain, i.e.,

$$\int_\Omega \delta\mathbf{v} \cdot \rho\mathbf{a}\,\mathrm{d}V = \int_\Omega \delta\mathbf{v} \cdot \mathrm{div}(\boldsymbol{\sigma})\,\mathrm{d}V + \int_\Omega \delta\mathbf{v} \cdot \rho\mathbf{g}\,\mathrm{d}V \tag{2.9}$$

The first term on the right-hand side can be expanded using integration by parts and applying the divergence theorem,

$$\begin{aligned}\int_\Omega \delta\mathbf{v} \cdot \mathrm{div}(\boldsymbol{\sigma})\,\mathrm{d}V &= \int_\Omega \mathrm{div}(\boldsymbol{\sigma} \cdot \delta\mathbf{v})\,\mathrm{d}V - \int_\Omega \mathrm{grad}(\delta\mathbf{v})\colon \boldsymbol{\sigma}\,\mathrm{d}V \\ &= \int_{\partial\Omega^\tau} \delta\mathbf{v} \cdot \hat{\boldsymbol{\tau}}\,\mathrm{d}S - \int_\Omega \mathrm{grad}(\delta\mathbf{v})\colon \boldsymbol{\sigma}\,\mathrm{d}V\end{aligned} \tag{2.10}$$

in which ":" implies a double contraction between two second-order tensors. Hence, upon substitution into Equation (2.9) we arrive at the weak form of the momentum balance equation

$$\int_\Omega \delta\mathbf{v} \cdot \rho\mathbf{a}\,\mathrm{d}V = \int_{\partial\Omega^\tau} \delta\mathbf{v} \cdot \hat{\boldsymbol{\tau}}\,\mathrm{d}S + \int_\Omega \delta\mathbf{v} \cdot \rho\mathbf{g}\,\mathrm{d}V - \int_\Omega \mathrm{grad}(\delta\mathbf{v})\colon \boldsymbol{\sigma}\,\mathrm{d}V \tag{2.11}$$

which will be discretized in the next section to obtain the semi-discretized form.

2.2.2 Spatial and Temporal Discretization

Spatial Discretization

Similar to the FEM discretization process, the computational mesh consists of nodes and triangular elements in the 2D case, or tetrahedral elements in the 3D case. Closed-form solutions to Equation (2.11) are difficult, if not impossible, to obtain. Instead, the general solution is approximated using standard nodal shape functions. A Bubnov–Galerkin approach (Zienkiewicz et al., 2025) is used to construct the semi-discretized momentum equation.

To illustrate the process let us approximate the field quantities (displacement, velocity, and acceleration) and their virtual counterparts as follows:

$$\mathbf{u}(\mathbf{x},t) \approx \mathbf{N}(\mathbf{x})\hat{\mathbf{u}}(t), \qquad \delta\mathbf{u}(\mathbf{x},t) \approx \mathbf{N}(\mathbf{x})\delta\hat{\mathbf{u}}(t) \tag{2.12a}$$

$$\mathbf{v}(\mathbf{x},t) \approx \mathbf{N}(\mathbf{x})\hat{\mathbf{v}}(t), \qquad \delta\mathbf{v}(\mathbf{x},t) \approx \mathbf{N}(\mathbf{x})\delta\hat{\mathbf{v}}(t) \tag{2.12b}$$

$$\mathbf{a}(\mathbf{x},t) \approx \mathbf{N}(\mathbf{x})\hat{\mathbf{a}}(t), \qquad \delta\mathbf{a}(\mathbf{x},t) \approx \mathbf{N}(\mathbf{x})\delta\hat{\mathbf{a}}(t) \tag{2.12c}$$

where the hat superscript denotes nodal vector quantities. For each computational step a node is considered active if it interacts with at least one particle, and only these active nodes are included in the calculations to reduce cost. Assuming the total number of active nodes in the entire mesh is denoted by I, then

$$\hat{\mathbf{u}} = \begin{bmatrix} \hat{u}_{11} & \hat{u}_{12} & \hat{u}_{13} & \dots & \hat{u}_{I1} & \hat{u}_{I2} & \hat{u}_{I3} \end{bmatrix}^{\mathrm{T}} \tag{2.13a}$$

$$\hat{\mathbf{v}} = \begin{bmatrix} \hat{v}_{11} & \hat{v}_{12} & \hat{v}_{13} & \dots & \hat{v}_{I1} & \hat{v}_{I2} & \hat{v}_{I3} \end{bmatrix}^{\mathrm{T}} \tag{2.13b}$$

$$\hat{\mathbf{a}} = \begin{bmatrix} \hat{a}_{11} & \hat{a}_{12} & \hat{a}_{13} & \dots & \hat{a}_{I1} & \hat{a}_{I2} & \hat{a}_{I3} \end{bmatrix}^{\mathrm{T}} \tag{2.13c}$$

where the first subscript of each component denotes the nodal number, while the second denotes the direction with respect to the coordinate system (i.e., x_1, x_2, and x_3). For example, $\hat{v}_{13}$ indicates the velocity of node 1 in the x_3 coordinate direction. The virtual quantities $\delta\hat{\mathbf{u}}$,

$\delta\hat{\mathbf{v}}$, and $\delta\hat{\mathbf{a}}$ are defined in a similar manner.

The nodal shape function matrix $\mathbf{N}(\mathbf{x})$ is assembled from the individual nodal contributions as

$$\mathbf{N}(\mathbf{x}) = \begin{bmatrix}\mathbf{N}_1(\mathbf{x}) & \mathbf{N}_2(\mathbf{x}) & \dots & \mathbf{N}_I(\mathbf{x})\end{bmatrix} \tag{2.14}$$

where each entry is a diagonal matrix given by

$$\mathbf{N}_i(\mathbf{x}) = \begin{bmatrix} N_i(\mathbf{x}) & 0 & 0 \\ 0 & N_i(\mathbf{x}) & 0 \\ 0 & 0 & N_i(\mathbf{x}) \end{bmatrix} \tag{2.15}$$

For simplicity, standard linear shape functions are used in this work. Since linear shape functions are only C^0 continuous, at least one integration point is required to evaluate the integrals over tetrahedral elements numerically.

A common practice for representing strain measures is to recast them in a form convenient for implementation. For instance, the strain-rate tensor can be arranged in vector form, known as Voigt notation, as shown in equation (2.16). To maintain consistency with other MPM presentations, the order of shear components here is slightly different from Voigt's original. Due to the symmetry of the strain tensor, three-dimensional problems consist of six independent strain components: three normal and three shear. The strain rate can be expressed as the product of a linear differential operator and the velocity vector (i.e., $\dot{\boldsymbol{\epsilon}}(\mathbf{x}, t) = \mathbf{L}\mathbf{v}(\mathbf{x}, t)$). This quantity is commonly referred to as the rate of deformation, and it is given by

$$\begin{Bmatrix} \dot{\epsilon}_{11} \\ \dot{\epsilon}_{22} \\ \dot{\epsilon}_{33} \\ 2\dot{\epsilon}_{12} \\ 2\dot{\epsilon}_{23} \\ 2\dot{\epsilon}_{31} \end{Bmatrix} = \begin{bmatrix} \dfrac{\partial}{\partial x_1} & 0 & 0 \\ 0 & \dfrac{\partial}{\partial x_2} & 0 \\ 0 & 0 & \dfrac{\partial}{\partial x_3} \\ \dfrac{\partial}{\partial x_2} & \dfrac{\partial}{\partial x_1} & 0 \\ 0 & \dfrac{\partial}{\partial x_3} & \dfrac{\partial}{\partial x_2} \\ \dfrac{\partial}{\partial x_3} & 0 & \dfrac{\partial}{\partial x_1} \end{bmatrix} \begin{Bmatrix} v_1 \\ v_2 \\ v_3 \end{Bmatrix} \tag{2.16}$$

which may be rewritten using the approximated velocity field equation (2.12b) as

$$\dot{\boldsymbol{\epsilon}}(\mathbf{x}, t) = \mathbf{B}(\mathbf{x})\hat{\mathbf{v}}(t) \tag{2.17}$$

where

$$\mathbf{B}(\mathbf{x}) = \begin{bmatrix}\mathbf{B}_1(\mathbf{x}) & \mathbf{B}_2(\mathbf{x}) & \dots & \mathbf{B}_I(\mathbf{x})\end{bmatrix} \tag{2.18}$$

is known as the *strain-displacement matrix*, and

$$\mathbf{B}_i(\mathbf{x}) = \begin{bmatrix} \dfrac{\partial N_i(\mathbf{x})}{\partial x_1} & 0 & 0 \\ 0 & \dfrac{\partial N_i(\mathbf{x})}{\partial x_2} & 0 \\ 0 & 0 & \dfrac{\partial N_i(\mathbf{x})}{\partial x_3} \\ \dfrac{\partial N_i(\mathbf{x})}{\partial x_2} & \dfrac{\partial N_i(\mathbf{x})}{\partial x_1} & 0 \\ 0 & \dfrac{\partial N_i(\mathbf{x})}{\partial x_3} & \dfrac{\partial N_i(\mathbf{x})}{\partial x_2} \\ \dfrac{\partial N_i(\mathbf{x})}{\partial x_3} & 0 & \dfrac{\partial N_i(\mathbf{x})}{\partial x_1} \end{bmatrix} \tag{2.19}$$

So far the similarity between MPM and FEM in deriving the governing equations is obvious; the main difference, however, lies in how the continuum domain is discretized. In MPM, the continuum is discretized into a set of particles that move attached to the material (Figure 2.2), while in standard FEM, the continuum is discretized into a mesh of elements

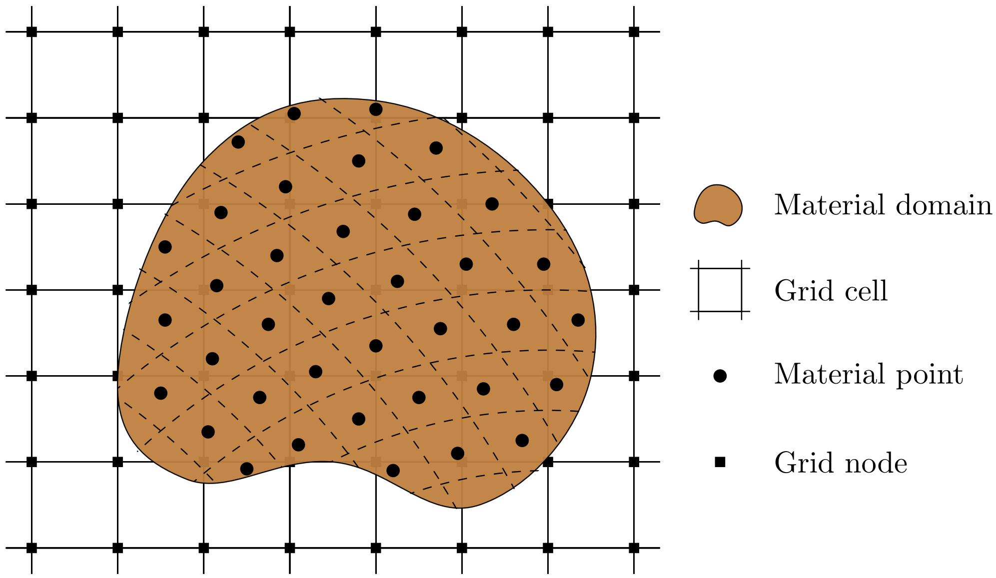

Figure 2.2: A typical discretization of a continuous body using material points and a background mesh for solving the governing equations.

with nodes. Conceptually, MPM particles can be viewed as free-moving Gauss points that traverse through fixed elements.

Let us assume that the total mass of the domain is the sum of each particle's mass. Mathematically, this is equivalent to

$$\rho(\mathbf{x}, t) = \sum_{p=1}^{n_p} m_p \delta(\mathbf{x} - \mathbf{x}_p) \tag{2.20}$$

where δ is the Dirac delta function, $\mathbf{x}_p$ and m_p are the position and mass of a particle p, respectively. n_p represents the total number of particles. Substituting equations (2.12b), (2.18) and (2.20) into equation (2.11) and observing that $\delta\hat{\mathbf{v}}$ is an arbitrary virtual velocity field (except where a boundary velocity is prescribed), we arrive at the discretized form of the momentum balance equation

$$\sum_{p=1}^{n_p} m_p \mathbf{N}_p^{\mathrm{T}} \cdot \mathbf{N}_p \hat{\mathbf{a}} = \int_{\partial\Omega^\tau} \mathbf{N}_p^{\mathrm{T}} \cdot \hat{\boldsymbol{\tau}} \, \mathrm{d}S - \sum_{p=1}^{n_p} \mathbf{B}_p^{\mathrm{T}} \cdot \boldsymbol{\sigma}_p V_p + \sum_{p=1}^{n_p} m_p \mathbf{N}_p^{\mathrm{T}} \cdot \mathbf{g} \tag{2.21}$$

which is exactly Newton's second law of motion with

$$\mathbf{M} = \sum_{p=1}^{n_p} m_p \mathbf{N}_p^{\mathrm{T}} \cdot \mathbf{N}_p \tag{2.22a}$$

$$\mathbf{F}^{ext} = \sum_{p=1}^{n_p} m_p \mathbf{N}_p^{\mathrm{T}} \cdot \mathbf{g} + \int_{\partial\Omega^{\tau}} \mathbf{N}_p^{\mathrm{T}} \cdot \hat{\boldsymbol{\tau}} \, \mathrm{d}S \tag{2.22b}$$

$$\mathbf{F}^{int} = \sum_{p=1}^{n_p} \mathbf{B}_p^{\mathrm{T}} \cdot \boldsymbol{\sigma}_p V_p \tag{2.22c}$$

where $\mathbf{F}^{int}$ denotes the global internal force vector, $\mathbf{F}^{ext}$ is the global external force vector, and $\mathbf{M}$ is the consistent mass matrix. These terms are evaluated at the grid nodes of the computational mesh to determine the unknown nodal acceleration vector.

The semi-discrete form equation (2.21) can alternatively be derived from FEM by treating the material points as integration points, with their associated volumes serving as the integration weights. Either approach will result in quadrature errors that are significantly higher than those in FEM where integrals are typically evaluated at Gauss points. An additional source of quadrature error in MPM is the so-called cell-crossing instability (Steffen et al., 2008) which is unfortunately inherent in the method and cannot be eliminated entirely.

Temporal Discretization

The momentum balance equation was discretized in space in the previous section, but is still continuous in time. A semi-implicit Euler–Cromer or symplectic Euler scheme is adopted in this thesis. Although fully implicit schemes are unconditionally stable, they are typically suited for quasi-static problems, and when applied to simulate a landslide, important deformation features may be lost due to large time increments.

Suppose the solution at the current time t^n is known; our goal is to determine the solution at the next time step $t^{n+1} = t^n + \Delta t$, where Δt is the time step. The semi-discretized momentum equation equation (2.21), evaluated at the current time, can be written as

$$\mathbf{M}^n \mathbf{a}^n = \mathbf{F}^{ext,n} - \mathbf{F}^{int,n} \tag{2.23}$$

where the nodal acceleration vector $\mathbf{a}^n$ is the primary unknown. To simplify notation, the hat symbol previously used to denote a nodal quantity is dropped. The nodal velocities at the next time step are calculated using an explicit Euler scheme, meaning they are computed directly from known values at the current time step t^n, i.e.,

$$\mathbf{v}^{n+1} = \mathbf{v}^n + \Delta t\, \mathbf{a}^n \tag{2.24}$$

which can then be used to update nodal displacements as

$$\mathbf{u}^{n+1} = \mathbf{u}^n + \Delta t\, \mathbf{v}^{n+1} \tag{2.25}$$

In MPM, however, the computational mesh is reset at the end of each time step, so calculating the nodal displacement is a redundant step. Nodal velocities are used next to update the particle state. The particle state variables are updated by interpolating the nodal values using shape functions, which in our case are linear. For example, in the original algorithm proposed by Sulsky et al. (1994), particle positions and velocities are computed according to the following transfer scheme

$$\mathbf{v}_p^{n+1} = \mathbf{v}_p^n + \Delta t \sum_{i=1}^{n_{en}} N_i(\mathbf{x}_p^n)\mathbf{a}_i^n \tag{2.26a}$$

$$\mathbf{x}_p^{n+1} = \mathbf{x}_p^n + \Delta t \sum_{i=1}^{n_{en}} N_i(\mathbf{x}_p^n)\mathbf{v}_i^{n+1} \tag{2.26b}$$

where n_{en} denotes the number of element nodes. This scheme, known as the Update Stress Last (USL), suffers from the so-called small mass issue. Consider a one-dimensional two-node element with shape functions N_1 and N_2, and let a single particle p have just entered this initially empty element from the side of node 1, so that $N_1(\xi_p) \approx 1$ and $N_2(\xi_p) \approx 0$. The mapped nodal masses are $m_1 = m_p N_1(\xi_p)$ and $m_2 = m_p N_2(\xi_p)$, which means m_2

is vanishingly small. The internal force f_2 remains finite nonetheless, because it involves the shape function gradient, which is constant over the element. As a result, the nodal acceleration $a_2 = f_2/m_2$ becomes enormous and may cause the particle to detach from the material. Sulsky et al. (1995) overcame this issue with the Modified Update Stress Last (MUSL) algorithm, which recovers the nodal velocities from the updated particle momentum instead of integrating the nodal accelerations. This algorithm is adopted in this thesis, and its steps are detailed in section 2.2.3.

Numerous solution schemes have been proposed since the original MPM was developed in an effort to improve stability, e.g., the Update Stress First (Bardenhagen, 2002) and the Update Stress Average (Nairn, 2003). A detailed discussion of these methods is beyond the scope of this thesis, and the reader is referred to the aforementioned references for additional information.

2.2.3 Solution Procedure

Particle Data Initialization

In numerical implementations it is usually convenient to evaluate equations (2.22a) to (2.22c) for each element and then assemble the results into a global system of equations. This thesis adopts tetrahedral elements for three-dimensional problems and triangular elements for two-dimensional problems.

To illustrate the initialization procedure of relevant quantities such as mass, volume and traction let us define the global position of a particle p as a function of local coordinates $\boldsymbol{\xi}$, or sometimes called parent coordinates, such that

$$\mathbf{x}_p(\boldsymbol{\xi}_p) = \sum_{i=1}^{n_{en}} N_i(\boldsymbol{\xi}_p)\mathbf{x}_i \tag{2.27}$$

where $\mathbf{x}_i$ is the global coordinates of node i, and $N_i(\boldsymbol{\xi}_p)$ is the shape function evaluated at the position of a particle p in local coordinates. The total volume of an element is distributed uniformly among the particles inside that element, and so the volume of each particle is

$$V_p = \frac{1}{n_{ep}} \int_{\Omega_{el}} \mathrm{d}\Omega \approx \frac{1}{n_{ep}} \sum_{g=1}^{n_{eg}} |\mathbf{J}(\boldsymbol{\xi}_g)| w_g \tag{2.28}$$

where n_{ep} denotes the number of particles in an element, n_{eg} is the number of Gauss points, $\boldsymbol{\xi}_g$ is the local coordinates of a Gauss integration point, w_g is the weight of the Gauss integration point, and $|\mathbf{J}(\boldsymbol{\xi}_g)|$ is the determinant of the Jacobian matrix evaluated at that point. For a given material density ρ_p associated with a particle p, the mass of that particle can be simply computed as

$$m_p = \rho_p V_p \tag{2.29}$$

It should be noted here that mass is a conserved quantity, whereas volume and density may change during the simulation.

The external force vector associated with a particle p consists of two parts, the gravitational force and the prescribed traction force. The gravitational force is easily obtained by multiplying the mass of that particle by the gravitational acceleration vector $\mathbf{g}$, i.e.,

$$\mathbf{f}_p^{\mathrm{grav}} = m_p \mathbf{g} \tag{2.30}$$

The traction force term is more complex to handle. This is because, in MPM, tractions can be applied either on (i) the boundary elements or (ii) the material points. Option (i) is only applicable when the continuum boundary subject to traction is aligned with the boundary of an element throughout the computation. In this case the traction force is handled the same way as in classical FEM. Option (ii) is applicable when the continuum natural boundary is moving through the mesh. To illustrate how traction forces are assigned to particles let us consider a tetrahedral element with a traction $\hat{\boldsymbol{\tau}}_e$ applied to one of its triangular faces, as shown in Figure 2.3. The traction of a boundary particle p is computed by interpolating the nodal values as

$$\hat{\boldsymbol{\tau}}_e(\mathbf{x}_p) \approx \sum_{i=1}^{n_{tri}} N_i(\boldsymbol{\xi}_p) \hat{\boldsymbol{\tau}}_e(\mathbf{x}_i) \tag{2.31}$$

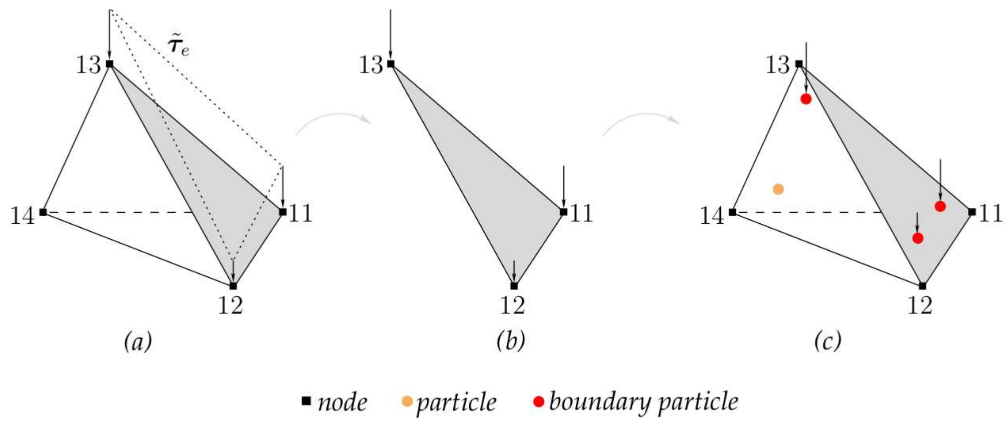

Figure 2.3: Surface traction initialization: (a) external traction applied on a tetrahedral element; (b) triangular boundary element; (c) mapping of nodal traction to boundary material points. (from Al-Kafaji, 2013)

where n_{tri} denotes the number of nodes of the boundary triangular element and $\boldsymbol{\xi}_p$ is the local coordinates of a boundary particle p, which also represents the projection of the particle's position onto the triangular face. Finally, the traction force vector carried by each boundary particle becomes

$$\begin{aligned} \mathbf{f}_p^{\text{trac}} &= \frac{S_{el}}{n_{ebp}} \hat{\boldsymbol{\tau}}_e(\mathbf{x}_p) \\ &= \frac{S_{el}}{n_{ebp}} \sum_{i=1}^{n_{tri}} N_i(\boldsymbol{\xi}_p) \hat{\boldsymbol{\tau}}_e(\mathbf{x}_i) \end{aligned} \tag{2.32}$$

where S_{el} is the area of the triangular element, and n_{ebp} is the number of boundary particles in that element.

Equations of Motion Initialization

In order to solve for the acceleration in equation (2.23) at a given time t^n, it is necessary to invert the consistent mass matrix first. This step can be computationally expensive for large-scale problems and is usually avoided. Instead, a row sum lumping approach is implemented to convert the consistent mass into a diagonal matrix. Such a procedure makes matrix inversion trivial at the cost of introducing additional dissipation of kinetic energy (Burgess et al., 1992).

Let us consider an element containing n_{en} nodes and n_{ep} particles. The corresponding lumped mass matrix is then given by

$$\mathbf{M}_e^{\text{lump}} \approx \begin{bmatrix} \mathbf{m}_1 & \mathbf{0} & \dots & \mathbf{0} \\ \mathbf{0} & \mathbf{m}_2 & \dots & \mathbf{0} \\ \vdots & \vdots & \ddots & \vdots \\ \mathbf{0} & \mathbf{0} & \dots & \mathbf{m}_{n_{en}} \end{bmatrix} \tag{2.33}$$

with

$$\mathbf{m}_i = \begin{bmatrix} m_i & 0 & 0 \\ 0 & m_i & 0 \\ 0 & 0 & m_i \end{bmatrix} \qquad \text{and} \qquad \mathbf{0} = \begin{bmatrix} 0 & 0 & 0 \\ 0 & 0 & 0 \\ 0 & 0 & 0 \end{bmatrix} \tag{2.34}$$

Here the mass of each node m_i is computed by summing the contribution of all particles in that element,

$$m_i \approx \sum_{p=1}^{n_{ep}} m_p N_i(\boldsymbol{\xi}_p) \tag{2.35}$$

The element matrices are then assembled into a global mass matrix. Thus we have

$$\mathbf{M} = \sum_{e=1}^{\bar{n}_{elm}} \mathbf{M}_e^{\text{lump}} \tag{2.36}$$

where $\bar{n}_{elm}$ denotes the number of active elements, which may change from one time step to another as particles travel through the mesh. Consequently, a new mass matrix needs to be constructed at the beginning of each time step.

The nodal external force vector is obtained by mapping the particle forces to grid nodes, which can be written as

$$\mathbf{F}^{ext} = \sum_{e=1}^{\bar{n}_{elm}} \sum_{p=1}^{n_{ep}} \mathbf{N}^{\text{T}}(\boldsymbol{\xi}_p) \cdot \mathbf{f}_p^{\text{grav}} + \sum_{e=1}^{\bar{n}_{belm}} \sum_{p=1}^{n_{ebp}} \mathbf{N}^{\text{T}}(\boldsymbol{\xi}_p) \cdot \mathbf{f}_p^{\text{trac}} \tag{2.37}$$

where $\bar{n}_{elm}$ and $\bar{n}_{belm}$ denote the number of active elements and traction boundary elements, respectively. n_{ep} is the number of element particles and n_{ebp} is the number of traction-carrying particles in an element. The internal force vector is computed as

$$\mathbf{F}^{int} = \sum_{e=1}^{\bar{n}_{elm}} \sum_{p=1}^{n_{ep}} \mathbf{B}^{\text{T}}(\boldsymbol{\xi}_p) \cdot \boldsymbol{\sigma}_p V_p \tag{2.38}$$

Computational Cycle of MPM

A typical solution procedure of a single computational time step is schematically shown in Figure 2.4. First, the information carried by particles is projected onto the grid nodes. The equations of motion are then solved on the grid to obtain nodal accelerations and velocities. Next, the updated nodal velocities are mapped back to the particles to update their positions and velocities. Finally, the computational mesh is reset to its initial configuration. As mentioned earlier, different algorithms exist in the literature, all of which aim to improve the stability of MPM. In this thesis, we adopt the Modified Update Stress Last (MUSL) scheme (Sulsky et al., 1995). The steps required to advance the solution from t^n to t^{n+1} are summarized as follows:

1. Initialize the computational mesh and material point data such as m_p, ρ_p, $\mathbf{x}_p$, $\mathbf{v}_p$, and $\boldsymbol{\sigma}_p$.

2. Compute nodal mass $\mathbf{m}_i^n$ and construct the lumped mass matrix $\mathbf{M}^n$ according to equations (2.33) to (2.36). Note the superscript "lump" is omitted for brevity.

3. Compute the external force vector $\mathbf{F}^{ext,n}$ and internal force vector $\mathbf{F}^{int,n}$ according to equations (2.37) and (2.38), respectively.

4. Solve the momentum equation equation (2.23) and obtain the current nodal accelerations.

$$\mathbf{a}^n = [\mathbf{M}^n]^{-1} (\mathbf{F}^{ext,n} - \mathbf{F}^{int,n}) \tag{2.39}$$

5. Particle velocities are updated as given by equation (2.26a), or

$$\mathbf{v}_p^{n+1} = \mathbf{v}_p^n + \Delta t \sum_{i=1}^{n_{en}} N_i(\boldsymbol{\xi}_p^n)\, \mathbf{a}_i^n \tag{2.40}$$

6. Compute the nodal momentum from equation (2.41), and then use it to solve for the

nodal velocities $\mathbf{v}^{n+1}$.

$$\mathbf{M}^n\,\mathbf{v}^{n+1} = \sum_{e=1}^{\bar{n}_{elm}} \sum_{p=1}^{n_{ep}} m_p \mathbf{N}^{\mathrm{T}}(\boldsymbol{\xi}_p^n)\,\mathbf{v}_p^{n+1} \tag{2.41}$$

7. Particle positions are updated as given by equation (2.26b), or

$$\mathbf{x}_p^{n+1} = \mathbf{x}_p^n + \Delta t \sum_{i=1}^{n_{en}} N_i(\boldsymbol{\xi}_p^n)\,\mathbf{v}_i^{n+1} \tag{2.42}$$

8. Compute the strain increment at particles as a function of nodal velocity.

$$\Delta\boldsymbol{\epsilon}_p^{n+1} = \Delta t \sum_{i=1}^{n_{en}} \mathbf{B}_i(\boldsymbol{\xi}_p^n)\,\mathbf{v}_i^{n+1} \tag{2.43}$$

9. Update the stresses via the material constitutive model.

$$\boldsymbol{\sigma}_p^{n+1} = \boldsymbol{\sigma}_p^n + \Delta\boldsymbol{\sigma}_p(\Delta\boldsymbol{\epsilon}_p^{n+1}) \tag{2.44}$$

10. Volumes and densities of particles are updated using the volumetric strain increment $\Delta\epsilon_{vol,p} = \mathrm{tr}(\Delta\boldsymbol{\epsilon}_p)$. Additional material properties may be updated as well.

$$\begin{aligned} V_p^{n+1} &= (1 + \Delta\epsilon_{vol,p}^{n+1})V_p^n \\ \rho_p^{n+1} &= \frac{\rho_p^n}{1 + \Delta\epsilon_{vol,p}^{n+1}} \end{aligned} \tag{2.45}$$

11. Identify active elements and record the number of particles per element. Other quantities such as the updated local positions of particles are also recorded for book-keeping.

12. Discard the old mesh and initialize a new one for the next computational cycle.

2.3 Two-Phase Formulation

In the previous section we presented the governing equations of the one-phase MPM, which apply to dry soils and pure fluids. In this section we shall discuss the *two-phase single-point*

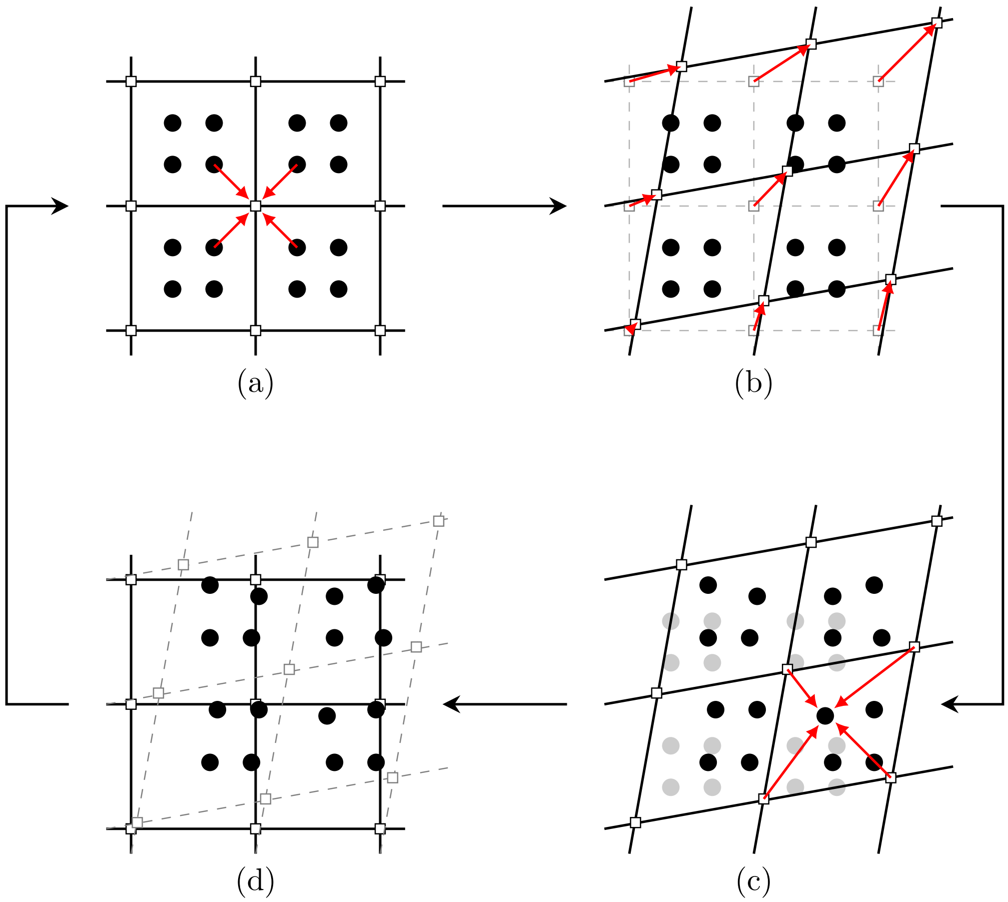

Figure 2.4: MPM computation steps: (a) particle data is projected to the grid; (b) linear momentum equation is solved on the grid; (c) position and velocity of particles are updated; (d) computational grid is reset.

approach for simulating dynamic problems in geomechanics.

Before presenting the governing equation, it should be noted that on certain occasions the behavior of saturated soil can be simplified and analyzed using the one-phase approach. One such case is when a highly permeable soil is subjected to quasi-static loading, in which case water pressures may be obtained using simple uncoupled calculations. On the other hand, if a soil of low permeability is subjected to an undrained loading condition, then a significant increase in excess pore water pressure is observed. Indeed, if the soil's permeability is very low then the relative movement between solid particles and pore liquid is prevented. Any other drainage condition between fully drained and undrained requires a coupled hydro-

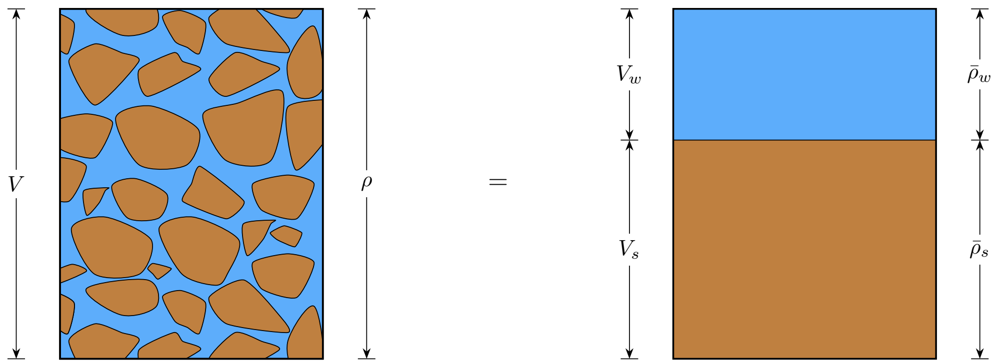

Figure 2.5: Phase diagram of a saturated porous medium.

mechanical analysis, as the developed pressures become a function of the loading history and can no longer be neglected.

2.3.1 Saturated Soil Problems in MPM

In soil mechanics, a porous medium is said to be saturated when the pore spaces between solid particles are completely filled with a fluid, typically water. Let us consider the volumetric phase diagram of a saturated soil sample shown in Figure 2.5. From the definition of porosity n (the volume of voids over the total volume), it is possible to express the total volume as

$$V = V_s + V_w, \qquad V_s = (1 - n)\, V, \qquad V_w = n\, V \tag{2.46}$$

where V_s and V_w are the fractional volumes of solid and liquid, respectively. Similarly, the total mixture density is defined as the sum of the average densities of its constituents. Thus for a fully saturated soil it becomes

$$\rho = \bar{\rho}_s + \bar{\rho}_w = (1 - n)\rho_s + n\rho_w \tag{2.47}$$

where ρ_s and ρ_w are the intrinsic densities of the solid and liquid phases, respectively. The overbar in equation (2.47) denotes an averaged phase density.

Different theories regarding the behavior of multiphase materials have been proposed since the pioneering work of Biot (1956a, 1956b), who formulated the macroscopic dynamic equations for saturated porous media. Most of these theoretical frameworks, despite their sophistication, assume a linear elastic behavior for the solid phase. For this reason, De Boer and Kowalski (1983) highlighted the need to develop a plasticity theory for porous saturated materials. Indeed, Biot's theory was extended to include nonlinearities in the behavior of the solid skeleton as described in Zienkiewicz (1982), Zienkiewicz and Shiomi (1984), and Zienkiewicz et al. (1990). More recently the so-called mixture theories emerged as an alternative way to establish the same set of equations governing the soil-pore fluid interaction. For a comprehensive discussion on the development of mixture theories, the reader is referred to de Boer (1996).

Generally, two-phase problems in MPM are analyzed using either a two-phase single-point or a two-phase double-point approach (see Figure 2.1). The single-point approach follows Biot's theory considering the soil as a homogeneous solid phase with pores to permit fluid mass influx. A single set of particles carries the information of both solid and water phases. Typical applications include consolidation and failure of saturated slopes due to infiltration (e.g., Abe et al., 2014).

In the double-point approach each constituent of the soil is represented independently by separate particle sets. The interaction between water and solid is accounted for through drag forces. Due to the increased number of material points required, it is computationally more expensive than the single-point approach. Application examples include liquefaction of soil and soil-free water interactions (e.g., failure of submerged slopes). The governing equations are derived from mixture theory, which postulates that water and solid particles can occupy the same position simultaneously, as illustrated in Figure 2.6. A detailed derivation of the governing equations can be found in Bandara and Soga (2015).

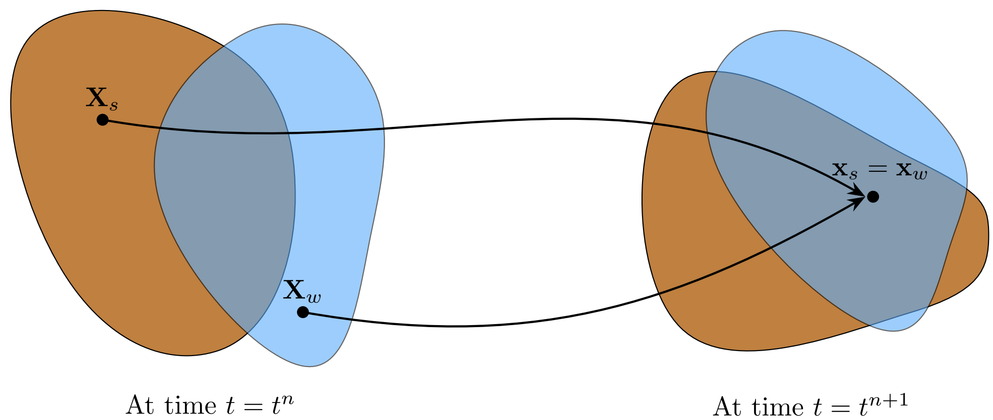

Figure 2.6: Solid and water moving independently in the two-phase double-point formulation.

2.3.2 Governing Equations

To establish the governing equations for the coupled hydro-mechanical behavior first we need to identify the type of formulation to be implemented. A wide variety of formulations are available in the literature (Jeremić et al., 2008); however, the most commonly used one is the solid displacement–water pressure, or $\mathbf{u} - p$, formulation. In this formulation, only the acceleration of the pore water relative to the solid skeleton is neglected (i.e., $\partial\mathbf{v}/\partial t \approx \partial\mathbf{w}/\partial t$), while the inertia of the mixture is retained. Here $\mathbf{v}$ and $\mathbf{w}$ denote the solid skeleton and pore water velocities, respectively. According to Zienkiewicz et al. (1980), this formulation is valid for quasi-static and low-frequency dynamic problems, such as consolidation and earthquake loading. A typical example is Terzaghi's classical consolidation equation.

The sudden application of a load to a saturated porous medium generates two distinct compression waves. One is a fast undrained wave in which the solid skeleton and pore water move nearly together when the permeability is very low. The other is a highly damped consolidation wave that can be observed in very stiff porous material, like concrete (Verruijt, 2010). van Esch et al. (2011) showed that the $\mathbf{u} - p$ formulation, despite its widespread use, fails to capture the second wave in dynamic problems. Indeed, only when a solid velocity–water velocity, or $\mathbf{v} - \mathbf{w}$, formulation (Verruijt, 2010) is used can the coupled behavior be effectively captured, and it will therefore be the primary focus herein.

The governing equations (i.e., conservation of mass, conservation of momentum, and the constitutive relation) for the two-phase MPM are a natural extension of the standard one-phase MPM. Thus, we shall only focus on the underlying assumptions used to obtain the governing equations and the physical interpretation of each term. A thorough development of the $\mathbf{v} - \mathbf{w}$ formulation in MPM applications is presented in Al-Kafaji (2013). To maintain consistency in notation we will use $\mathbf{v}_s$ (instead of $\mathbf{v}$) to denote the solid velocity and $\mathbf{v}_w$ (instead of $\mathbf{w}$) to denote the pore water velocity. Additionally, the sign convention of solid mechanics is adopted throughout this thesis, with stresses and pore pressures positive in tension. Compressive stresses and pore pressures are therefore negative, and suction corresponds to a positive liquid pressure.

Balance of Mass

The basic equation for mass balance of the solid material can be expressed as

$$\frac{\overset{s}{D}\bar{\rho}_s}{Dt} + \bar{\rho}_s \text{div}(\mathbf{v}_s) = 0 \tag{2.48}$$

where, as before, $\bar{\rho}_s = (1-n)\rho_s$ denotes the average density of solid grains and $\mathbf{v}_s$ is the solid particle velocity. The superscript s indicates that the material derivative is taken with respect to the solid phase. Equation (2.48) can now be expanded using the product rule of differentiation,

$$n\frac{\overset{s}{D}\rho_s}{Dt} + \rho_s\frac{\overset{s}{D}n}{Dt} + (1-n)\rho_s \text{div}(\mathbf{v}_s) = 0 \tag{2.49}$$

In most geotechnical applications the solid grains are assumed incompressible ($\frac{\overset{s}{D}\rho_s}{Dt} \approx 0$), and thus balance of mass for the solid phase reduces to

$$\frac{\overset{s}{D}n}{Dt} = (1-n)\,\text{div}(\mathbf{v}_s) \tag{2.50}$$

which basically describes the change of porosity in time.

Similarly, mass balance for the pore water is given by

$$\frac{\overset{s}{D}\bar{\rho}_w}{Dt} + \bar{\rho}_w \mathrm{div}(\mathbf{v}_w) + \mathrm{grad}(n\rho_w) \cdot (\mathbf{v}_w - \mathbf{v}_s) = 0 \tag{2.51}$$

where the last term on the left-hand side appears due to the movement of pore water relative to the solid phase. Since $\bar{\rho}_w = n\rho_w$, equation (2.51) can be expanded as

$$n\frac{\overset{s}{D}\rho_w}{Dt} + \rho_w \frac{\overset{s}{D}n}{Dt} + n\rho_w \mathrm{div}(\mathbf{v}_w) + \mathrm{grad}(n\rho_w) \cdot (\mathbf{v}_w - \mathbf{v}_s) = 0 \tag{2.52}$$

By combining equation (2.50) and equation (2.52) we can easily eliminate the time derivative of porosity. Additionally, we assume a linear compressibility relation for the water,

$$\frac{d\rho_w}{dp} = -\frac{\rho_w}{K_w} \tag{2.53}$$

where p is the pore pressure and K_w is the bulk modulus of water. With these assumptions we arrive at the following expression

$$\begin{aligned} \frac{\overset{s}{D}p}{Dt} = \frac{K_w}{n} &[(1-n)\,\mathrm{div}(\mathbf{v}_s) + n\,\mathrm{div}(\mathbf{v}_w)] \\ &+ \frac{K_w}{n\rho_w} \mathrm{grad}(n\rho_w) \cdot (\mathbf{v}_w - \mathbf{v}_s) \end{aligned} \tag{2.54}$$

which describes mass conservation of both water and solid particles. Equation (2.54) is in agreement with the *storage equation* from linear poroelasticity theory, see Verruijt (2010). The expression above can be further simplified by assuming the spatial variation of water mass density to be negligible ($\mathrm{grad}(n\rho_w) \approx 0$) or the relative velocity of water with respect to the solid to be zero ($\mathbf{v}_w - \mathbf{v}_s \approx 0$).

Balance of Linear Momentum

Equations of linear momentum for a saturated medium must be developed for solid particles, pore water, and the mixture as a whole. First, the total stress tensor must be split into two parts, each corresponding to a constituent of the material. The stress portion carried by the solid and water is given according to Lewis and Schrefler (1998) as

$$\boldsymbol{\sigma}_s = \boldsymbol{\sigma}' + (1-n)\mathbf{m}p \tag{2.55}$$

$$\boldsymbol{\sigma}_w = n\mathbf{m}p \tag{2.56}$$

where $\boldsymbol{\sigma}'$ is the effective stress tensor, and $\mathbf{m} = [1\ 1\ 1\ 0\ 0\ 0]^{\mathrm{T}}$ is the second-order identity tensor in Voigt notation. Thus we can write the momentum equation for the mixture as

$$n\rho_w\mathbf{a}_w + (1-n)\rho_s\mathbf{a}_s = \mathrm{div}(\boldsymbol{\sigma}) + \rho\mathbf{g} \tag{2.57}$$

and for the water phase

$$n\rho_w\mathbf{a}_w = n\,\mathrm{grad}(p) - \frac{n^2\mu_d}{\kappa_w}(\mathbf{v}_w - \mathbf{v}_s) + n\rho_w\mathbf{g} \tag{2.58}$$

where $\mathbf{a}_w$ and $\mathbf{a}_s$ denote the water and solid accelerations, μ_d is the dynamic viscosity of water, and κ_w is the intrinsic permeability, which can be converted into Darcy's permeability using the relation $k = (\rho_w g/\mu_d)\kappa_w$. The second term on the right-hand side of equation (2.58) accounts for the energy dissipated by the relative motion between the two phases and is referred to as the *drag force*.

Note that the above equations assume that Terzaghi's effective stress concept is valid, that spatial variations of porosity and liquid density are negligible, and that water flow is governed by Darcy's law.

It can be easily shown that balance of linear momentum for the solid phase may be obtained by subtraction of the water part equation (2.58) from the mixture equation (2.57), yielding

$$(1-n)\rho_s\mathbf{a}_s = \mathrm{div}(\boldsymbol{\sigma}') + (1-n)\,\mathrm{grad}(p) + \frac{n^2\mu_d}{\kappa_w}(\mathbf{v}_w - \mathbf{v}_s) + (1-n)\rho_s\mathbf{g} \tag{2.59}$$

To summarize, the governing equations for the two-phase MPM consist of the storage equation equation (2.54), momentum balance for the mixture equation (2.57) and water equation (2.58), and a constitutive relation for the solid skeleton.

Boundary Conditions

The coupled $\mathbf{v}-\mathbf{w}$ (or $\mathbf{v}_w-\mathbf{v}_s$) formulation requires the definition of boundary conditions for both solid and water. The domain boundary can be divided into

$$\partial\Omega = \partial\Omega^u \cup \partial\Omega^\tau = \partial\Omega^w \cup \partial\Omega^p \tag{2.60}$$

where $\partial\Omega^u$ denotes the prescribed displacement (velocity) on the solid boundary and $\partial\Omega^\tau$ is the prescribed total stress. The water phase boundary consists of a prescribed water displacement (velocity) on $\partial\Omega^w$ and pore pressure on $\partial\Omega^p$. The following condition must also be satisfied,

$$\partial\Omega^u \cap \partial\Omega^\tau = \emptyset, \quad \partial\Omega^w \cap \partial\Omega^p = \emptyset \tag{2.61}$$

Initial Conditions

The initial conditions for the solid and water velocities are expressed as

$$\mathbf{v}_s(\mathbf{x}, t=0) = \mathbf{v}_{s_0} \quad \text{and} \quad \mathbf{v}_w(\mathbf{x}, t=0) = \mathbf{v}_{w_0} \tag{2.62}$$

respectively. The total stress and pore pressure at the initial time are given by

$$\boldsymbol{\sigma}(\mathbf{x}, t=0) = \boldsymbol{\sigma}_0 \quad \text{and} \quad p(\mathbf{x}, t=0) = p_0 \tag{2.63}$$

From Strong to Weak Form

The momentum balance equation of the mixture equation (2.57) and water equation (2.58) can be converted to a weak form using the weighted residual method. The procedure is identical to the one presented in Section 2.2.1 and will not be repeated here. Note that the water momentum equation equation (2.58) is first divided by the porosity n, which is admissible since spatial variations of porosity are neglected. The resulting weak form expression for the mixture is given by

$$\begin{aligned}\int_{\Omega} \delta\mathbf{v} \cdot (1-n)\rho_s \mathbf{a}_s \,\mathrm{d}V + \int_{\Omega} \delta\mathbf{v} \cdot n\rho_w \mathbf{a}_w \,\mathrm{d}V = \\ \int_{\partial\Omega^{\tau}} \delta\mathbf{v} \cdot \hat{\boldsymbol{\tau}} \,\mathrm{d}S - \int_{\Omega} \mathrm{grad}(\delta\mathbf{v}) : \boldsymbol{\sigma} \,\mathrm{d}V + \int_{\Omega} \delta\mathbf{v} \cdot \rho\mathbf{g} \,\mathrm{d}V\end{aligned} \tag{2.64}$$

and for the water,

$$\begin{aligned}\int_{\Omega} \delta\mathbf{v} \cdot \rho_w \mathbf{a}_w \,\mathrm{d}V = \int_{\partial\Omega^{p}} \delta\mathbf{v} \cdot \hat{\boldsymbol{p}} \,\mathrm{d}S \\ - \int_{\Omega} \mathrm{div}(\delta\mathbf{v}) \cdot p \,\mathrm{d}V + \int_{\Omega} \delta\mathbf{v} \cdot \rho_w \mathbf{g} \,\mathrm{d}V - \int_{\Omega} \delta\mathbf{v} \cdot \frac{n\mu_d}{\kappa_w} (\mathbf{v}_w - \mathbf{v}_s) \,\mathrm{d}V\end{aligned} \tag{2.65}$$

In the above, $\mathbf{a}_s$, $\mathbf{a}_w$, $\mathbf{v}_s$, and $\mathbf{v}_w$ are the phase accelerations and velocities. $\hat{\boldsymbol{p}} = p \cdot \mathbf{n}$ is the prescribed pore pressure acting on the liquid phase pressure boundary $\partial\Omega^p$ and $\hat{\boldsymbol{\tau}} = \boldsymbol{\sigma} \cdot \mathbf{n}$ is the prescribed traction along the $\partial\Omega^\tau$ boundary. The test function $\delta\mathbf{v}$ is chosen such that it is zero along the prescribed displacement boundary of both solid and liquid phases.

2.3.3 Spatial and Temporal Discretization

Spatial Discretization

The weak forms (Equations (2.64) and (2.65)) are discretized using the Galerkin method, with identical shape functions applied to both water and solid phases. The resulting discrete form as given by Al-Kafaji (2013) is, for the total mixture,

$$\mathbf{M}_s^n \mathbf{a}_s^n = \mathbf{F}^{trac,n} + \mathbf{F}^{grav,n} - \mathbf{F}^{int,n} - \bar{\mathbf{M}}_w^n \mathbf{a}_w^n \tag{2.66}$$

and for the water,

$$\mathbf{M}_w^n \mathbf{a}_w^n = \mathbf{F}_w^{trac,n} + \mathbf{F}_w^{grav,n} - \mathbf{F}_w^{int,n} - \mathbf{F}_w^{drag,n} \tag{2.67}$$

where the mass matrices are defined as

$$\mathbf{M}_s^n \approx \int\limits_\Omega \mathbf{N}^{\mathrm{T}}(1-n)\rho_s \mathbf{N}\,\mathrm{d}V \tag{2.68}$$

$$\bar{\mathbf{M}}_w^n \approx \int\limits_\Omega \mathbf{N}^{\mathrm{T}} n\rho_w \mathbf{N}\,\mathrm{d}V \tag{2.69}$$

$$\mathbf{M}_w^n \approx \int\limits_\Omega \mathbf{N}^{\mathrm{T}} \rho_w \mathbf{N}\,\mathrm{d}V \tag{2.70}$$

Two water mass matrices appear in the discrete system: $\bar{\mathbf{M}}_w$ originates from the water inertia term of the mixture equation, whereas $\mathbf{M}_w$ originates from the water equation normalized by n. The external force vectors are

$$\mathbf{F}^{trac,n} + \mathbf{F}^{grav,n} \approx \int\limits_{\partial\Omega^\tau} \mathbf{N}^{\mathrm{T}} \hat{\boldsymbol{\tau}}\,\mathrm{d}S + \int\limits_\Omega \mathbf{N}^{\mathrm{T}} \rho \mathbf{g}\,\mathrm{d}V \tag{2.71}$$

$$\mathbf{F}_w^{trac,n} + \mathbf{F}_w^{grav,n} \approx \int\limits_{\partial\Omega^p} \mathbf{N}^{\mathrm{T}} \hat{\boldsymbol{p}}\,\mathrm{d}S + \int\limits_\Omega \mathbf{N}^{\mathrm{T}} \rho_w \mathbf{g}\,\mathrm{d}V \tag{2.72}$$

the internal force vectors are

$$\mathbf{F}^{int,n} \approx \int\limits_\Omega \mathbf{B}^{\mathrm{T}} \boldsymbol{\sigma}\,\mathrm{d}V \tag{2.73}$$

$$\mathbf{F}_w^{int,n} \approx \int\limits_\Omega \mathbf{B}^{\mathrm{T}} \mathbf{m} p\,\mathrm{d}V \tag{2.74}$$

and the drag force vector is

$$\mathbf{F}_w^{drag,n} \approx \int\limits_\Omega \mathbf{N}^{\mathrm{T}} \frac{n\rho_w g}{k}(\mathbf{v}_w - \mathbf{v}_s)\,\mathrm{d}V \tag{2.75}$$

Temporal Discretization

The primary unknowns in the discretized dynamic momentum equations are the liquid and solid accelerations. Assuming material point data and other field variables are given at the current time t^n, the solution at the next time step t^{n+1} is obtained using a symplectic Euler scheme. The updated velocities for water and solid are determined from the accelerations at time $t = t^n$, and the incremental strains are determined from those computed velocities.

2.3.4 Solution Procedure

The initialization and solution procedure for the two-phase MPM is similar to that of the one-phase MPM. The main difference is that now we have two sets of velocities and accelerations to be computed at each time step. We restrict our discussion here to the overall solution procedure of the two-phase single-point formulation. Initialization of material points and construction of mass matrices is identical to the procedure outlined in Section 2.2.3, and thus will not be discussed here. The computational cycle of the coupled MPM consists of the following steps:

1. The water acceleration vector, $\mathbf{a}_w^n$, is obtained from the water momentum balance equation (2.67).

2. The solid acceleration vector, $\mathbf{a}_s^n$, is computed from the mixture momentum balance equation (2.66) once the water acceleration is determined.

3. Particle velocities for both solid and water are updated as

$$\mathbf{v}_{s,p}^{n+1} = \mathbf{v}_{s,p}^{n} + \Delta t \sum_{i=1}^{n_{en}} N_i(\boldsymbol{\xi}_p^n)\, \mathbf{a}_{s,i}^n \tag{2.76}$$

$$\mathbf{v}_{w,p}^{n+1} = \mathbf{v}_{w,p}^{n} + \Delta t \sum_{i=1}^{n_{en}} N_i(\boldsymbol{\xi}_p^n)\, \mathbf{a}_{w,i}^n \tag{2.77}$$

4. Nodal velocities $\mathbf{v}_s$ and $\mathbf{v}_w$ are updated by solving the following equations

$$\mathbf{M}_s^n \mathbf{v}_{s,i}^{n+1} = \sum_{e=1}^{\bar{n}_{elm}} \sum_{p=1}^{n_{ep}} (1 - n_p^n) m_{s,p}\, \mathbf{N}^{\mathrm{T}}(\boldsymbol{\xi}_p^n)\, \mathbf{v}_{s,p}^{n+1} \tag{2.78}$$

$$\bar{\mathbf{M}}_w^n \mathbf{v}_{w,i}^{n+1} = \sum_{e=1}^{\bar{n}_{elm}} \sum_{p=1}^{n_{ep}} n_p^n\, m_{w,p}\, \mathbf{N}^{\mathrm{T}}(\boldsymbol{\xi}_p^n)\, \mathbf{v}_{w,p}^{n+1} \tag{2.79}$$

where $m_{s,p} = \rho_s V_p$ and $m_{w,p} = \rho_w V_p$ denote the intrinsic phase masses of a particle p.

5. Incremental strains of the liquid and solid are computed via

$$\Delta\boldsymbol{\epsilon}_{s,p}^{n+1} = \Delta t \sum_{i=1}^{n_{en}} \mathbf{B}_i(\boldsymbol{\xi}_p^n)\, \mathbf{v}_{s,i}^{n+1} \tag{2.80}$$

$$\Delta\boldsymbol{\epsilon}_{w,p}^{n+1} = \Delta t \sum_{i=1}^{n_{en}} \mathbf{B}_i(\boldsymbol{\xi}_p^n)\, \mathbf{v}_{w,i}^{n+1} \tag{2.81}$$

6. The effective stress on the solid skeleton is computed using a proper constitutive relation.

$$\boldsymbol{\sigma}_p'^{n+1} = \boldsymbol{\sigma}_p'^{n} + \Delta\boldsymbol{\sigma}'(\Delta\boldsymbol{\epsilon}_{s,p}^{n+1}) \tag{2.82}$$

7. The pore pressure is updated using the storage equation (2.54) as

$$p^{n+1} = p^n + \frac{K_{w,p}}{n_p^n}\left[(1 - n_p^n)\,\mathrm{tr}(\Delta\boldsymbol{\epsilon}_{s,p}^{n+1}) + n_p^n\,\mathrm{tr}(\Delta\boldsymbol{\epsilon}_{w,p}^{n+1})\right] \tag{2.83}$$

   where $\mathrm{tr}(\Delta\boldsymbol{\epsilon}_{s,p})$ and $\mathrm{tr}(\Delta\boldsymbol{\epsilon}_{w,p})$ represent the solid and water volumetric strain increments of a particle p, and $K_{w,p}$ is the water bulk modulus assigned to particle p.

8. Secondary properties are also updated accordingly. For example, particle volume is updated using the computed solid volumetric strain $\Delta\epsilon_{vol,s}^{n+1}$, total stress is updated by summing the effective stress and liquid pressure, and porosity is adjusted according to the mass balance of solid equation (2.50).

9. The new position of particles is updated using the solid's nodal velocities.

10. Discard the old mesh and initialize a new one for the next computational cycle.

2.4 Minimum Time Stepping Criterion

To ensure numerical stability of the explicit time integration scheme, the time step size Δt must satisfy the Courant–Friedrichs–Lewy (CFL) condition (Courant et al., 1928). For the one-phase MPM, the critical time step size is given by

$$\Delta t_{cr} = \frac{L_{min}}{c} = \frac{L_{min}}{\sqrt{E_c/\rho}} \tag{2.84}$$

where L_{min} is the smallest characteristic length of the elements, c is the wave speed, E_c is the constrained modulus of the material, and ρ is the density of the solid. This equation can also be applied to two-phase problems. However, for undrained loading conditions, E_c is replaced with the *undrained* constrained modulus $E_{c,u}$ and ρ refers to the density of the saturated mixture. Note that $E_{c,u} = E_c + K_w/n$ where K_w is the bulk modulus of water and n is the porosity.

Mieremet et al. (2016) showed that in low-permeability soils the CFL condition alone does not guarantee numerical stability in fully coupled two-phase MPM simulations. They proposed a modified stability condition given by

$$\Delta t_{cr} = \frac{-2a + \sqrt{4a^2 + 8(b + \sqrt{b^2 - 4c})}}{b + \sqrt{b^2 - 4c}} \tag{2.85}$$

where the coefficients a, b, and c are defined as

$$a = \frac{n\rho g}{(1-n)\rho_s k} \tag{2.86}$$

$$b = \frac{4[n\rho K_w + (1-2n)\rho_w K_w + n\rho_w E_c]}{n(1-n)\rho_s \rho_w L_{min}^2} \tag{2.87}$$

$$c = \frac{16 E_c K_w}{(1-n)\rho_s \rho_w L_{min}^4} \tag{2.88}$$

2.5 Numerical Stabilization and Efficiency Techniques

Explicit dynamic MPM simulations often require additional numerical treatments, either to stabilize the solution or to reduce the computational cost. Five features available in Anura3D are used in this thesis, namely local damping, mass scaling, mixed integration, strain smoothing, and liquid pressure smoothing.

2.5.1 Local Damping

A non-viscous damping of the Cundall type is applied at the grid nodes. A damping force proportional to the magnitude of the unbalanced force, acting opposite to the nodal velocity, is added to the equation of motion:

$$\mathbf{F}^{damp} = -\alpha \, \mathrm{sign}(\mathbf{v}) \left| \mathbf{F}^{ext} - \mathbf{F}^{int} \right| \tag{2.89}$$

where α is a dimensionless damping factor and all operations are performed componentwise at each node. The momentum equation equation (2.23) then becomes

$$\mathbf{M}^n \mathbf{a}^n = \mathbf{F}^{ext,n} - \mathbf{F}^{int,n} + \mathbf{F}^{damp,n} \tag{2.90}$$

Because the damping force scales with the out-of-balance force, it vanishes as equilibrium is approached, and converged quasi-static solutions are not affected. Unlike viscous damping, the energy dissipated per cycle is independent of frequency. In the two-phase formulation, the water and solid phases are damped separately. The damping force of each phase is computed from its own out-of-balance force, in which the drag force is excluded since it already provides a natural damping to the system. Both contributions enter the mixture momentum equation, and the same damping factor is used for the two phases. The appropriate value of α depends on the stage of the analysis. Relatively high values (e.g., 0.7) accelerate convergence in quasi-static stages such as gravity initialization, whereas very low values (e.g., 0.01–0.05) are recommended in transient stages, provided that their influence on the results is verified.

2.5.2 Mass Scaling

Quasi-static processes such as consolidation evolve over time scales that are orders of magnitude larger than the critical time step of Section 2.4. To reduce the number of time steps, the mass matrices in the momentum equations are scaled by a factor β, while the densities and gravity loads are kept unchanged (Al-Kafaji, 2013). The scaling thus increases only the inertia, and the stress waves travel as if the density were $\beta\rho$, so the CFL condition gives

$$\tilde{\mathbf{M}} = \beta\,\mathbf{M} \qquad \Rightarrow \qquad \tilde{c} = \sqrt{\frac{E_c}{\beta\rho}} = \frac{c}{\sqrt{\beta}} \qquad \Rightarrow \qquad \Delta\tilde{t}_{cr} = \sqrt{\beta}\,\Delta t_{cr} \tag{2.91}$$

Mass scaling is admissible only when inertial effects are negligible. The artificially increased inertia introduces noise in the initial response of the system (Ceccato, 2015), and the kinetic energy should remain small compared to the external work throughout the simulation. For the same reason, best practices advise against mass scaling in simulations of landslide propagation, since the added inertia alters the dynamics of the moving mass and shortens the computed runout.

2.5.3 Mixed Integration

As discussed in Section 2.2.2, using material points as integration points introduces quadrature errors, and particles crossing cell boundaries produce spurious oscillations in the internal forces. Mixed integration (Al-Kafaji, 2013; Beuth et al., 2011) mitigates both issues by treating filled elements as in standard FEM. When an element is fully (or nearly fully) covered by material, the internal force is evaluated by Gauss quadrature using the element-averaged stress, while partially filled elements retain material point integration,

$$\mathbf{F}_e^{int} = \begin{cases} \displaystyle\sum_{p=1}^{n_{ep}} \mathbf{B}^{\mathrm{T}}(\boldsymbol{\xi}_p)\,\boldsymbol{\sigma}_p V_p & \text{partially filled element} \\[2ex] \mathbf{B}^{\mathrm{T}}(\boldsymbol{\xi}_g)\,\bar{\boldsymbol{\sigma}}_e\,V_e & \text{fully filled element} \end{cases} \tag{2.92}$$

where

$$\bar{\boldsymbol{\sigma}}_e = \frac{\sum_{p=1}^{n_{ep}} \boldsymbol{\sigma}_p V_p}{\sum_{p=1}^{n_{ep}} V_p} \tag{2.93}$$

is the volume-averaged particle stress of the element, V_e is the element volume, and $\boldsymbol{\xi}_g$ is the location of the single Gauss point of the low-order elements adopted here. Interior elements are always treated as fully filled, while a boundary element is considered fully filled when its particle volumes occupy more than a prescribed fraction of the element volume. The averaged stress and state variables are then assigned to all particles of the element. The averaging smooths the internal forces as particles cross element boundaries and reduces the quadrature error discussed in Section 2.2.2. Since integrating over the full element volume does not exactly conserve energy, mixed integration is primarily intended for quasi-static and slow problems rather than wave-dominated ones.

2.5.4 Strain Smoothing

Linear elements with a single integration point are prone to volumetric locking. Their shape functions cannot represent volume-preserving deformation fields, so when the material response is nearly incompressible, as in undrained saturated soil, the mesh exhibits an artificially stiff response accompanied by spurious stress oscillations. To mitigate locking, the nodal mixed discretization technique (Detournay & Dzik, 2006) is adopted here. The strain increment is decomposed into a deviatoric part and a volumetric part, and only the volumetric part is smoothed over neighboring elements. First, a nodal value is computed by volume-averaging over the $n_{el,i}$ elements attached to node i,

$$\Delta\bar{\epsilon}_{vol,i} = \frac{\sum_{e=1}^{n_{el,i}} \Delta\epsilon_{vol,e} V_e}{\sum_{e=1}^{n_{el,i}} V_e} \tag{2.94}$$

then the smoothed element value is recovered as the average of its nodal values,

$$\Delta\bar{\epsilon}_{vol,e} = \frac{1}{n_{en}} \sum_{i=1}^{n_{en}} \Delta\bar{\epsilon}_{vol,i} \tag{2.95}$$

Finally, the strain increment of every particle in the element is recomposed from its unmodified deviatoric part $\Delta\mathbf{e}_p$ and the smoothed volumetric part, i.e., $\Delta\boldsymbol{\epsilon}_p = \Delta\mathbf{e}_p + \frac{1}{3}\Delta\bar{\epsilon}_{vol,e}\,\mathbf{m}$. In effect, the volumetric response is evaluated over a patch of elements rather than a single element, which relaxes the excessive kinematic constraint and has proven effective in mitigating locking in (nearly) incompressible deformations (Al-Kafaji, 2013).

2.5.5 Liquid Pressure Smoothing

In the two-phase formulation, pore pressures are updated at the particles from the volumetric strain increments through the storage equation equation (2.54). Because water is nearly incompressible, its large bulk modulus amplifies even small errors in the volumetric strains into spurious oscillations of the pore pressure field. These oscillations are mitigated by smoothing the pressure increments in a manner analogous to the strain smoothing above. A nodal increment is first computed by volume-averaging the particle values over the elements attached to node i,

$$\Delta \bar{p}_i = \frac{\sum_{e=1}^{n_{el,i}} \sum_{p=1}^{n_{ep}} \Delta p_p \, V_p}{\sum_{e=1}^{n_{el,i}} \sum_{p=1}^{n_{ep}} V_p} \tag{2.96}$$

and the element increment, obtained by averaging the nodal values,

$$\Delta \bar{p}_e = \frac{1}{n_{en}} \sum_{i=1}^{n_{en}} \Delta \bar{p}_i \tag{2.97}$$

is assigned to all particles within the element.

2.6 Verification Problems

This section presents two benchmark problems to verify the existing coupled MPM formulation implemented in the open-source code Anura3D (2025). The first problem examines wave propagation in a saturated porous medium and the second is Terzaghi's one-dimensional consolidation problem, a classical benchmark in geomechanics. Numerical results are compared with analytical solutions to demonstrate the accuracy and robustness of the dynamic MPM formulation for geomechanical applications. Pore pressures in these benchmarks are reported as positive in compression, following common geotechnical practice.

Material parameter	Description	Value
E'	Effective Young's modulus [kPa]	10000
ν'	Effective Poisson's ratio [–]	0.3
n	Porosity [–]	0.4
K_w	Bulk modulus of water [kPa]	2.15×10^6
ρ_s	Density of solid grains [kg/m^3]	2650
ρ_w	Density of water [kg/m^3]	1000
κ_w	Intrinsic permeability [m^2]	1.0214×10^{-12}
μ_d	Dynamic viscosity of water [kPa·s]	1.002×10^{-6}

Table 2.1: Material parameters for the one-dimensional wave propagation problem.

2.6.1 Undrained Wave Propagation

A 1.0 m long saturated soil column is subjected to a sudden compressive load of $\sigma_0 = 1\,\text{kPa}$ at the top surface, generating an undrained pressure wave that propagates through the medium. The load is kept constant and gravity effects are neglected. Material properties of the solid and water are summarized in Table 2.1. Since the load is suddenly applied, an undrained soil response is expected. The analytical solutions for pore pressure and effective stress are derived from the governing equations of porous media, which, when reduced to the one-dimensional case, become (Verruijt, 2010):

$$p = \frac{1/E_c}{1/E_c + n/K_w}\,\sigma_0 \tag{2.98}$$

$$\sigma' = \frac{n/K_w}{1/E_c + n/K_w}\,\sigma_0 \tag{2.99}$$

where $E_c = E'(1-\nu')/[(1+\nu')(1-2\nu')]$ is the constrained modulus. These expressions assume incompressible solid grains but take into account the compressibility of the pore fluid. Typically, for soft saturated soils, the pore fluid compressibility dominates the response, leading to a pore pressure close to the applied load and a small effective stress. Indeed, the analytical solution of this problem gives a pore pressure of $p = 0.9975\,\text{kPa}$ and an effective stress of $\sigma' = 0.0025\,\text{kPa}$. The stress wave propagates at a speed of

$$c_{p,u} = \sqrt{\frac{E_{c,u}}{\rho}} = \sqrt{\frac{E_c + K_w/n}{n\rho_w + (1-n)\rho_s}} \tag{2.100}$$

where $E_{c,u}$ is the undrained constrained modulus and ρ is the density of the saturated soil. For the considered material parameters the wave speed is $c_{p,u} = 1645\,\text{m/s}$ and would reach a particle located at a depth of 0.5 m in approximately 3.04×10^{-4} s.

The numerical model consists of a soil column of height 1.0 m and a width of 0.001 m, discretized using a very fine mesh to capture the dynamic response properly. In this example, 2000 triangular elements with three particles per element are used. The critical time step for stability was approximately $\Delta t_{cr} = 3.67 \times 10^{-7}$ s. To ensure stability, a Courant number of 0.98 was used, i.e., the time step was set to $\Delta t = 0.98\,\Delta t_{cr}$. Restraints in the normal direction were applied at the bottom boundary and along the sides for both solid and fluid phases. A vertical load of $\sigma_0 = 1\,\text{kPa}$ was applied at the top boundary of the solid phase, while the pore pressure at the top was kept zero. No local damping or mass scaling is used in this example.

The numerical results for pore pressure and effective stress of a material point located at a depth of 0.5 m are shown in Figure 2.7. As expected, the stress waves reach the observation point at approximately $t = 3.04 \times 10^{-4}$ seconds, which is consistent with the theoretical wave speed. The pore pressure rises sharply to about $p = 0.9975\,\text{kPa}$, matching the analytical solution. Once the wave reaches the bottom boundary it reflects and travels back, doubling the stress magnitude at $t = 9.12 \times 10^{-4}$ s. Because the top boundary is free from any fixity, the compressive wave is reflected back as a tensile wave, causing a drop in pore pressure.

2.6.2 Terzaghi's Consolidation Theory

The second benchmark problem consists of a 1.0 m high saturated soil column subjected to a load of $\sigma_0 = 10\,\text{kPa}$ applied instantaneously at the top surface. Again, the bottom boundary

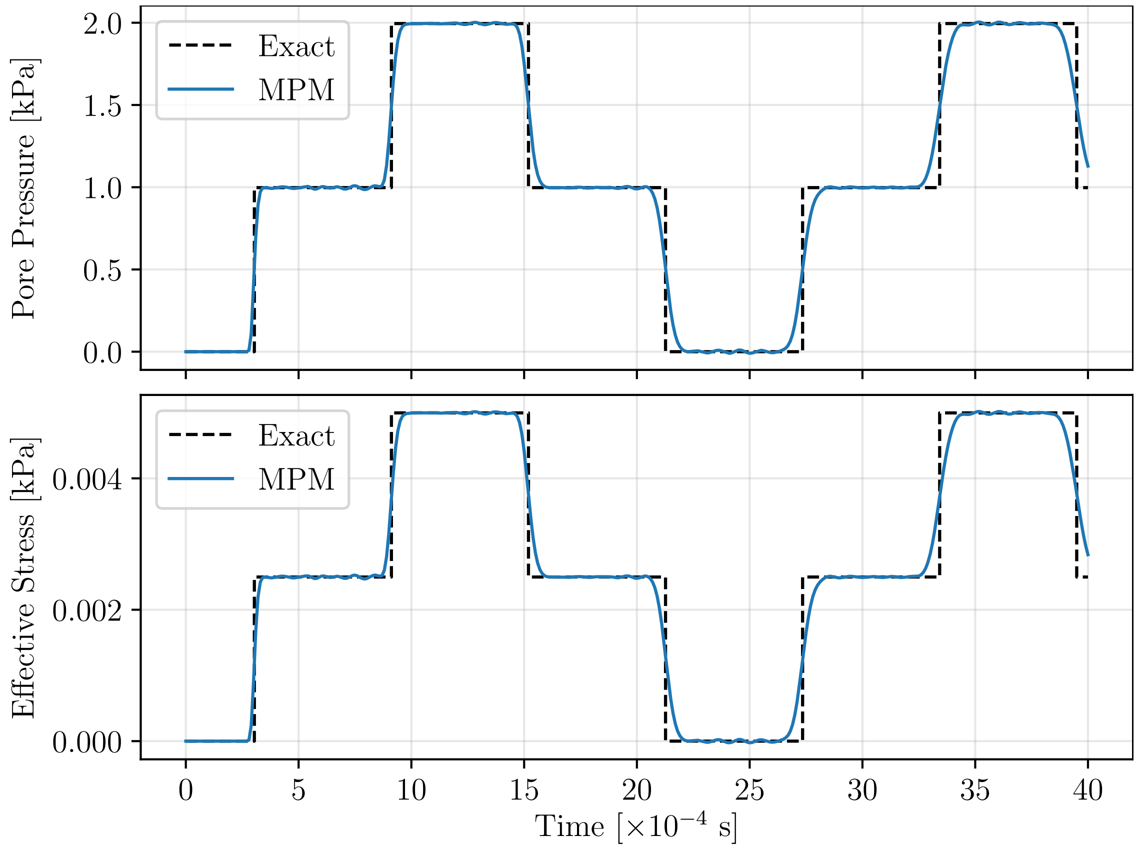

Figure 2.7: Pore pressure and effective stress evolution of a material point located at a depth of 0.5 m.

is impermeable and the sides are restrained in the normal direction for both solid and fluid phases. The partial differential equation governing the dissipation of excess pore pressure in fully one-dimensional consolidation was derived by Terzaghi (1925) as:

$$\frac{\partial p}{\partial t} = c_v \frac{\partial^2 p}{\partial z^2} \tag{2.101}$$

where c_v is the coefficient of consolidation defined as

$$c_v = \frac{k}{\rho_w g (1/E_c + n/K_w)} \tag{2.102}$$

Terzaghi's theory of consolidation assumes both solid grains and water to be incompressible, neglecting the term related to water compressibility in Equation (2.102); nevertheless, this term is included in the analysis. Material properties for this problem are sum-

Material parameter	Description	Value
E'	Effective Young's modulus [kPa]	10000
ν'	Effective Poisson's ratio [–]	0.3
n	Porosity [–]	0.4
K_w	Bulk modulus of water [kPa]	2.15×10^6
ρ_s	Density of solid grains [kg/m^3]	2650
ρ_w	Density of water [kg/m^3]	1000
κ_w	Intrinsic permeability [m^2]	1.0214×10^{-13}
μ_d	Dynamic viscosity of water [kPa·s]	1.002×10^{-6}

Table 2.2: Material parameters for the one-dimensional consolidation problem.

marized in Table 2.2. The permeability selected yields a coefficient of consolidation of $c_v \approx 1.37 \times 10^{-3}\,\mathrm{m}^2/\mathrm{s}$. This value represents the rate at which excess pore pressure dissipates. In many soils it is considerably lower, resulting in a consolidation process lasting months or even years.

The numerical model consists of a column of height 1.0 m and a width of 0.1 m, discretized using 500 triangular elements with three particles per element. The critical time step for stability is $\Delta t_{cr} = 1.48 \times 10^{-5}$ s. Figure 2.8 shows the normalized pore pressure, p/p_0 with $p_0 = \sigma_0$, along the column depth for different values of a dimensionless time factor T defined by

$$T = \frac{c_v t}{H^2} \tag{2.103}$$

where H is the maximum drainage path length and t is time. The analytical solution is given by

$$\frac{p}{p_0} = \frac{4}{\pi} \sum_{k=1}^{\infty} \frac{1}{2k-1} \sin\left[(2k-1)\,\frac{\pi}{2}\,\frac{z}{H}\right] \exp\left[-(2k-1)^2\,\frac{\pi^2}{4}\,T\right] \tag{2.104}$$

where z is the depth measured from the drained top surface. The computed pore pressures coincide with the analytical solution, except for a minor mismatch at an early time ($T = 0.2$) caused by dynamic wave oscillations. These oscillations eventually damp out and the

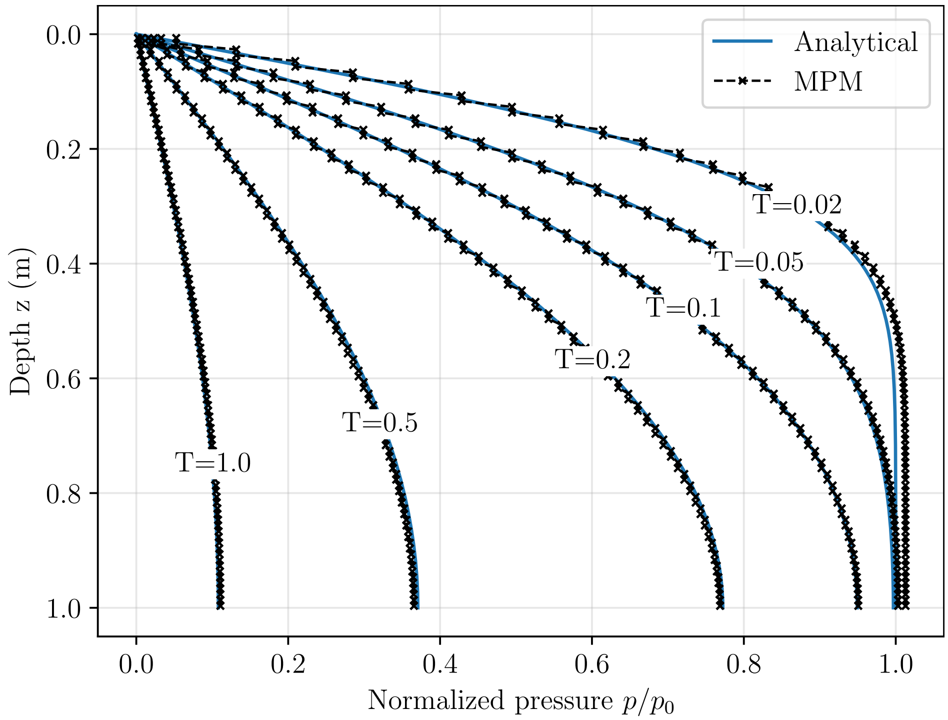

Figure 2.8: Normalized excess pore pressure along the depth of the soil column at different dimensionless time factors.

isochrones at subsequent time factors agree with the analytical solution. Local damping with a factor of $\alpha = 0.01$ is used to reduce high-frequency oscillations; it is kept minimal to avoid overestimating pore pressures during the later stages of consolidation. A mass scaling factor of $\beta = 40$ is applied to increase the critical time step.

Figure 2.9 shows the evolution of excess pore pressure at three different depths within the soil column, at the top ($z = 0$ m), middle ($z = 0.5$ m), and bottom ($z = 1.0$ m). As expected, the pore pressure at the top boundary drops to zero almost immediately due to the free drainage condition, while the consolidation at the bottom boundary continues beyond $t = 800\,\mathrm{s}$.

Finally, Figure 2.10 shows the degree of consolidation U with respect to the dimensionless time factor T. For this problem, the final settlement is $u_\infty = \sigma_0 H / E_c \approx 0.74\,\mathrm{mm}$, where $\sigma_0 = 10\,\mathrm{kPa}$, $H = 1.0$ m, and $E_c = 13\,462\,\mathrm{kPa}$. Numerical results obtained using MPM are

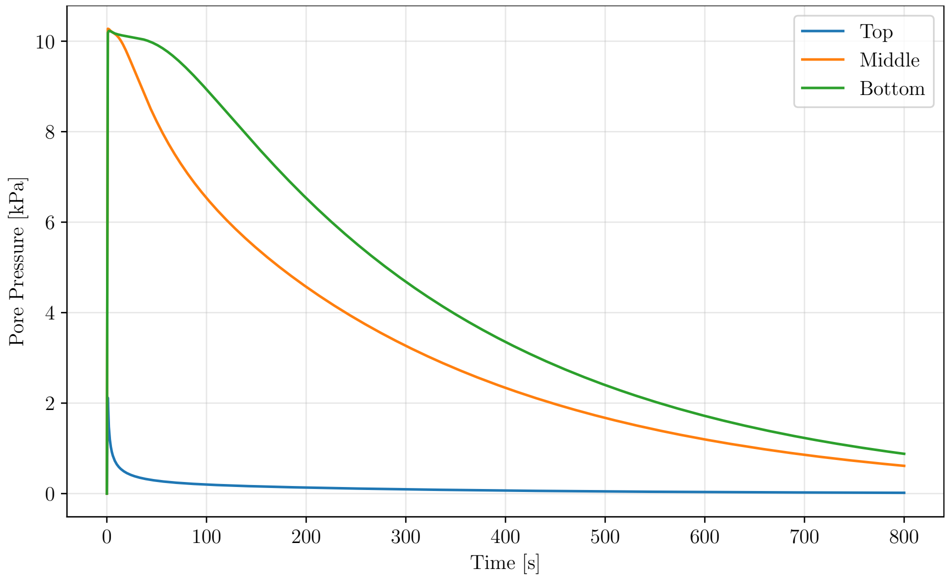

Figure 2.9: Excess pore pressure evolution at different depths within the soil column.

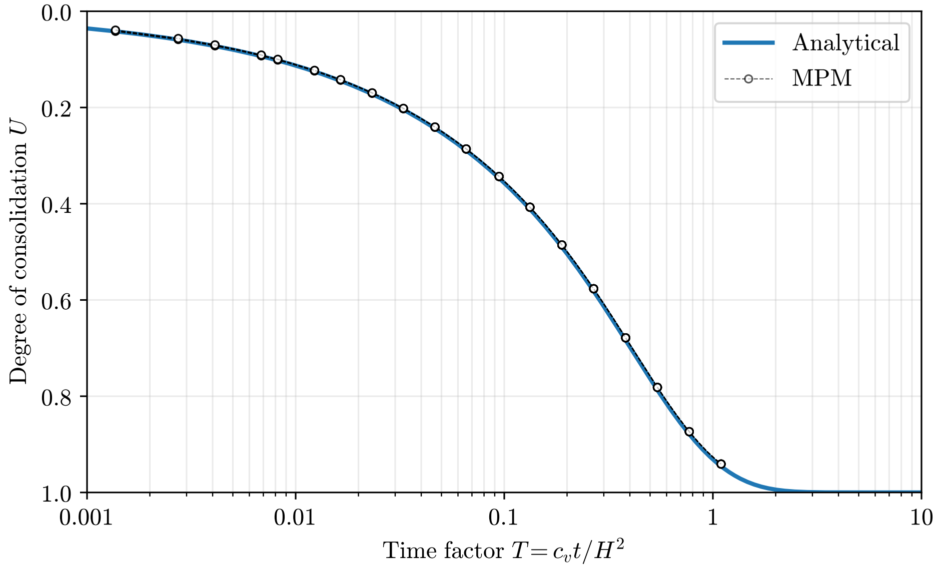

Figure 2.10: Degree of consolidation as a function of the time factor.

consistent with the analytical solution

$$U = 1 - \frac{8}{\pi^2} \sum_{k=1}^{\infty} \frac{1}{(2k-1)^2} \exp\left[-(2k-1)^2 \frac{\pi^2}{4} T\right], \tag{2.105}$$

and after 800 s of simulation time, the degree of consolidation reached approximately 95%.

Chapter 3

Stability Analysis of Dry and Unsaturated Soil Slopes

3.1 Introduction

The Material Point Method has shown great success in simulating real slope failure events (Kohler & Puzrin, 2022; Macedo et al., 2024; Nguyen et al., 2022; Pinyol et al., 2018; Yerro et al., 2015; Zabala & Alonso, 2011). Pre-failure stability analysis, however, has received far less attention, largely because MPM is regarded as a large-deformation method and is commonly used to simulate the onset of failure and the resulting runout. Moreover, the majority of existing MPM formulations are dynamic and employ explicit time integration schemes, which makes the simulation of long processes computationally expensive. This limitation, however, is expected to become less significant as open-source, GPU-accelerated MPM codes become more widely available.

Traditional methods of slope stability analysis, such as limit equilibrium methods (LEMs), FEM, and the finite difference method (FDM), often seek a single scalar-valued stability indicator known as the factor of safety (FoS), defined as the ratio of the soil's available shear strength to the shear stress required for equilibrium along a potential failure surface. A slope is considered stable when FoS > 1, unstable when FoS < 1, and at a critical state when FoS $= 1$. Limit equilibrium methods, such as the ordinary method of slices (Fellenius, 1936), Bishop's simplified method (Bishop, 1955), and Spencer's method (Spencer, 1967), represent the oldest approach to stability analysis. It is well known that these methods (i) are statically indeterminate, (ii) assume rigid-perfectly plastic behavior, and (iii) require prescribing a potential slip surface in advance. Nevertheless, they remain widely used today owing to their simplicity and effectiveness in problems with simple geometry and loading conditions.

In the 1970s, Zienkiewicz et al. (1975) introduced the strength reduction method (SRM), in which the soil's shear strength parameters (i.e., effective cohesion and friction angle) are iteratively reduced until equilibrium can no longer be reached. The technique became increasingly practical as computational tools improved over the years, and it is now the standard approach when FEM is applied to slope stability problems (Dawson et al., 1999; Griffiths & Lane, 1999; Matsui & San, 1992). A key advantage of FEM over LEMs is that no assumption regarding the slip surface is required, as failure develops from the stress response. Since the SRM is an iterative procedure, failure is generally defined when one of the following criteria is met: (i) non-convergence of the numerical scheme after a specified tolerance is exceeded (Zienkiewicz et al., 1975), (ii) a rapid increase of the maximum nodal displacement (Griffiths & Lane, 1999), or (iii) the formation of a continuous plastic zone extending through the slope (Matsui & San, 1992). The FEM solutions in this chapter are obtained using RS2 software by Rocscience, which employs the first criterion to determine the critical strength reduction factor (SRF).

Using the strength reduction technique in MPM to determine the safety factor is not straightforward. This is because MPM can handle large deformations without suffering from mesh distortion, so the non-convergence criterion adopted in FEM is not applicable. Existing SRM-MPM studies have instead defined failure directly from the displacement-SRF curve, commonly by identifying the SRF at which the displacement increases abruptly (J.-H. Wang

& Xu, 2025; Xu et al., 2022; P. Zhang et al., 2022). In many cases, however, the displacement increases gradually, without a clear transition from stable to unstable conditions. To address this, Feng and Xu (2021) fitted one straight line through the small-displacement portion of the curve and another through the rapidly increasing portion, and defined the FoS as the SRF at which the two lines intersect.

These studies demonstrate the feasibility of applying the SRM within MPM. However, they are limited to dry slopes, except for J.-H. Wang and Xu (2025), who obtained the pore-pressure distribution from a separate seepage analysis. The sensitivity of the computed FoS to discretization also remains unclear, as each study considered only a single mesh and material-point configuration.

The objective of this chapter is to investigate the capability of MPM to serve as a complete tool for slope stability analysis, in which the factor of safety, the failure mechanism, and the subsequent deformation are obtained within a single framework. To this end, two cases are considered: a dry slope and an unsaturated slope under steady-state seepage. For the dry case, a one-phase single-point MPM formulation is used. For the unsaturated case, a fully coupled two-phase single-point MPM formulation is employed to capture the interaction between the solid skeleton and the pore fluid. The computed factors of safety and failure mechanisms are compared with those obtained from conventional methods, namely FEM and, for the dry slope, Spencer's method. Their sensitivity to the mesh size and the number of material points is also examined.

3.2 Governing Equations for Unsaturated Soils

The dry slope is analyzed with the one-phase formulation, in which the soil is treated as a single continuum and the pore fluid plays no role. The unsaturated slope requires a coupled description in which the solid skeleton and the pore water are represented separately and interact through the effective stress and through the drag force generated by their relative motion. The formulation adopted here is the two-phase, single-point $\mathbf{v}_s$–$\mathbf{v}_w$ formulation extended by Ceccato et al. (2021) to account for variable saturation, and its governing equations are summarized below. The full derivation can be found in the original work.

Physical quantities related to different phases are distinguished by subscripts — namely, s for the solid phase, w for the water phase, and no subscript for the mixture. Unsaturated soil is a three-phase medium composed of solid particles and pore fluids, typically water and air. Assuming that pore air is freely connected to the atmosphere ($p_a = 0$) and its density is negligible ($\rho_a \approx 0$), then the total density of the mixture can be defined as

$$\rho = \bar{\rho}_s + \bar{\rho}_w = n_s\rho_s + n_w\rho_w \tag{3.1}$$

where $n_s = 1 - n$ is the volumetric concentration of solid phase, $n_w = S_w n$ is the volumetric concentration of liquid phase, S_w is the degree of saturation, n is the porosity, and ρ_s and ρ_w are the intrinsic densities. The governing equations within the MPM framework are derived under the following general assumptions: (i) solid particles are incompressible, (ii) pore water is weakly compressible, (iii) conditions are isothermal, and (iv) fluid flow is laminar.

The mass balance equations for the solid and liquid phases are expressed as

$$\frac{\overset{s}{D}\bar{\rho}_s}{Dt} + \bar{\rho}_s \mathrm{div}(\mathbf{v}_s) = 0 \tag{3.2}$$

$$\frac{\overset{s}{D}\bar{\rho}_w}{Dt} + \bar{\rho}_w \mathrm{div}(\mathbf{v}_w) + \mathrm{grad}(n\rho_w) \cdot (\mathbf{v}_w - \mathbf{v}_s) = 0 \tag{3.3}$$

where $\mathbf{v}_s$ and $\mathbf{v}_w$ denote the absolute velocity of the solid and liquid phases, respectively. The superscript indicates that the material derivative is taken with respect to the solid phase velocity. Under the assumption of incompressible solid grains, Eq. (3.2) describes the evolution of porosity with time. In Eq. (3.3), a third term arises from the relative motion of the liquid with respect to the solid skeleton. Combining Eqs. (3.2) and (3.3), and omitting intermediate derivation steps for brevity, yields the overall mass conservation of the system, i.e.,

$$n\left(S_w\frac{\partial\rho_w}{\partial p_w}+\rho_w\frac{\partial S_w}{\partial p_w}\right)\frac{\overset{s}{D}p_w}{Dt}=\mathrm{div}\left[\rho_w n S_w(\mathbf{v}_s-\mathbf{v}_w)\right]-\rho_w S_w\mathrm{div}(\mathbf{v}_s) \tag{3.4}$$

where the liquid pressure p_w is taken as a state variable. The derivative of liquid density with respect to pressure is described by a linear compressibility relation, $d\rho_w/dp_w = -\rho_w/K_w$, while the derivative of the degree of saturation with respect to pressure is obtained from the soil-water retention curve. In a fully saturated soil $S_w = 1$ and $\partial S_w/\partial p_w = 0$, and so Eq. (3.4) reduces to the storage equation of the saturated formulation, Eq. (2.54).

The dynamic equations of motion are governed by the balance of linear momentum for the liquid phase (Eq. 3.5) and the overall mixture (Eq. 3.6).

$$\bar{\rho}_w\mathbf{a}_w = n_w\mathrm{grad}(p_w)-\frac{n_w^2\mu_d}{\kappa_w}(\mathbf{v}_w-\mathbf{v}_s)+n_w\rho_w\mathbf{g} \tag{3.5}$$

$$\bar{\rho}_w\mathbf{a}_w+\bar{\rho}_s\mathbf{a}_s=\mathrm{div}(\boldsymbol{\sigma})+\rho\mathbf{g} \tag{3.6}$$

Here, $\mathbf{a}_w$ and $\mathbf{a}_s$ denote the water and solid accelerations, $\mathbf{g}$ is the gravitational acceleration vector, $\boldsymbol{\sigma}$ is the total stress tensor, μ_d is the dynamic viscosity of water, and κ_w is the intrinsic permeability, which can be converted into Darcy's permeability using the relation $k = (\rho_w g/\mu_d)\kappa_w$. The second term on the right-hand side of Eq. (3.5), also known as the drag force, accounts for the energy dissipated due to solid-fluid relative motion. The discrete form of the momentum equations can be written as

$$\tilde{\mathbf{M}}_w\,\mathbf{a}_w=\mathbf{F}_w^{\mathrm{ext}}-\mathbf{F}_w^{\mathrm{int}}-\mathbf{F}_w^{\mathrm{drag}} \tag{3.7}$$

$$\mathbf{M}_s\,\mathbf{a}_s+\mathbf{M}_w\,\mathbf{a}_w=\mathbf{F}^{\mathrm{ext}}-\mathbf{F}^{\mathrm{int}} \tag{3.8}$$

which follows from expressing Eqs. (3.5) and (3.6) in weak form and applying the Galerkin approximation with standard shape functions. $\mathbf{M}_s$, $\mathbf{M}_w$, and $\tilde{\mathbf{M}}_w$ are the lumped mass matrices of the solid and liquid; $\mathbf{F}^{\mathrm{ext}}$, $\mathbf{F}_w^{\mathrm{ext}}$, $\mathbf{F}^{\mathrm{int}}$, and $\mathbf{F}_w^{\mathrm{int}}$ are the external and internal nodal force vectors; and $\mathbf{F}_w^{\mathrm{drag}}$ is the drag force vector. For detailed definitions of these terms, the reader is referred to Ceccato et al. (2021) or section 2.3.3.

3.2.1 Boundary Conditions

In the coupled MPM formulation, boundary conditions are specified over the entire boundary, $\partial\Omega$, such that for the solid,

$$\partial\Omega = \partial\Omega_{v_s} \cup \partial\Omega_{\tau} \quad \text{and} \quad \partial\Omega_{v_s} \cap \partial\Omega_{\tau} = \emptyset, \tag{3.9}$$

where $\partial\Omega_{v_s}$ denotes the portion of the boundary where velocity is prescribed, and $\partial\Omega_{\tau}$ denotes the portion where traction is prescribed. Similarly, for the liquid,

$$\partial\Omega = \partial\Omega_{v_w} \cup \partial\Omega_{p} \quad \text{and} \quad \partial\Omega_{v_w} \cap \partial\Omega_{p} = \emptyset, \tag{3.10}$$

where liquid velocity and pore pressure are prescribed along $\partial\Omega_{v_w}$ and $\partial\Omega_{p}$, respectively. Many slope stability problems involve unsaturated soil conditions and seepage flow, for which appropriate hydraulic boundary conditions must be specified. For instance, a total head value, $\hat{H}$, can be applied to represent the water level in a reservoir. The corresponding prescribed pressure $\hat{p}_w$ is obtained from the one-dimensional energy equation,

$$\hat{H} = h_g - \frac{\hat{p}_w}{\rho_w g} \tag{3.11}$$

where h_g is the geometric head. Stresses are taken as positive in tension, hence the minus sign in Eq. (3.11). Another common condition is a potential seepage face, usually applied on the downstream slope to allow water outflow at zero pressure once the boundary becomes saturated.

3.2.2 Constitutive Relations

Although many advanced constitutive models have been proposed in the literature to describe the complex behavior of unsaturated soils (Alonso et al., 1990; Cheng et al., 2007; Chiu & Ng, 2003; Gens et al., 2006; Loret & Khalili, 2002; Mašín & Khalili, 2008), a basic elasto-plastic model based on the Mohr–Coulomb failure criterion is adopted in this chapter. This choice is motivated by the desire to focus on the slope stability methodology without introducing additional complexity from the constitutive model. Effective stresses for unsaturated soil are calculated using Eq. (3.12), where Bishop's χ parameter is taken equal to the degree of saturation, and $\mathbf{m}$ is the unit vector $[1\,1\,1\,0\,0\,0]^{\mathrm{T}}$ in 3D.

$$\boldsymbol{\sigma}' = \boldsymbol{\sigma} - \chi\, p_w \mathbf{m} \tag{3.12}$$

Taking χ equal to the degree of saturation is the definition employed in the two-phase formulation of Ceccato et al. (2021) and thus will not be modified in the present work. Alternative expressions are available in the literature, notably that of Khalili and Khabbaz (1998), in which χ is a power function of the ratio of suction to the air-entry value.

The hydraulic properties of unsaturated soil are defined by a soil–water retention curve (SWRC) and a hydraulic conductivity function (HCF). In this chapter, the HCF is assumed to be constant and equal to the saturated hydraulic conductivity, whereas the SWRC is described using the van Genuchten model,

$$S_w = S_{min} + (S_{max} - S_{min}) \left[1 + \left(\frac{p_w}{p_{ref}} \right)^{\frac{1}{1-\lambda}} \right]^{-\lambda} \tag{3.13}$$

Here, S_{max} and S_{min} represent the maximum and minimum degrees of saturation, while p_{ref} and λ are curve-fitting parameters. It is acknowledged that the assumption of a constant hydraulic conductivity is a simplification, and that a suction-dependent HCF would provide a more realistic description of unsaturated flow, particularly at low degrees of saturation. Adopting a suction-dependent conductivity in the present explicit two-phase formulation would, however, severely restrict the critical time step, rendering the computational cost of the strength-reduction analyses impractical. The same hydraulic simplifications are applied consistently in the MPM and FEM analyses, so that the comparison between the two methods is unaffected by this assumption.

3.3 Strength Reduction Method

Slope stability analysis with the shear-strength-reduction technique is performed through a series of simulations in which the soil cohesion c and friction angle ϕ are systematically reduced by a shear strength reduction factor (SRF). The trial parameters c_t and ϕ_t for each calculation are given by

$$c_t = \frac{c}{\mathrm{SRF}} \tag{3.14}$$

$$\phi_t = \arctan\left(\frac{\tan\phi}{\mathrm{SRF}}\right) \tag{3.15}$$

Initially, a sufficiently low SRF is used to ensure that the slope remains stable under self-weight. The SRF is then incrementally increased with each subsequent calculation until slope failure is identified, at which point the corresponding SRF is taken as the factor of safety. Because numerical non-convergence does not apply to the explicit MPM scheme, failure is instead defined by the onset of a rapid increase in the displacement–SRF curve. The maximum displacement in the slope is monitored, and the SRF at which the displacement begins to grow rapidly is taken as the factor of safety. If the increase is gradual and no distinct transition can be identified, as in the dry case below, the criterion of Feng and Xu (2021) is adopted: straight lines are fitted to the initial, slowly increasing and to the rapidly increasing branches of the displacement-SRF curve, and the factor of safety is defined by their intersection.

3.4 Benchmark Problems

In this section, slope stability analyses are conducted using MPM on a benchmark slope geometry inspired by Griffiths and Lane (1999). Dry and unsaturated soil conditions are examined, and the results predicted by MPM are compared with those from the FEM. The open-source MPM software Anura3D (2025) is used. Like most MPM codes available today,

Parameter	Description	Value
E'	Effective Young's modulus [kPa]	45000
ν'	Effective Poisson's ratio [–]	0.30
n	Porosity [–]	0.40
c'	Effective cohesion [kPa]	2
ϕ'	Effective friction angle [°]	30
ψ	Dilatancy angle [°]	0
ρ_s	Density of solid grains [kg/m^3]	2650

Table 3.1: Material properties of the dry soil.

Anura3D is implemented with an explicit time scheme, which makes it conditionally stable; the time increment is therefore chosen as 0.98 times the critical time step. For the coupled hydromechanical formulation, the critical time step is determined by the stability criterion of Mieremet et al. (2016), as the classical Courant–Friedrichs–Lewy condition (Courant et al., 1928) alone does not guarantee numerical convergence, especially in soils of low permeability. The local damping, mass scaling, and mixed integration techniques employed in the analyses were described in Section 2.5.

3.4.1 Case I: Dry Homogeneous Slope

Model and Calculation Stages

A homogeneous slope with an inclination of 2:1 (horizontal:vertical) is considered (Figure 3.1). The underlying foundation is 5 m thick and consists of the same material. The computational domain is discretized into 3,066 triangular elements with an average edge length of 0.75 m. Of these, 1,792 elements are active, i.e., initially occupied by material points, while the remaining elements cover the initially empty regions into which material may move during large deformation. Three material points are assigned to each active element, resulting in a total of 5,376 material points. The critical time step determined from

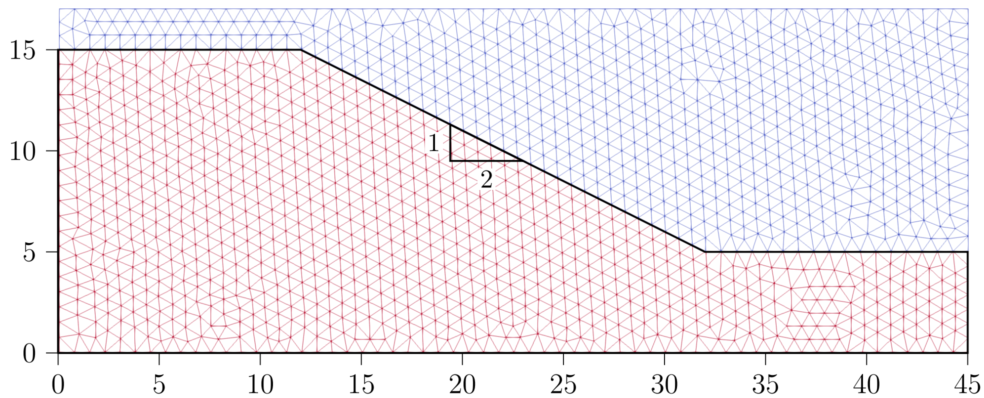

Figure 3.1: MPM model and computational mesh of the dry slope.

the CFL condition is $\Delta t_{cr} = 2.1 \times 10^{-3}$ s, and a time step of $0.98\,\Delta t_{cr}$ is adopted. Boundary conditions consist of full fixity along the bottom boundary and fixity in the normal direction along the lateral boundaries. The material properties are summarized in Table 3.1.

The slope stability analysis using MPM is performed in three stages. First, the initial stress state is established by applying gravity loading to a stress-free slope. During this stage, cohesion is temporarily increased to a very high value ($c' = 200$ kPa) to prevent material yielding, and a local damping force with a factor of $\alpha = 0.75$ is applied to accelerate convergence toward a quasi-static stress state. Next, the actual cohesion is restored, and the simulation is continued until static equilibrium is re-established under the actual strength parameters. In this example, 18 s was sufficient. Finally, the shear strength reduction technique is applied according to equations (3.14) and (3.15), and the response is recorded over a 5-s window. The SRF is initially set to 1.00 and increased by $\Delta\mathrm{SRF} = 0.05$ in each subsequent calculation. Near the transition to large deformations, the increment is reduced to $\Delta\mathrm{SRF} = 0.01$. The local damping factor is reduced to $\alpha = 0.05$, since higher damping can alter the failure mechanism and the computed deformations (Ceccato et al., 2024). The influence of lower and zero damping is examined in Section 3.4.1.

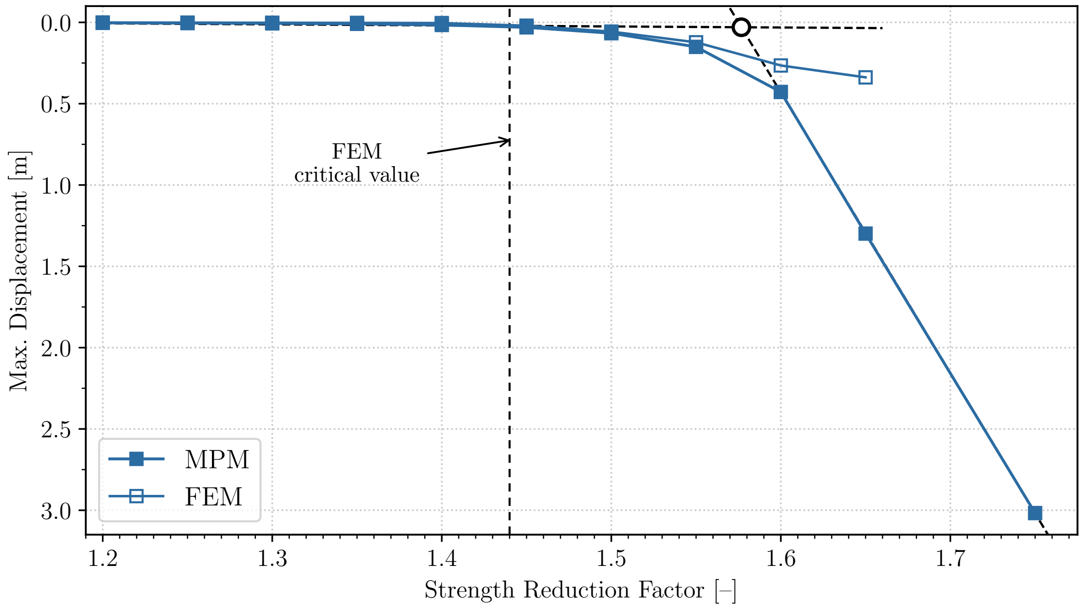

Figure 3.2: Maximum displacement versus strength reduction factor for the dry slope. The dashed lines show the bilinear construction used to estimate the factor of safety.

Displacement Response and Factor of Safety

Figure 3.2 shows the relationship between the applied SRF and the maximum displacement recorded after 5 s. The curve remains essentially flat up to approximately SRF = 1.45, beyond which the displacement increases more rapidly with each increment. Because no distinct turning point is observed, the FoS is estimated using a bilinear construction (Feng & Xu, 2021). One straight line is fitted to the initial branch of the curve (SRF $\leq$ 1.45), and another is fitted to the final branch (SRF = 1.60–1.75). The intersection of the two lines gives $\text{FoS}_{\text{MPM}} \approx 1.58$.

The same slope is analyzed using FEM with identical geometry, unit weight, and Mohr–Coulomb parameters. The domain is discretized into 4,514 quadrilateral elements, and the strength is reduced in increments of 0.01 until the solution fails to converge. Based on the last converged solution, the critical value is determined as $\text{FoS}_{\text{FEM}} = 1.44$. The slope stability is also evaluated using LEM in Slide2, where the potential sliding mass is divided

Approach	Solution method	FoS	Computation time
MPM	Strength reduction	1.58	4.7 min/trial
FEM	Strength reduction	1.44	40 s
LEM	Spencer	1.44	1.6 s
	Morgenstern–Price	1.44	
	Simplified Bishop	1.44	
	Simplified Janbu	1.39	

Table 3.2: Computed factors of safety and computation times for the dry slope.

into 50 slices and 19,000 circular trial surfaces are examined. The FoS obtained from the Spencer, Morgenstern–Price, and simplified Bishop methods is nearly identical to the FEM value, whereas simplified Janbu yields a slightly lower value of 1.39.

Table 3.2 compares the three approaches in terms of the computed FoS and computation times. The FEM and LEM results are in close agreement, whereas the MPM estimate is approximately 10% higher. This difference is partly attributable to the distinct criteria used to identify failure. In FEM, the critical strength reduction factor is defined by the loss of numerical convergence, indicating that an equilibrium solution can no longer be obtained. In MPM, the calculation can continue beyond the onset of instability, and the FoS must therefore be inferred from the displacement response of the slope. Consequently, the estimated value depends on the response quantity and criterion used to distinguish stable and unstable behavior.

MPM is more computationally expensive than FEM and LEM when performing iterative stability analyses, mainly because of the small critical time step imposed by the explicit integration scheme. Whether this additional cost is justified depends on the purpose of the analysis. FEM and LEM are more efficient when the FoS is the only quantity of interest, whereas MPM is more suitable when both slope stability and the post-failure response are to be examined.

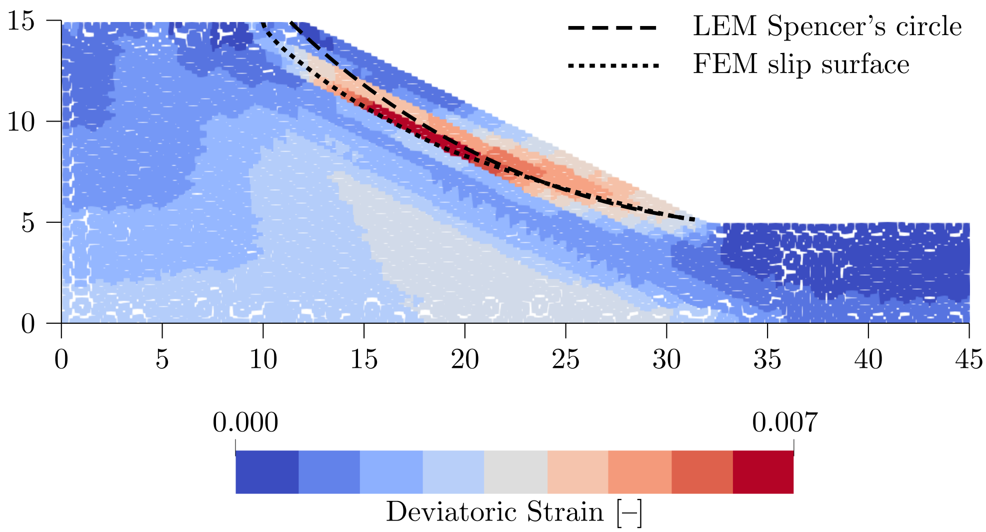

Figure 3.3: Deviatoric strain distribution for the dry slope at SRF = 1.44, compared with the FEM and Spencer slip surfaces.

Failure Mechanism

Figure 3.3 compares the deviatoric strain field at the onset of failure (SRF = 1.44) with the slip surfaces identified by FEM and LEM. A localized strain band extending from the slope toe to behind the crest is clearly observed, consistent with the shape of the reference slip surfaces shown in the same figure. In MPM and FEM, the failure mechanism develops naturally from the numerical calculation, whereas in Spencer's method the slip surface must be assumed a priori.

To examine the slope behavior beyond the onset of failure, the analyses are extended to reduction factors well above the critical value. Figure 3.4 compares the displacement contours obtained from MPM and FEM at four levels of strength reduction. In the FEM results (right column), mesh distortion develops progressively and becomes severe in Figure 3.4d, rendering the solution unreliable. The MPM results (left column) instead capture a more natural failure process. Knowing the extent of post-failure deformation and runout distance is valuable for landslide risk assessment and mitigation.

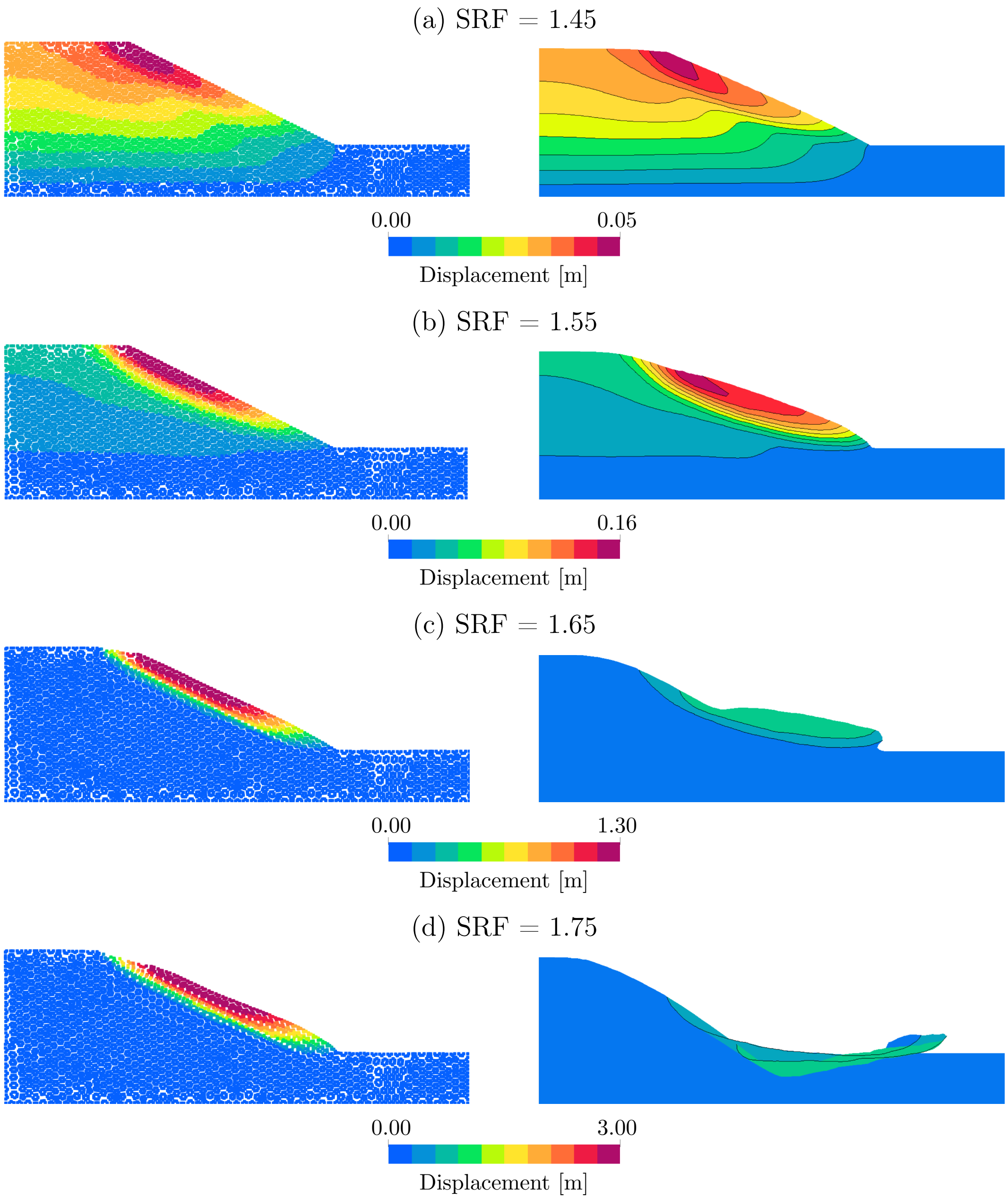

Figure 3.4: Displacement contours for the dry slope case obtained from MPM (left) and FEM (right).

Sensitivity to Numerical Parameters

The sensitivity of the results to the main numerical parameters is examined by varying the mesh size, the number of material points per element, and the damping factor, one at a time, while all other settings are kept at their reference values. For each variant, the complete displacement–SRF curve is recomputed and the FoS is re-estimated using the same bilinear construction applied in Figure 3.2. Table 3.3 reports the maximum displacement at selected reduction factors together with the estimated FoS, and Figure 3.5 shows the influence of the mesh on the response.

Among the parameters examined, the mesh size has the strongest influence on the results. Refining the mesh from h = 1.50 m to 0.50 m increases the displacement at SRF = 1.60 from 0.07 to 1.46 m, as a finer mesh resolves a narrower shear band and allows the failure mechanism to develop earlier. The FoS is much less affected and ranges from 1.51 on the finest mesh to 1.59 on the coarsest. Below the critical range, the mesh effect amounts to a few millimeters and is of little practical consequence, so the discretization matters mainly for the post-failure displacements. The number of material points has a minor influence. Three and six points per element produce nearly identical curves and the same FoS of 1.58, whereas a single point per element yields a lower FoS of 1.55. Reducing the damping factor from 0.05 to 0.01, or removing it entirely, increases the displacements by up to about 23% but changes the FoS by only 0.01. Additional checks showed that halving the Courant factor, or shortening the observation window from 5 to 1 s changes the response by less than 1%, and that the initialization damping and the temporary cohesion affect the displacements by a few millimeters without altering the failure mechanism.

In summary, the results are most sensitive to mesh size, whereas the number of material points, damping factor, and other numerical settings have only a minor influence. Mesh refinement primarily affects the displacement magnitudes, which vary by more than an order of magnitude across the cases considered. In contrast, the FoS remains within a relatively

	Maximum displacement [mm]					
	SRF = 1.40	1.45	1.50	1.55	1.60	**FoS**
$\alpha = 0.05$ (reference)	16.0	30.7	66.7	150.7	427.9	1.58
$\alpha = 0.01$	17.9	35.5	76.2	172.9	548.6	1.57
No damping	19.1	37.8	80.1	182.6	592.7	1.57
$h = 0.50$ m	19.4	48.5	120.4	449.1	1458.0	1.51
$h = 0.75$ m (reference)	16.0	30.7	66.7	150.7	427.9	1.58
$h = 1.00$ m	14.8	27.3	48.0	83.3	136.9	1.57
$h = 1.25$ m	12.5	20.8	32.4	48.7	72.0	1.56
$h = 1.50$ m	11.3	17.7	27.9	45.3	73.8	1.59
1 material point/element	15.3	28.8	62.3	142.2	1016.7	1.55
3 material points/element (reference)	16.0	30.7	66.7	150.7	427.9	1.58
6 material points/element	16.1	30.7	66.8	144.9	438.5	1.58

Table 3.3: Maximum displacements and estimated FoS for the sensitivity cases.

narrow range of 1.51 to 1.59 for all nine cases.

3.4.2 Case II: Unsaturated Slope with Steady-State Seepage

Model and Calculation Stages

Next, the stability of an unsaturated slope subjected to steady-state seepage is examined. The slope geometry is identical to that of the dry case (see Figure 3.1). Two sets of boundary conditions are required when using the coupled MPM formulation: one for the solid phase and one for the liquid phase. For the solid phase, full fixity is assigned to the bottom boundary, and fixity in the normal direction is assigned to the lateral boundaries. For the liquid phase, the boundary conditions are illustrated in Figure 3.6. A hydrostatic pressure corresponding to a groundwater level of 10 m is applied at the left boundary. The slope face and top surface are treated as potential seepage faces, and a total head of 5 m is prescribed on the lower horizontal ground surface. The same material properties are adopted here

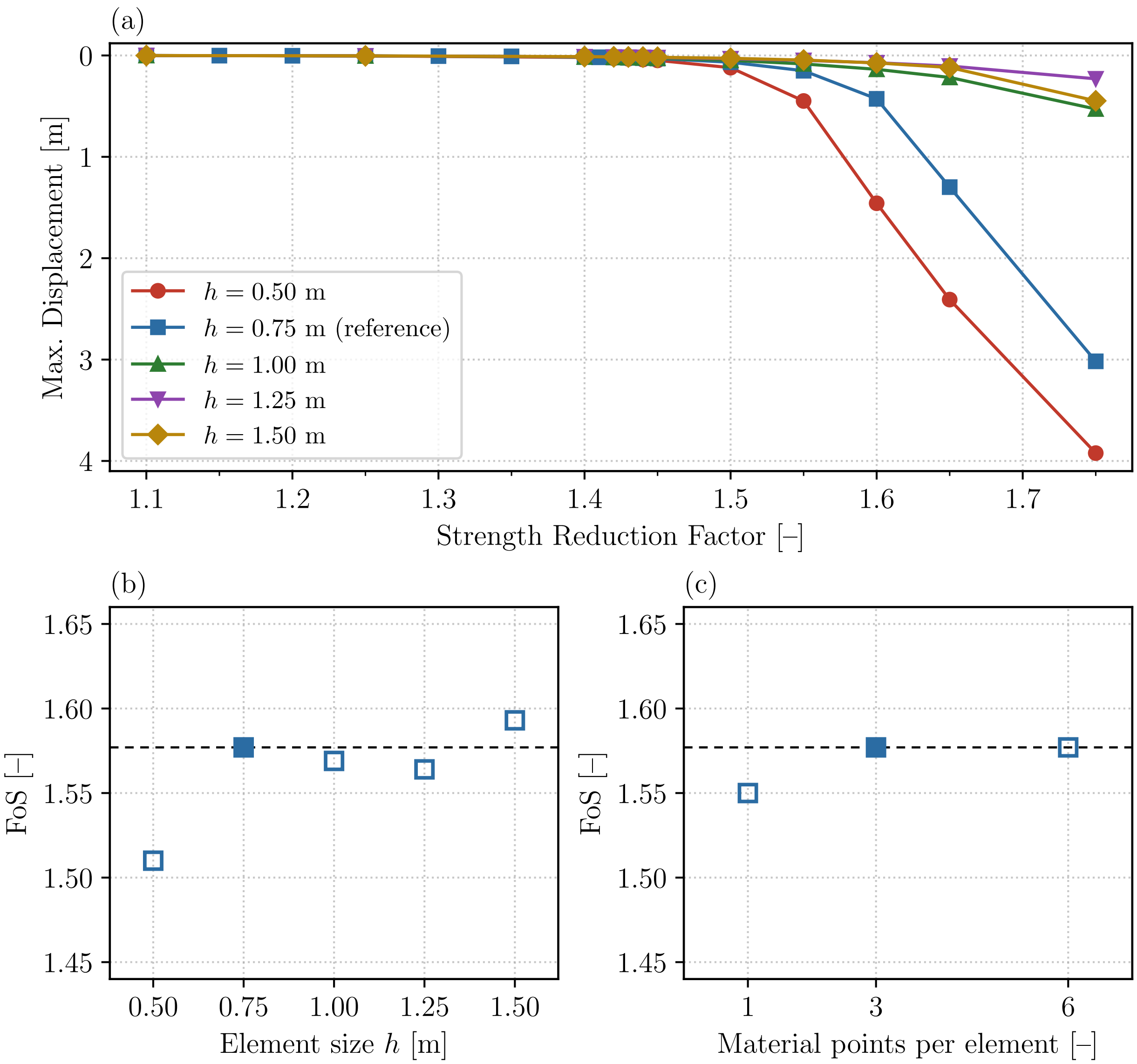

Figure 3.5: Numerical sensitivity of the dry slope. (a) Displacement response for the five mesh sizes. (b) FoS versus element size. (c) FoS versus number of material points per element. The dashed line marks the reference value.

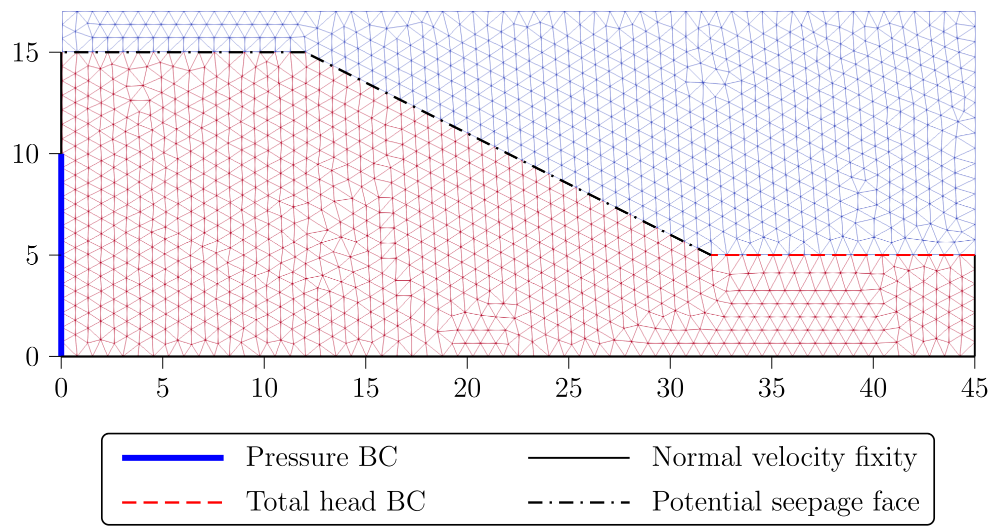

Figure 3.6: Prescribed boundary conditions for the liquid phase.

Hydraulic property	**Description**	**Value**
ρ_w	Density of water [kg/m^3]	1000
K_w	Bulk modulus of water [kPa]	80000
μ_d	Dynamic viscosity [kPa·s]	1×10^{-6}
κ_w	Intrinsic permeability [m^2]	6×10^{-11}
S_{min}	Minimum saturation [–]	0.15
S_{max}	Maximum saturation [–]	1.0
p_{ref}	SWRC parameter [kPa]	6.13
λ	SWRC parameter [–]	0.27

Table 3.4: Hydraulic properties of the unsaturated soil.

(Table 3.1). The computational mesh consists of 3,067 triangular elements, and the slope is represented by a total of 5,379 material points.

The hydraulic properties of the water phase are listed in Table 3.4. A relatively low bulk modulus is used to reduce the computational cost. The van Genuchten SWRC and the hydraulic conductivity are plotted in Figure 3.7. As stated in Section 3.2.2, the conductivity is constant and equal to the saturated value of 5.89×10^{-4} m/s, corresponding to the intrinsic permeability in Table 3.4. This simplification has limited influence in the present case

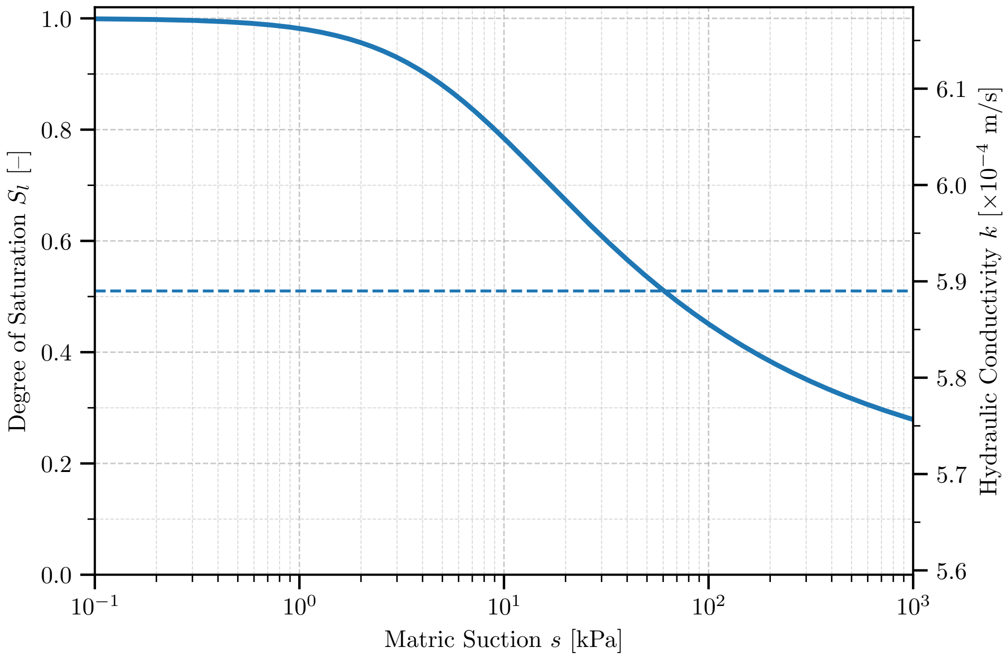

Figure 3.7: Soil–water retention curve (solid line) and the hydraulic conductivity used in the analyses (dashed line), which is constant and equal to the saturated value of 5.89×10^{-4} m/s.

because the seepage field is established as an initial condition and no rainfall or additional flow is imposed during the calculation.

Gravity loading is first applied to establish the initial stress state. The computational time of this stage is optimized by increasing the hydraulic conductivity by one order of magnitude and by applying mass scaling, both techniques commonly used in the literature (e.g., Girardi et al. (2021) and Yerro et al. (2015)). A high damping factor is avoided here because damping on the liquid phase significantly delays the dissipation of excess pore pressure and the approach to a quasi-static state (Ceccato et al., 2024). Volumetric locking in the low-order elements is mitigated by the strain-smoothing procedure of Ceccato and Simonini (2019).

Once quasi-static equilibrium is reached, the pore pressures and degree of saturation predicted by MPM are in very good agreement with those obtained from an FEM seepage analysis, as shown in Figure 3.8. Above the phreatic surface, suction is assumed to increase

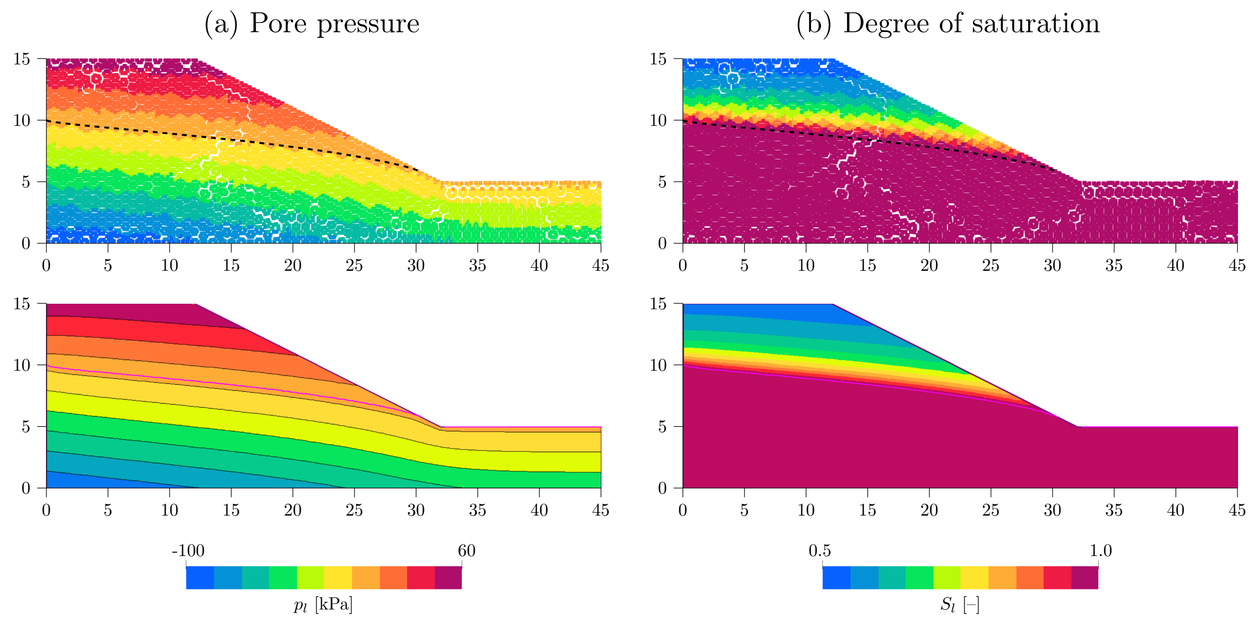

Figure 3.8: Comparison of (a) pore pressure distribution and (b) degree of saturation after stress initialization. The top row shows results from MPM and the bottom row from FEM. Pore pressure is shown positive in compression.

linearly with elevation, reaching a maximum value of 56 kPa. Based on the SWRC of Equation (3.13), the minimum degree of saturation is 0.52, consistent with the value observed near the slope crest. With the initial state established, the shear strength is then progressively reduced to evaluate the stability of the slope.

Displacement Response and Factor of Safety

The relationship between the maximum displacement and the strength reduction factor is presented in Figure 3.9. To identify the factor of safety accurately, smaller SRF increments are applied in the range where failure is expected. Using the same failure criterion adopted in the dry case, the factor of safety is found to be FoS = 1.28. Compared with the FEM critical value of 1.32, MPM predicts a slightly lower factor of safety, but the two results remain in close agreement.

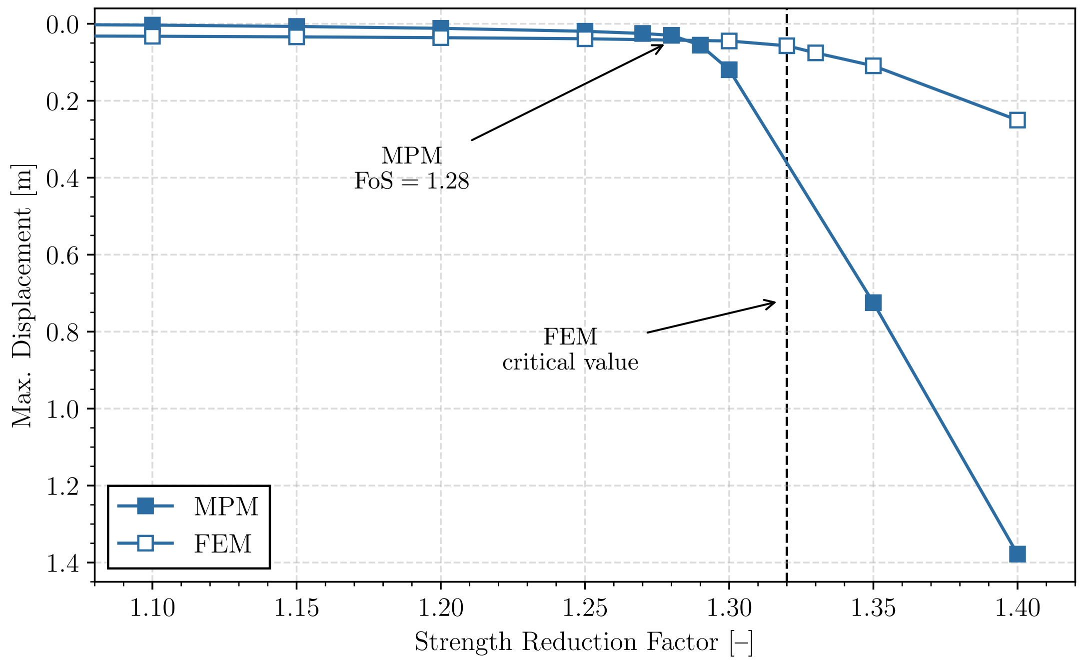

Figure 3.9: Maximum displacement versus strength reduction factor for the unsaturated slope.

Failure Mechanism

Figure 3.10 shows the deviatoric strain contours at the critical strength reduction factor, together with the slip surface predicted by FEM. The strain band is fully developed near the toe but remains diffuse toward the crest, indicating that failure initiates at the toe and propagates upslope along the FEM surface. Initiation at the toe is consistent with the seepage field. The phreatic surface exits near the toe, so the soil there is saturated and has lost its suction-induced strength, whereas the soil near the crest retains suction and yields last.

Sensitivity to Numerical Parameters

The main numerical parameters were varied to test the reliability of the estimated factor of safety. The time step, the number of material points per element, and the recording time have a negligible effect, whereas the mesh controls how sharply the slip surface forms. A

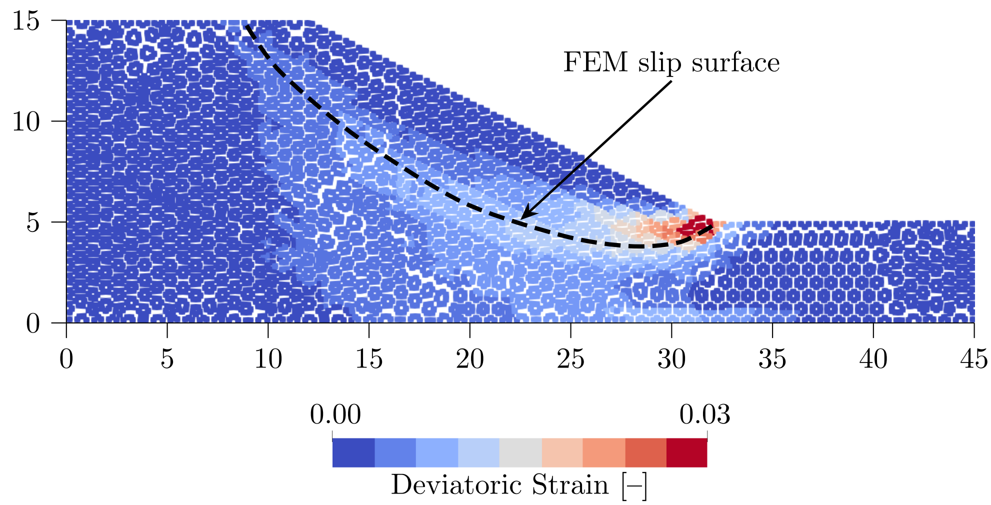

Figure 3.10: Deviatoric strain distribution for the unsaturated slope at FoS = 1.28, compared with the FEM slip surface.

finer discretization concentrates the shear band at the toe and slightly lowers the factor of safety, so on the finest mesh the toe has already failed at the strength reduction factor where the reference mesh is only beginning to move.

Local damping matters more here than in the dry case. Reducing it below the adopted value of $\alpha = 0.05$ amplifies the near-failure displacement several times over and triggers the toe failure slightly earlier. This stronger effect reflects the coupling between the moving soil and the pore water, which the dry problem lacks.

As anticipated in Section 3.2.2, replacing the constant conductivity with the suction-dependent Mualem model reduced the stable time step by a factor of more than fifty and made the calculation impractical.

3.5 Summary

This chapter examined MPM as a unified framework for slope stability analysis, in which the factor of safety, failure mechanism, and subsequent deformation are obtained within a single analysis. Two benchmark problems were considered: a dry slope and an unsaturated slope under steady-state seepage. For the dry slope, MPM gave a factor of safety of 1.58, approximately 10% higher than the value of 1.44 obtained using both FEM and limit equilibrium. This difference arises mainly from the different criteria used to identify failure. The slip surface predicted by MPM agreed well with those obtained using FEM and limit equilibrium. When the analysis was extended beyond failure, the FEM mesh experienced severe distortion, whereas MPM continued to simulate the downslope movement and runout of the failed soil mass.

The unsaturated slope was analyzed using a fully coupled hydromechanical MPM formulation. The SRF–displacement curve showed a clear transition from small displacement to rapid large deformation at an SRF of 1.28, which was taken as the MPM factor of safety. This value was slightly below the FEM result of 1.32, and the slip surfaces predicted by the two methods were again in close agreement. While further assessment using advanced soil constitutive models is necessary, the present study showed that MPM is a viable tool for slope stability problems and can incorporate complex features and behavior that conventional approaches, such as FEM, would struggle to represent.

Chapter 4

Vegetation Effects on Slope Failure and Runout

4.1 Introduction

The presence of roots enhances soil shear strength by mobilizing tensile resistance during shear deformation, thereby increasing the apparent cohesion of the rooted layer. Experimental studies have shown that this additional reinforcement is highly variable and depends on factors such as root biomass content, architecture, drainage conditions, and stress path (Alam et al., 2022; Jiang et al., 2022; C.-B. Zhang et al., 2010; Zou et al., 2024). For most natural vegetation, root systems tend to be more concentrated near the ground surface (Ni et al., 2018). As a result, mechanical reinforcement is most effective against shallow failures and surface erosion but contributes only marginally to deep-seated failures. In addition to mechanical reinforcement, roots modify the soil's hydraulic properties, namely the soil–water retention curve (SWRC) and the hydraulic conductivity function (HCF). Predictive models for the SWRC and HCF that account for root-induced changes in the pore space have been proposed by Ng, Ni, et al. (2016) and H. Wang et al. (2025), respectively. Vegetation can also improve slope stability through evapotranspiration, which extracts water from the soil and increases matric suction. For instance, Ng, Kamchoom, and Leung (2016) reported in their centrifuge tests that ignoring evapotranspiration-induced suction may underestimate the post-rainfall factor of safety by up to 50%. The influence of evapotranspiration, however, acts mainly through the antecedent suction built up over longer periods. During short rainfall events, mechanical root reinforcement plays a more direct role in the initiation and failure of shallow landslides (Sidle & Bogaard, 2016).

Various approaches in the literature quantify the contribution of plant roots to soil shear strength. The earliest and most widely used is the Wu–Waldron model (Waldron, 1977; Wu et al., 1979), in which an apparent root cohesion c_r is added to the Mohr–Coulomb shear strength criterion. The model assumes that all roots crossing the shear plane fail simultaneously in tension, thereby overestimating c_r. Fiber-bundle models (Pollen & Simon, 2005; Schwarz et al., 2010; Thomas & Pollen-Bankhead, 2010) were later developed to account for the progressive breakage of roots and the redistribution of load among the intact ones. In both approaches, root reinforcement is captured as an increase in the cohesion intercept, which modifies only the failure strength and does not fully describe the constitutive behavior of rooted soil. More recently, Świtała et al. (2018) proposed a rooted-soil constitutive model that addresses this limitation by extending the modified Cam-clay framework of Tamagnini (2004), introducing the root biomass as an additional hardening variable that drives the increase in preconsolidation pressure. This formulation captures the progressive mobilization of root reinforcement with shear deformation, together with the associated changes in yield, hardening, and dilatancy. Applications of this model to slope stability problems remain limited to a few studies (Kang et al., 2026; Świtała & Wu, 2018; Świtała, 2020), which reproduce the main trends observed in rainfall-induced failures of rooted slopes.

Despite the recognized advantages of MPM for landslide modeling, vegetation effects remain rarely investigated in MPM analyses of slope failure. To the author's knowledge, Cuomo et al. (2024) is the only such study to account for root reinforcement, and it does so by adding a Wu–Waldron apparent cohesion to the Mohr–Coulomb criterion. The simulations therein indicate that fine, long-rooted grass can mitigate the impact of a debris avalanche on engineered slopes, but rainfall infiltration and failure initiation in the rooted slope are not addressed. Further MPM analyses incorporating advanced constitutive models for rooted soils are therefore needed to capture the influence of vegetation on rainfall-induced failure initiation and the subsequent deformation.

This chapter implements the constitutive model of Świtała et al. (2018) to characterize the role of vegetation in rainfall-induced landslides using a fully coupled hydromechanical MPM formulation. The model is first verified against the numerical triaxial results of Świtała et al. (2019) and then validated against the drained triaxial dataset of Alam et al. (2022) on rooted loess. The vegetated and bare slope cases are then compared to isolate the effect of root reinforcement, and the analysis examines how the root content influences failure initiation, the failure mechanism, and the post-failure runout. Finally, the formulation is validated against a documented centrifuge slope test.

4.2 Numerical Framework for Rooted Soil

The simulations reported in this chapter are performed using the open-source MPM code Anura3D, which implements the two-phase single-point formulation for unsaturated soils developed by Ceccato et al. (2021). The rooted-soil model of Świtała et al. (2018) is implemented as a user-material (UMAT) subroutine and integrated into Anura3D as a native soil model. The governing equations of the MPM formulation were presented in Chapter 2, and the unsaturated extension used here was summarized in Section 3.2; only the constitutive model for rooted soil, which is the central contribution of this chapter, is developed in full below.

4.2.1 Constitutive Model for Rooted Soil

The mechanical behavior of rooted soil is described using the multiple-hardening Cam-clay model of Świtała et al. (2018). Building on the unsaturated Cam-clay framework of Tamagnini (2004), the model treats the mobilization of root reinforcement as an additional hardening mechanism. A key feature of the model is the macroscopic representation of the soil-root composite as a single homogenized continuum with uniform effective properties. For finely and densely rooted soils this treatment is appropriate, since explicitly resolving individual roots would be extremely difficult, if not impossible, and would be impractical at the scale of a slope (Kang et al., 2026; Świtała et al., 2019).

Yield Surface and Flow Rule

As in the classical modified Cam-clay model, the yield surface is an ellipse in the p'–q plane defined by

$$f(p', q, p'_c) = \frac{q^2}{M_r^2} - p'\,(p'_c - p') = 0, \tag{4.1}$$

where $p' = -\frac{1}{3}\mathrm{tr}(\boldsymbol{\sigma}')$ and $q = \sqrt{\frac{3}{2}\,\boldsymbol{s} : \boldsymbol{s}}$ are the mean effective and deviatoric stresses, respectively, and $\boldsymbol{s} = \boldsymbol{\sigma}' - \frac{1}{3}\mathrm{tr}(\boldsymbol{\sigma}')\,\mathbf{I}$ is the deviatoric part of the effective stress tensor. The preconsolidation pressure p'_c controls the size of the yield surface, and M_r is the slope of the critical-state line. An associated flow rule is adopted, so that the plastic potential coincides with the yield function, $g \equiv f$, and the plastic strain increment is

$$\mathrm{d}\boldsymbol{\epsilon}^p = \mathrm{d}\lambda^p \frac{\partial f}{\partial \boldsymbol{\sigma}'}, \tag{4.2}$$

where $\mathrm{d}\lambda^p$ is the plastic multiplier. The derivatives of the yield function with respect to the stress invariants and the preconsolidation pressure, which are required by the integration scheme, are

$$\frac{\partial f}{\partial p'} = 2p' - p'_c, \qquad \frac{\partial f}{\partial q} = \frac{2q}{M_r^2}, \qquad \frac{\partial f}{\partial p'_c} = -p'. \tag{4.3}$$

In the original rooted-soil model, M_r was treated as a fixed material constant. Here, following the direct-shear observations of Kang et al. (2026) on loess reinforced with herbaceous roots, which showed that the shear-strength parameters increase with the root biomass content, the critical-state slope is instead assumed to vary linearly with the initial root mass fraction m_r^{ini},

$$M_r = M_0 + R_a \, m_r^{\text{ini}}, \tag{4.4}$$

where M_0 is the critical-state slope of the bare soil and R_a is a dimensionless root parameter that governs the increase of the critical-state slope with root content.

Root Activation Strain

To account for the progressive mobilization of root reinforcement, the model introduces an activation strain ε_r, whose rate is defined as the sum of the volumetric and deviatoric strain rates,

$$\dot{\varepsilon}_r = \dot{\varepsilon}_v + \dot{\varepsilon}_q. \tag{4.5}$$

The activation strain accumulates with continued deformation until it reaches a peak value $\varepsilon_r^{\text{peak}}$. Beyond this peak the roots begin to break, and the shear strength gradually converges to the residual state. This dependence on the current strain level reflects the experimental observation that root reinforcement is not mobilized instantaneously but develops progressively as the soil-root composite is sheared (Schwarz et al., 2010; Świtała et al., 2019).

Hardening Law

The initial value of the preconsolidation pressure, p'_{cn}, depends on both the initial suction and the initial root content and is given by

$$p'_{cn} = p'_{c0} \, \exp\left[\, b\,(1 - S_{\text{ini}}) + R_p \, m_r^{\text{ini}} \,\right], \tag{4.6}$$

where p'_{c0} is the saturated preconsolidation pressure of the non-vegetated soil, S_{ini} is the initial degree of saturation, and m_r^{ini} is the initial root mass fraction expressed as a percentage. The parameter b controls the hardening due to partial saturation, and R_p is a root characteristic parameter that depends on the plant type and is calibrated from direct-shear or triaxial tests.

The subsequent evolution of the preconsolidation pressure is governed by a multiple-hardening law that superposes three mechanisms (mechanical, hydraulic, and root reinforcement) so that

$$\dot{p}'_c = \dot{p}'_{c,\mathrm{sat}} + \dot{p}'_{c,\mathrm{unsat}} + \dot{p}'_{c,\mathrm{root}}. \tag{4.7}$$

The first term recovers the classical Cam-clay hardening law,

$$\dot{p}'_{c,\mathrm{sat}} = \frac{1+e}{\lambda - \kappa}\, p'_c\, \dot{\varepsilon}_v^p, \tag{4.8}$$

where $\dot{\varepsilon}_v^p$ is the plastic volumetric strain rate, e is the current void ratio, and λ and κ are the slopes of the normal-compression and swelling lines in the e–$\ln p'$ plane. The second term, after Tamagnini (2004), is the hardening produced by changes in partial saturation,

$$\dot{p}'_{c,\mathrm{unsat}} = -b\, p'_c\, \dot{S}_L, \tag{4.9}$$

where $\dot{S}_L$ is the rate of change of saturation. The third term is the progressive hardening due to root reinforcement, which mobilizes as the activation strain accumulates,

$$\dot{p}'_{c,\mathrm{root}} = R_p\, p'_c\, e\, \dot{\varepsilon}_r\, m_r^{\mathrm{ini}}. \tag{4.10}$$

The evolution of the yield surface can be visualized in the extended p'–q–ψ/ε_r space shown in Figure 4.1. Ellipse A represents the initial yield surface. The accumulation of plastic volumetric strain increases the preconsolidation pressure causing an expansion of ellipse A to B. Suction and root activation work as a separate mechanism to provide additional hardening through Equations (4.9) and (4.10), extending the yield surface to C; its projection onto the p'–q plane forms ellipse D. Conversely, wetting or root rupture reduces the corresponding

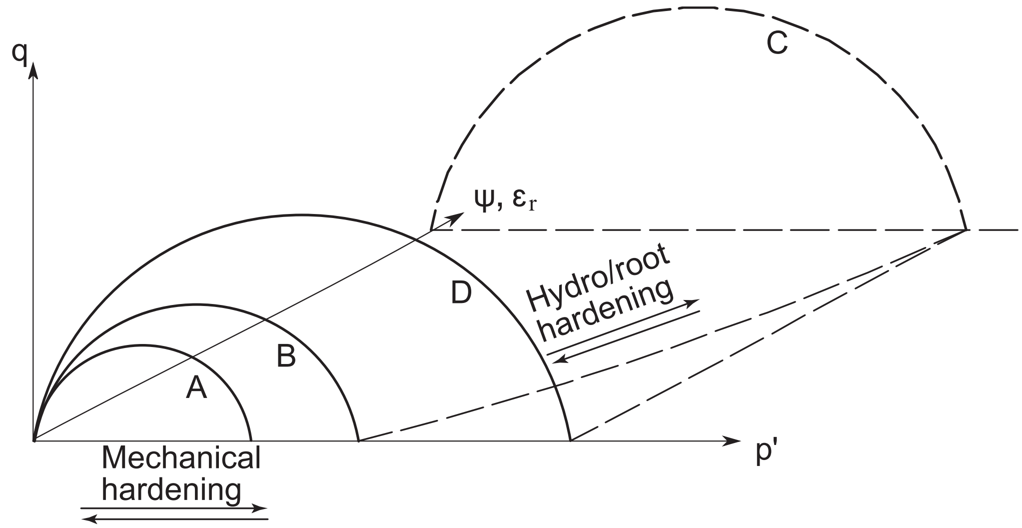

Figure 4.1: Evolution of the yield surface under the three superposed hardening mechanisms, represented in the extended p'–q–ψ/ε_r stress space (from Świtała et al. (2019)).

hardening contribution, causing the yield surface to contract and the material to soften.

Numerical Integration

The constitutive equations are integrated implicitly through the return-mapping algorithm of Borja and Lee (1990). At the beginning of each step, the trial state is computed by freezing the plastic flow while allowing the preconsolidation pressure to evolve with the known increments of saturation and root activation strain,

$$\begin{cases} \boldsymbol{\sigma}^{\mathrm{tr}}_{n+1} = \boldsymbol{\sigma}_n + \mathbf{D}^e \Delta\boldsymbol{\epsilon}_{n+1}, \\ p'^{\,\mathrm{tr}}_{c,n+1} = p'_{c,n} \, \exp\!\left(-b\,\Delta S_{L,n+1} + R_p\, e\, \Delta\varepsilon_{r,n+1}\, m_r^{\mathrm{ini}}\right), \\ f^{\mathrm{tr}}_{n+1} = f\left(p'^{\,\mathrm{tr}}_{n+1},\, q^{\mathrm{tr}}_{n+1},\, p'^{\,\mathrm{tr}}_{c,n+1}\right), \end{cases} \tag{4.11}$$

where $\mathbf{D}^e$ is the elastic stiffness tensor. A distinct feature of this model is that the yield surface is allowed to expand even during elastic loading, which is essential for capturing the hardening induced by desaturation and root mobilization. The trial stress invariants follow as $p'^{\,\mathrm{tr}}_{n+1} = -\frac{1}{3}\mathrm{tr}(\boldsymbol{\sigma}^{\mathrm{tr}}_{n+1})$ and $q^{\mathrm{tr}}_{n+1} = \sqrt{\frac{3}{2}}\,\|\boldsymbol{\xi}^{\mathrm{tr}}_{n+1}\|$, with $\boldsymbol{\xi}^{\mathrm{tr}}_{n+1} = \boldsymbol{\sigma}^{\mathrm{tr}}_{n+1} - \frac{1}{3}\mathrm{tr}(\boldsymbol{\sigma}^{\mathrm{tr}}_{n+1})\mathbf{I}$.

If $f^{\mathrm{tr}}_{n+1} < 0$, the trial state lies inside the yield surface, the step is elastic, and all variables are updated with their trial values. Otherwise, a plastic corrector returns the stress to the yield surface. The corrected stress increment is

$$\mathrm{d}\boldsymbol{\sigma}_{n+1} = \mathrm{d}\boldsymbol{\sigma}^{\mathrm{tr}}_{n+1} - \mathbf{D}^e \, \mathrm{d}\lambda^p \frac{\partial f}{\partial \boldsymbol{\sigma}'}, \tag{4.12}$$

which, projected onto the invariant axes and combined with the hardening law equation (4.7), yields the updated invariants (see Borja and Lee (1990) for a detailed derivation)

$$p'_{n+1} = p'^{\,\mathrm{tr}}_{n+1} - K \, \Delta\lambda^p \left(2p'_{n+1} - p'_{c,n+1}\right), \tag{4.13}$$

$$q_{n+1} = \frac{q^{\mathrm{tr}}_{n+1}}{1 + 6G \, \Delta\lambda^p / M_r^2}, \tag{4.14}$$

$$p'_{c,n+1} = p'^{\,\mathrm{tr}}_{c,n+1} \, \exp\left(\frac{1+e}{\lambda - \kappa} \, \Delta\varepsilon^p_v\right), \tag{4.15}$$

where K and G are the elastic bulk and shear moduli, and $\Delta\varepsilon^p_v = \Delta\lambda^p \left(2p'_{n+1} - p'_{c,n+1}\right)$ is the plastic volumetric strain increment obtained from the associated flow rule. The four unknowns p'_{n+1}, q_{n+1}, $p'_{c,n+1}$, and $\Delta\lambda^p$ are obtained by enforcing the consistency condition $f_{n+1} = 0$ together with equations (4.13) to (4.15), and the resulting system of nonlinear equations is solved with the Newton-Raphson method. After convergence, the consistent tangent modulus is computed and returned by the UMAT subroutine.

4.3 Verification and Validation of the Constitutive Model

The UMAT implementation is first verified against the numerical triaxial results reported by Świtała et al. (2019). Single-element simulations are performed to isolate the constitutive response from MPM discretization effects. The material parameters and hydraulic properties are taken from the referenced paper. The initial root mass fraction is set to 10% in all simulations, while the root parameter R_p is varied from 0 (bare soil) to 10 (strongly reinforced). The resulting q–ε_a curves, shown in Figure 4.2, match the numerical results

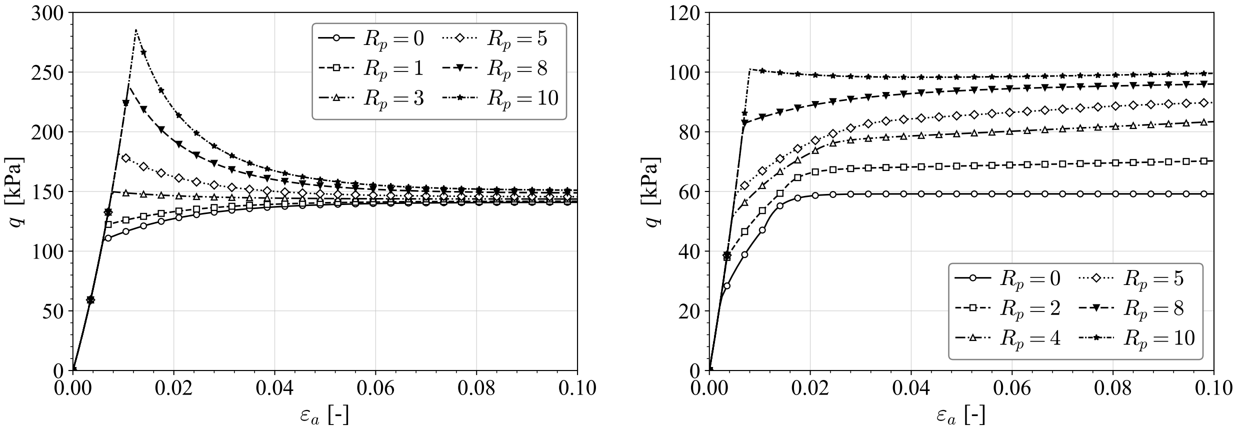

(a) Drained

(b) Undrained

Figure 4.2: Evolution of deviatoric stress with axial strain for different values of R_p, compared with the results of Świtała et al. (2019).

in the original paper. In Equation (4.10), the initial root mass fraction, m_r^{ini}, is omitted in producing the results of Figure 4.2, as it was introduced in a later revision of the constitutive model (Świtała, 2020).

Next, the predictive capability of the model is assessed against one of the few experimental datasets on rooted soil. Previous validations mainly considered grass and herbaceous roots. Here, the model is further validated against the drained triaxial tests of Alam et al. (2022) on saturated loess reinforced with woody roots. The samples were collected from the Longchi forest in Sichuan, China, and reconstituted into cylinders 100 mm high and 50 mm in diameter, each containing randomly oriented roots of *Cryptomeria japonica* (Japanese cedar) up to 5 mm thick. Different root biomass contents were examined, of which 0.63, 1.25, and 2.5 g are used in the simulations. Each specimen was saturated, isotropically consolidated, and then sheared at 0.01 mm/min under fully drained conditions.

Material parameters used for validation are summarized in Table 4.1. For bare soil, $M_0 = 1.42$ was obtained from the measured drained failure envelope ($\varphi' = 35.0°$). Initial preconsolidation pressure $p'_{c0} = 125$ kPa was taken from the p'-intercept of the yield envelope, while $e_0 = 0.86$ was calculated from the dry density using $G_s = 2.70$. Initial root mass

Parameter	Description	Value
ρ_d	Soil dry density [kg/m^3]	1453
ν	Poisson's ratio [–]	0.30
e_0	Initial void ratio [–]	0.86
p'_{c0}	Initial preconsolidation pressure [kPa]	125
λ	Plastic compressibility [–]	0.089†
κ	Elastic compressibility [–]	0.022†
M_0	Slope of the critical-state line [–]	1.42
b	Parameter for partial saturation [–]	0.00
S_{ini}	Initial degree of saturation [–]	1.00
R_p	Root characteristic parameter [–]	0.28†
R_a	Root parameter [–]	0.18†
m_r^{ini}	Initial root content [%]	0.22 / 0.44 / 0.88

Table 4.1: Material parameters used for validation of the soil–root constitutive model.
† Calibrated soil parameter.

fraction was calculated as the ratio of root mass to dry-soil mass. Accordingly, biomass contents of 0.63, 1.25, and 2.5 g correspond to $m_r^{\text{ini}} = 0.22$, 0.44, and 0.88%, respectively. Parameters not measured directly in the tests were specified separately. The compression parameters λ and κ were calibrated against the bare-soil response, whereas R_p and R_a were calibrated against the reinforced-soil curves. Poisson's ratio was taken as $\nu = 0.30$. Since all specimens were saturated before shearing, $S_{\text{ini}} = 1$ and partial-saturation hardening was inactive ($b = 0$).

Figure 4.3 compares the computed stress–strain response with reference curves reconstructed from the peak strengths and trends reported by Alam et al. (2022). For bare soil, the simulation captures nonlinear hardening and predicts the peak deviator stress within about 6% at all three confining pressures. The predicted volumetric response is contractive, consistent with the compression measured in the tests. However, the gradual post-peak reduction in deviator stress is not reproduced. In modified Cam-clay, post-peak softening

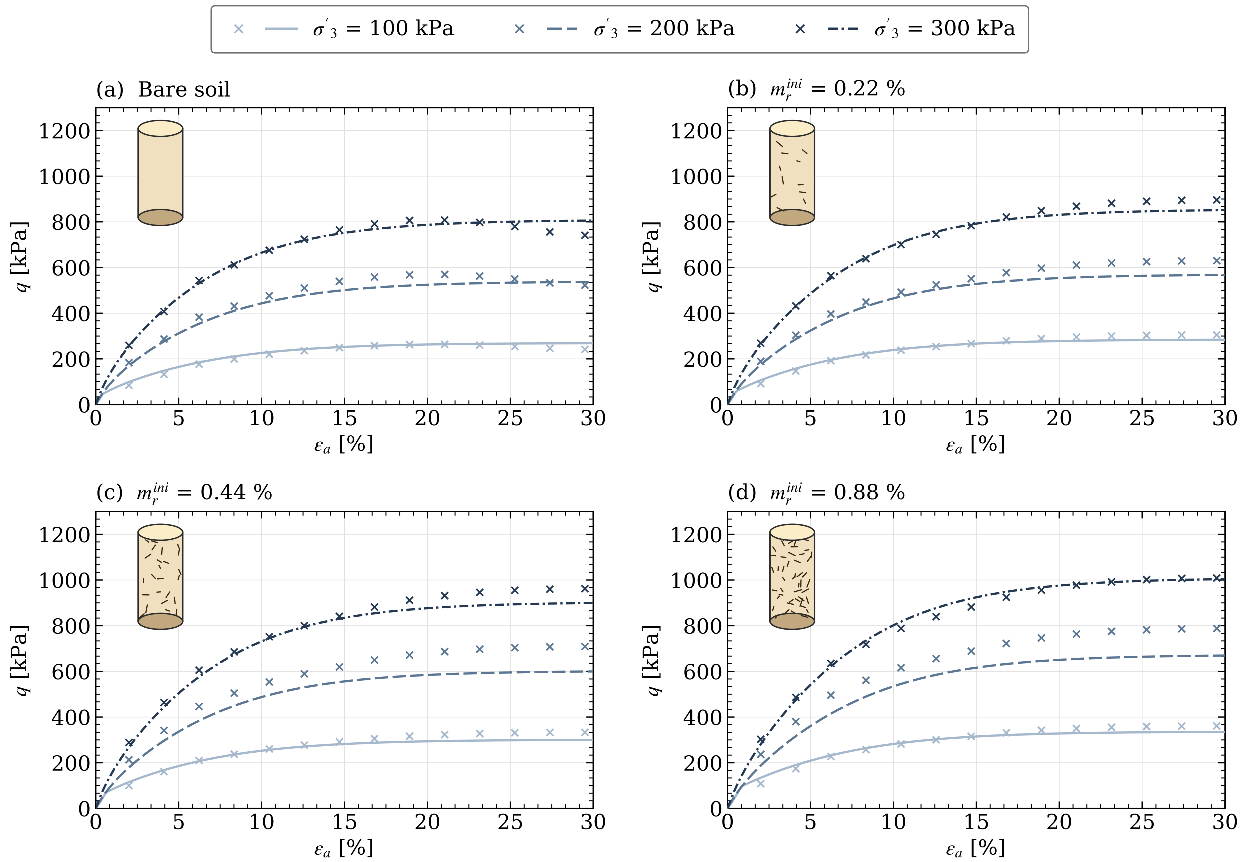

Figure 4.3: Comparison between predicted and measured triaxial test results of loess soil with various biomass content at cell pressures of 100, 200 and 300 kPa.

develops only on the dry side of the critical-state line and is accompanied by plastic dilation. With $p'_{c0} = 125$ kPa, the reconstituted loess remains lightly overconsolidated and contractive. Consequently, the formulation cannot reproduce the measured combination of volumetric contraction and strain softening.

The rooted specimens become stronger with increasing root content, and in all cases the deviator stress increases monotonically with axial strain. Only the bare soil specimens reached peak strength at approximately 20% axial strain and subsequently softened toward a residual state. The rooted specimens, however, continued to gain strength throughout shearing and had not reached their peak strength by the end of the tests. The model reproduces the measured strengths at all three confining pressures, with the largest discrepancy, approximately 10–15%, occurring at 200 kPa. The close agreement at low strains and stress levels supports the use of the model for shallow landslide analysis, where failure of the soil–root mass typically occurs under low confining stresses.

4.4 Stability Analysis of Vegetated Slopes under Rainfall

The implemented soil–root model is now applied to an idealized slope subjected to rainfall infiltration, in order to isolate the effect of vegetation on the initiation and the post-failure development of a shallow landslide. The soil and root parameters follow the herbaceous-root loess dataset of Kang et al. (2026). The saturated hydraulic conductivity, however, is set to a higher value to accelerate the failure and reduce the computational time. Four cases are considered: a bare slope and three vegetated slopes with initial root mass fractions of 0.51, 0.94, and 1.29%. The comparison addresses the time to failure, the accumulated displacement, and the failure mechanism.

4.4.1 Model Setup

The geometry of the slope model is shown in Figure 4.4. The slope is 4 m high, with a face inclined at 45° and a toe at an elevation of 1 m. The crest and the ground beyond the toe extend 3 m and 4 m from the face, placing the lateral boundaries far enough not to affect the results. A steep inclination is chosen so that the slope is initially close to failure and is held stable by the suction. Rainfall infiltration then triggers failure quickly through the loss of suction. A root layer covering the top 0.5 m of the surface represents herbaceous vegetation. This thickness falls within the typical rooting depth of such species, which form the dense near-surface network assumed in the homogenized treatment of Section 4.2.1 (Kang et al., 2026).

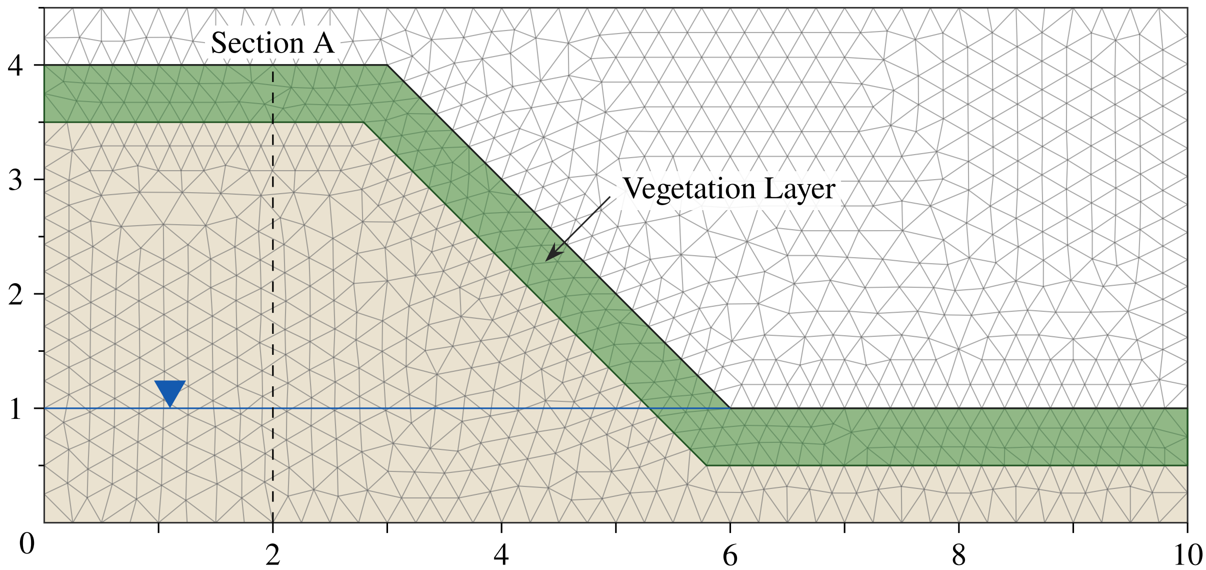

Figure 4.4: Geometry, computational mesh, rooted surface layer, and initial water-table position. Section A marks the vertical profile examined in Figure 4.6.

An unstructured mesh of 1,798 three-node triangular elements and 959 nodes discretizes the model and is locally refined across the rooted zone. Initially, 1,003 elements are active, and each carries three material points, giving 3,009 in total. Out of these, 990 material points are located in the rooted layer for the vegetated slope cases.

Boundary conditions consist of full fixity at the base and normal fixity at the lateral boundaries. The water table sits initially at $y = 1$ m, with a hydrostatic pressure profile below it. Suction is assumed linear above the water table. Self-weight equilibrium is established first. The overconsolidation ratio R_0 given in Table 4.2 is used to initialize the saturated preconsolidation pressure as $p'_{c0} = R_0 p'_{\text{ini}}$, where p'_{ini} is the mean effective stress obtained. The effects of suction and roots subsequently increase the initial preconsolidation pressure according to Equation (4.6).

Mechanical parameters of the bare soil and the soil–root composite are listed in Table 4.2. All four cases share one parameter set and differ only in the initial root mass fraction.

Hydraulic behavior follows the van Genuchten retention curve of Equation (3.13) and the

Parameter	Description	Value
ρ_s	Density of solid grains [kg/m^3]	2710
ν	Poisson's ratio [–]	0.35
e_0	Initial void ratio [–]	0.6
R_0	Preconsolidation ratio [–]	3.0
λ	Plastic compressibility [–]	0.155
κ	Elastic compressibility [–]	0.04
M_0	Slope of the critical-state line [–]	0.827
b	Parameter for partial saturation [–]	10
R_p	Root characteristic parameter [–]	0.4
R_a	Root parameter [–]	0.18
m_r^{ini}	Initial root content [%]	0 / 0.51 / 0.94 / 1.29

Table 4.2: Mechanical and root parameters of the bare soil and the soil–root composite (Kang et al., 2026).

Mualem conductivity,

$$k = k_s \sqrt{S_w} \left[1 - \left(1 - S_w^{1/\lambda_{VG}} \right)^{\lambda_{VG}} \right]^2 \tag{4.16}$$

where $p_{ref} = 15.63$ kPa and $\lambda_{VG} = 0.288$. The subscript λ_{VG} distinguishes the van Genuchten parameter from the Cam-clay compression index λ. Retention parameters are fitted to measured data of J. Wang et al. (2015) for the same Malan loess (Kang et al., 2026). Both functions are shown in Figure 4.5, and additional hydraulic parameters are listed in Table 4.3. A residual saturation of zero is adopted. However, the results are insensitive to this value because computed suctions in the slope remain below about 30 kPa, where $S_w \geq 0.7$.

For simplicity, bare soil and rooted layer share one retention curve, but a modestly higher saturated conductivity is assigned to the rooted layer. Young, actively growing roots of herbaceous species tend to raise near-surface permeability by opening preferential flow paths, unlike roots of woody plants (Kang et al., 2026; Ni et al., 2018). In the slope model, saturated conductivity is raised by about three orders of magnitude, to 7.62×10^{-4} m/s in bare soil and 9.81×10^{-4} m/s in the rooted layer, so that the wetting front reaches the failure zone within a computationally feasible time. Reported times therefore follow an exaggerated numerical scale rather than field rainfall durations. Rainfall is prescribed as a flux of $q_r = 6.0 \times 10^{-4}$ m/s, far larger than any natural intensity and scaled together with the conductivity. This flux stays below the infiltration capacity set by the saturated conductivity, so all water infiltrates and no ponding occurs. Such a condition is necessary because the two-phase single-point formulation cannot simulate free water above the surface. Interception by vegetation, surface runoff, and evapotranspiration are not accounted for in the present analyses. If rainfall intensity significantly exceeded the infiltration capacity of the soil, the neglect of runoff would lead to an overestimation of pore pressures near the surface.

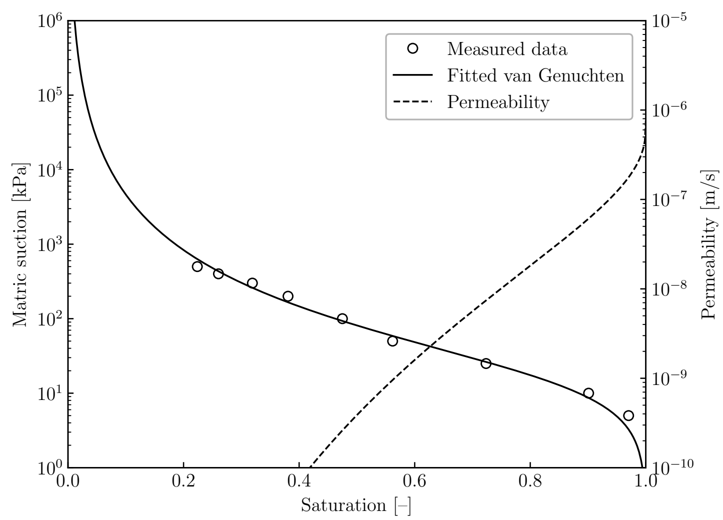

Figure 4.5: Measured soil-water retention data, fitted van Genuchten curve, and the true hydraulic conductivity function calibrated for the loess, with $k_s = 7.62 \times 10^{-7}$ m/s. A higher conductivity value was used in the numerical simulation (see Table 4.3).

Rainfall is applied as an inward flux q_r prescribed over the whole ground surface and maintained throughout the 560-s simulation. A mass-scaling factor of 80 increases the critical time step, and local damping is set to 0.75 during self-weight equilibrium and 0.05 during rainfall.

Hydraulic property	**Description**	**Value**
ρ_w	Density of water [kg/m^3]	1000
K_w	Bulk modulus of water [kPa]	5000
μ_d	Dynamic viscosity [kPa·s]	1×10^{-6}
S_{min}	Minimum saturation [–]	0
S_{max}	Maximum saturation [–]	1.0
p_{ref}	SWRC parameter [kPa]	15.63
λ_{VG}	SWRC parameter [–]	0.288
k_s	Saturated conductivity [m/s]	7.62×10^{-4}

Table 4.3: Hydraulic parameters for the bare soil.

A numerical difficulty arises as the wetting front approaches full saturation $S_r \approx 0.999 \to 1$. At this state, the retention term $\partial S_w/\partial p_w$ in the pore-pressure update of Equation (3.4) vanishes, and the storage coefficient reduces to the fluid compressibility term, which scales with $1/K_w$. Each pressure increment then becomes proportional to K_w, and at the physical modulus small errors in volumetric strain rate are amplified into severe pore-pressure oscillations that ultimately destabilize the solution. Stable calculations were obtained only after lowering K_w to 5,000 kPa, far below the physical value. Both the mass scaling and the reduced K_w affect the transient response, so results are interpreted through differences between identically configured cases rather than as calibrated predictions of actual field behavior.

4.4.2 Failure Initiation and Runout

Failure is triggered by rainfall infiltration, which shrinks the yield surface of the wetted soil. Figure 4.6 presents vertical profiles of the preconsolidation pressure p'_c during rainfall, extracted along section A marked in Figure 4.4, for the bare slope and the highest root content. Before rainfall, p'_c increases linearly with depth below the water table, while suction strengthens the unsaturated zone above it, most strongly near the crest. Roots enlarge this initial value further within the rooted layer, so the vegetated slope starts from a larger yield surface than the bare one. As infiltration proceeds, suction is quickly lost at the surface, and the loss follows the wetting front downward. Wherever suction vanishes, p_c' collapses toward its saturated value, and much of the upper profile falls to about 50 kPa. Roots do not slow this hydraulic softening. Their contribution is the larger initial surface, which leaves more strength in place once suction disappears. Late profiles are read qualitatively, since large deformation moves material across elevations.

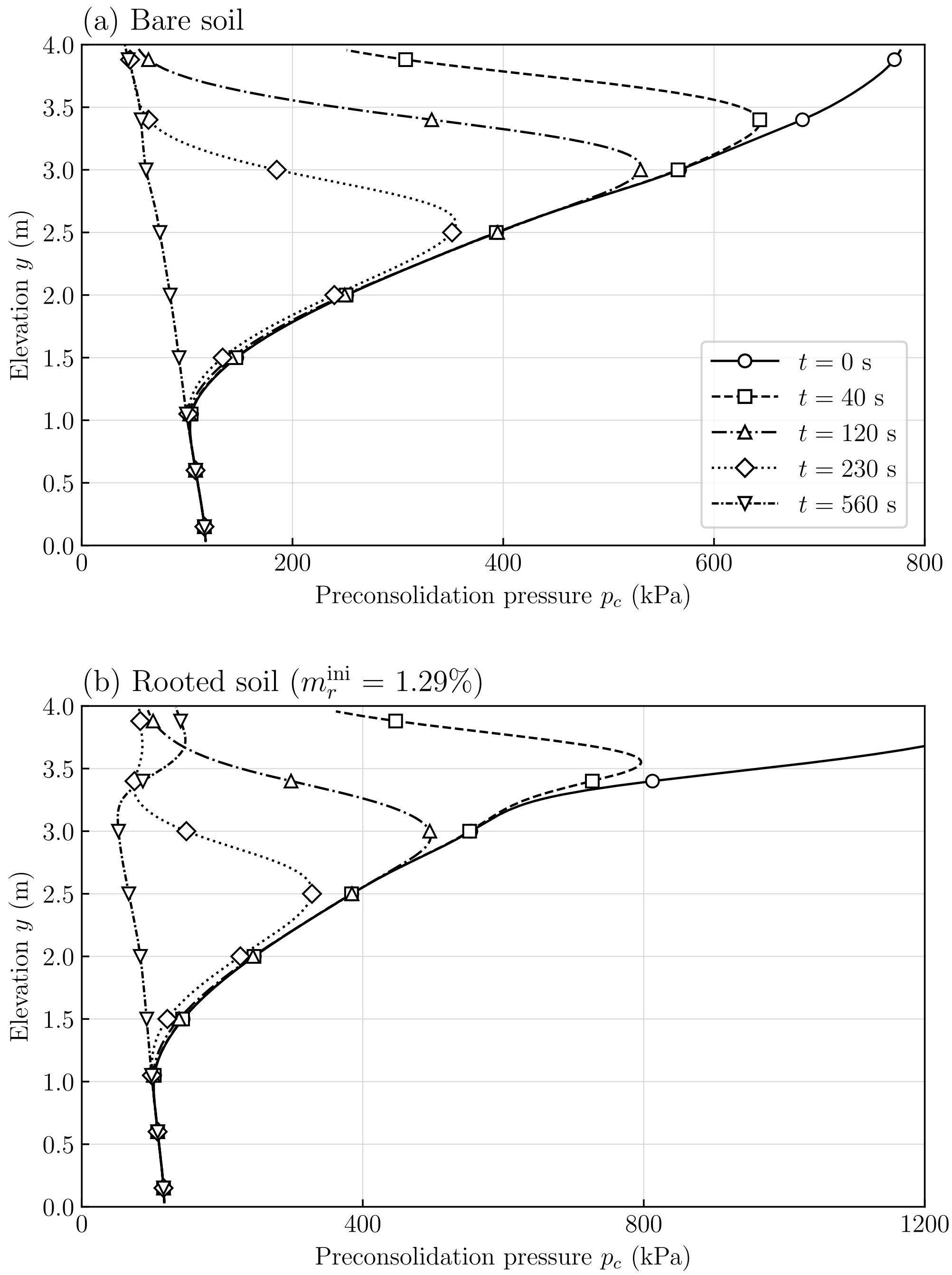

Figure 4.6: Preconsolidation-pressure profiles at the start of rainfall and at 40, 120, 230, and 560 s for (a) the bare slope and (b) the rooted slope with $m_r^{\text{ini}} = 1.29\%$.

Displacement histories of three surface material points, near the crest, at mid-face, and above the toe, are compared in Figure 4.7. The sequence in which these points mobilize distinguishes the two failure mechanisms. In the bare slope, the toe moves first, the mid-face follows, and the crest joins last, the signature of a retrogressive slide that begins at the toe and works upslope. Rooted slopes behave differently. All three points start moving together and travel as a single block, so the upper slope participates from the beginning instead of being undermined.

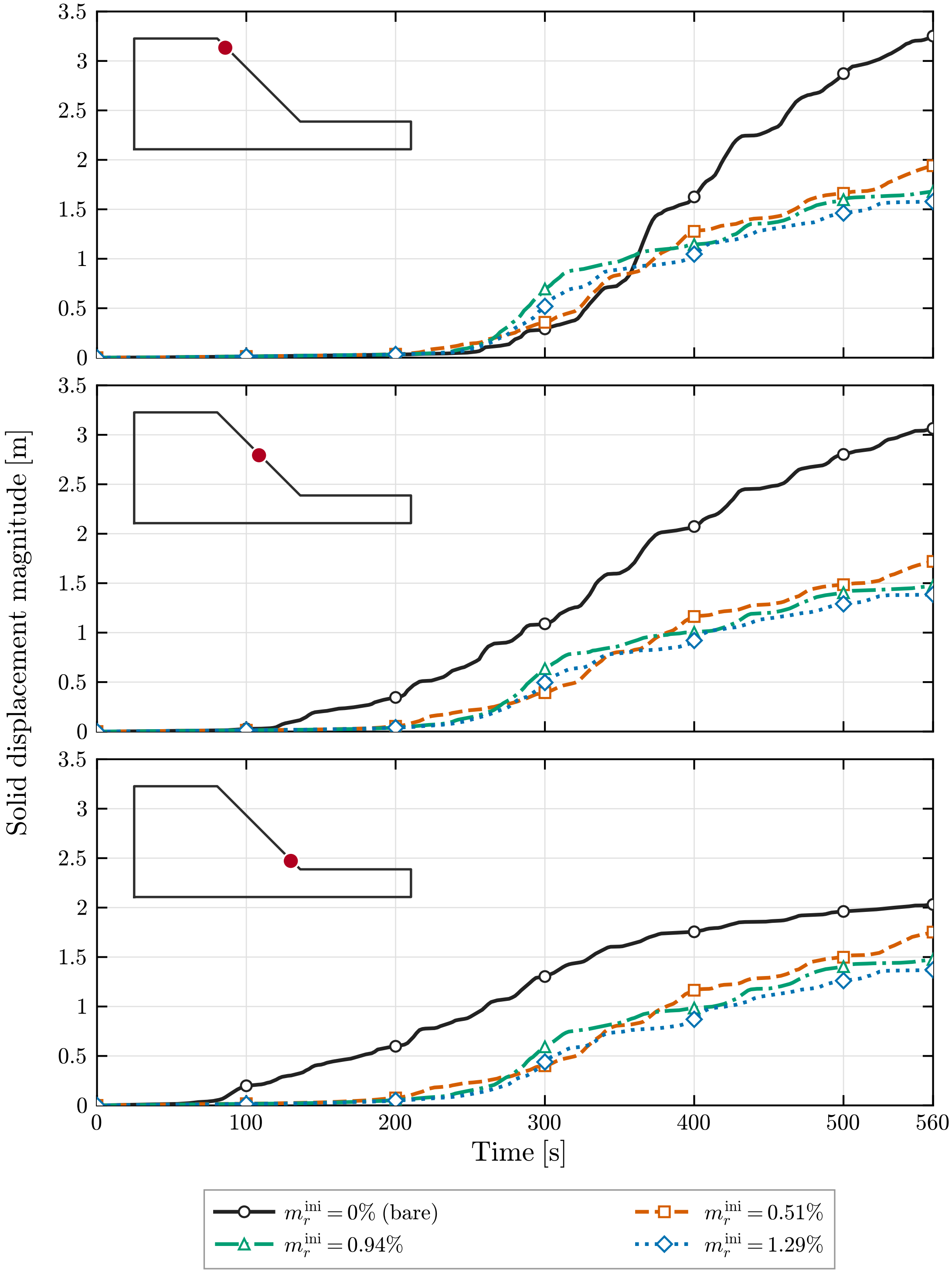

Figure 4.7: Displacement histories for the bare slope and three root mass fractions. Insets identify the monitored material points.

Root content also controls how much the slope moves. Increasing biomass roughly halves the displacement of the upper slope, with a smaller reduction near the toe, so the benefit concentrates in the upper moving mass. This gain develops even though the rooted layer is slightly more conductive, meaning the mechanical reinforcement outweighs the small hydraulic contrast.

Contours of deviatoric strain in Figures 4.8 to 4.11 show where deformation localizes in each case. All slopes are essentially undeformed when rainfall starts. By 200 s, shear strain has concentrated near the toe of the bare slope and its lower face has failed, while the rooted faces show no localization yet. At later times, failure of the bare slope propagates from the toe toward the crest, and shear strain spreads through the entire moving mass. Rooted slopes fail differently. Strain localizes in a continuous shear band at the base of the sliding mass, and the material above this band translates with little internal deformation. Nevertheless, every case eventually undergoes large movement and reaches a runout distance of about 2 m beyond the original toe. Roots in these analyses therefore delay the onset of movement, keep the sliding mass intact, and reduce its displacement, but they do not prevent failure under continued rainfall.

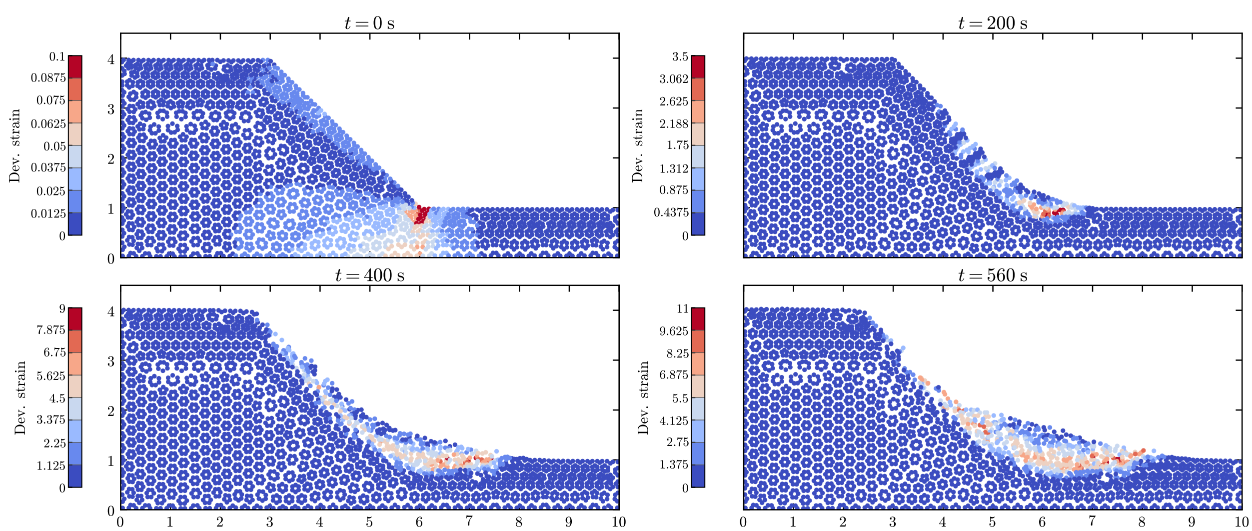

Figure 4.8: Deviatoric strain in the bare slope at $t = 0$, 200, 400, and 560 s.

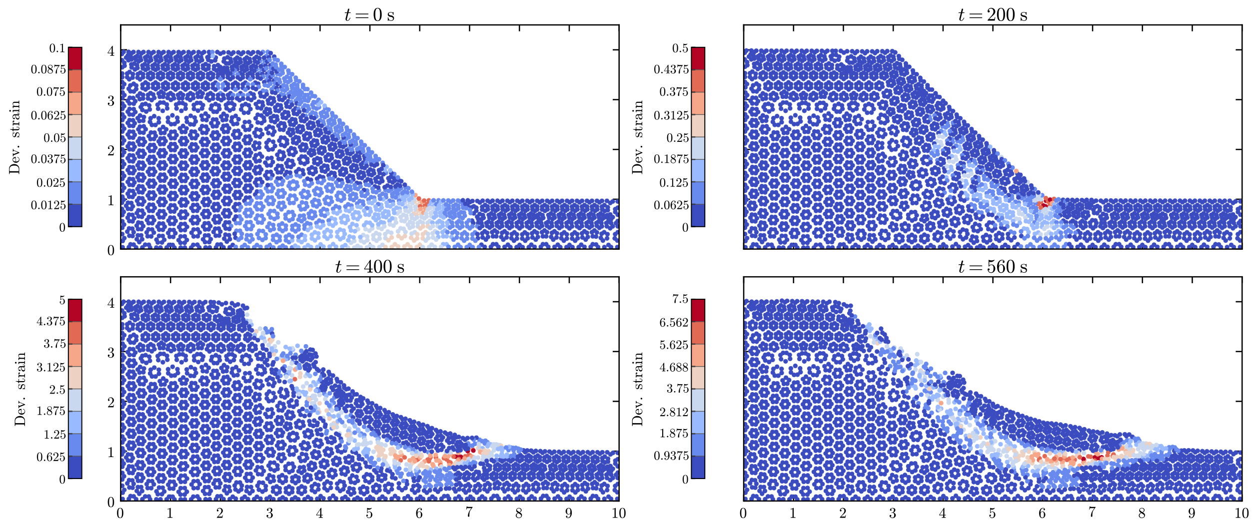

Figure 4.9: Deviatoric strain in the rooted slope with $m_r^{\text{ini}} = 0.51\%$ at $t = 0$, 200, 400, and 560 s.

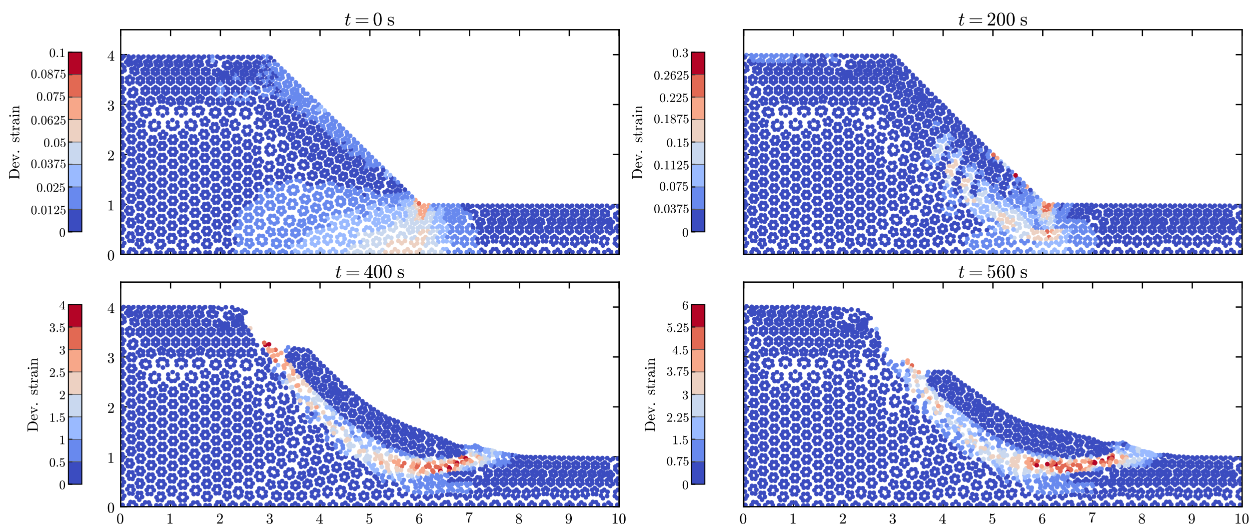

Figure 4.10: Deviatoric strain in the rooted slope with $m_r^{\text{ini}} = 0.94\%$ at $t = 0$, 200, 400, and 560 s.

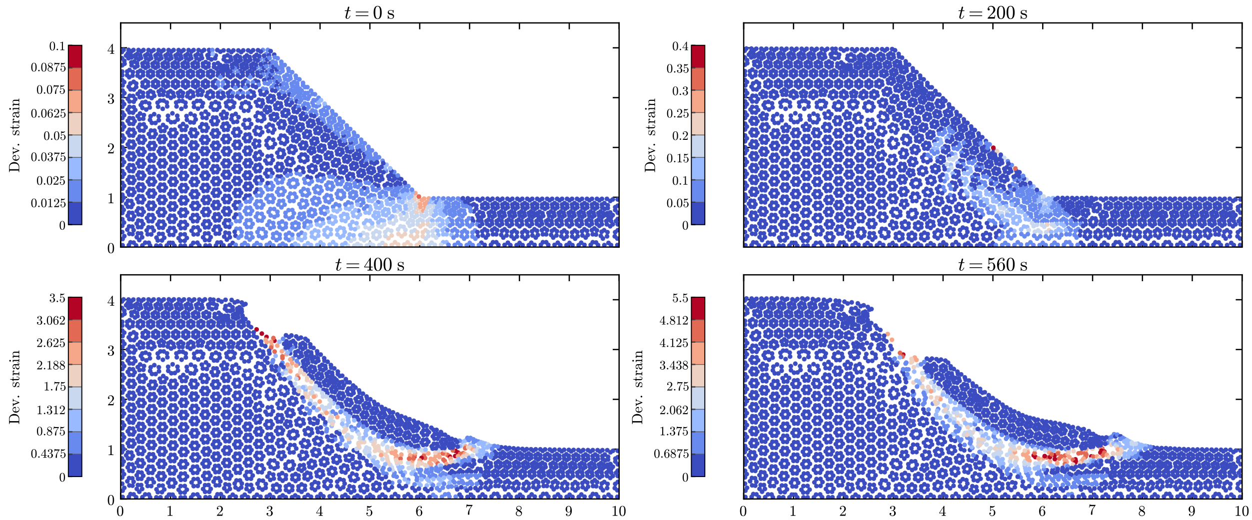

Figure 4.11: Deviatoric strain in the rooted slope with $m_r^{\mathrm{ini}} = 1.29\%$ at $t = 0$, 200, 400, and 560 s.

4.5 MPM Simulation of a Centrifuge Slope Test

This section presents a coupled MPM analysis of the centrifuge slope tests reported by Sonnenberg et al. (2010, 2012), in which instability was induced by raising the water table within a compacted model slope in stages. Analysis proceeds in two steps. First, the unreinforced test is reproduced using the reported geometry, initial state, and water-level history. A rooted slope is then simulated with the same geometry and hydraulic loading, using the soil–root formulation of Section 4.2, to examine how reinforcement changes the response. Reinforced tests with discrete wooden and rubber root analogues are not reproduced directly, since the continuum formulation represents rooted soil as a homogenized mixture and the reported root area ratio has no direct mass-fraction equivalent.

4.5.1 Experimental Setup

Figure 4.12 shows the geometry and instrumentation of the unreinforced model. A 400-mm-high slope inclined at 45° was built inside an 800-mm-long strongbox, with the upstream water level imposed through a gravel drain behind the crest and a toe drain defining the downstream boundary. Testing at $15g$ reproduces prototype stresses at one-fifteenth scale, so the model represents a 6-m-high prototype slope, and seepage durations scale by $15^2 = 225$.

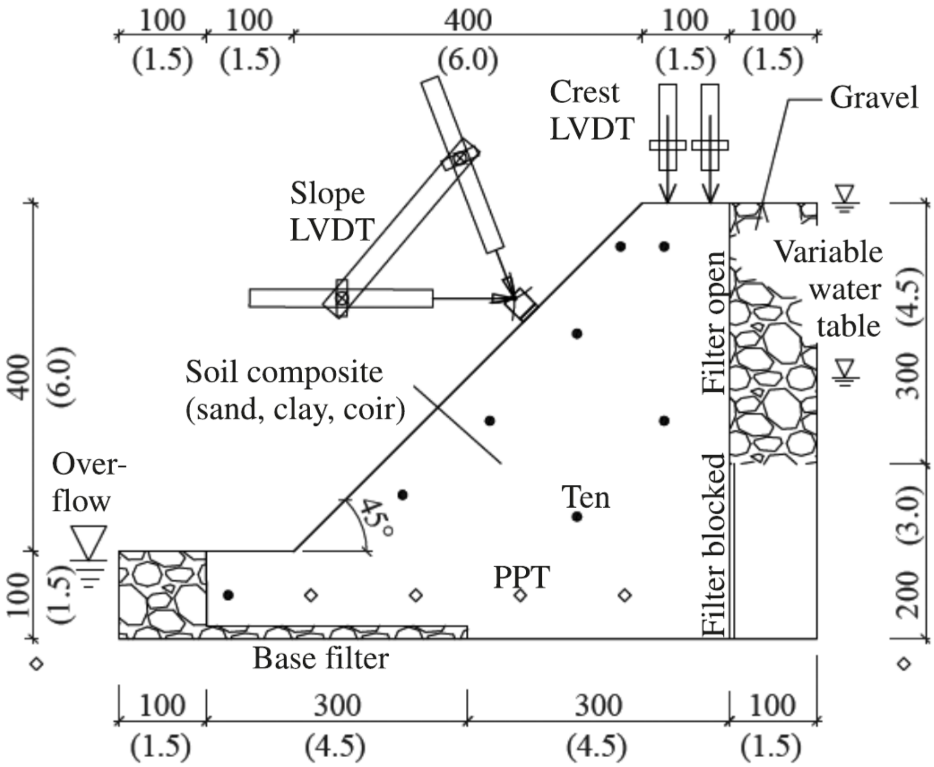

Figure 4.12: Geometry and instrumentation of the unreinforced centrifuge test (reprinted from Sonnenberg et al. (2010) with permission of Canadian Science Publishing). Dimensions are in millimetres at model scale, with prototype values in metres in parentheses.

The soil is composed of 77.5% fine silica sand, 20.0% calcium montmorillonite, and 2.5% milled coir by dry mass, mixed at a water content of about 28% and compacted in 35-mm lifts at 115 kJ/m^3 to a dry density of 1.24 Mg/m^3. With $G_s = 2.65$, these values give an initial void ratio $e_0 = G_s\rho_w/\rho_d - 1 \approx 1.14$, a porosity of 0.53, and an initial saturation of 0.65. Drained direct-shear tests gave $\phi' = 24°$ and $c' = 2$ kPa, equivalent to a critical-state ratio $M_0 \approx 0.94$ in triaxial compression, and consolidation testing indicated a saturated conductivity of 1.5×10^{-8} m/s.

Loading followed a staged procedure. After spin-up to $15g$, the upstream level was raised in 100-mm increments, each held until pore pressures stabilized, until the slope failed. Pore pressures were recorded by four base transducers, A to D, and surface movement by displacement transducers and image analysis.

No compression or swelling tests were reported, and neither were elastic stiffness, preconsolidation state, retention properties, or an initial suction field. These gaps shape the parameter selection described next.

4.5.2 Numerical Model and Material Parameters

Figure 4.13 shows the geometry, computational grid, and boundary conditions of the model. Dimensions are at model scale, and gravity is raised to $15g$ as in the test. The grid consists of 934 triangular elements with a median size of 32 mm. Slope material occupies 501 elements, each carrying three material points, and the remaining elements leave room for large deformation after failure.

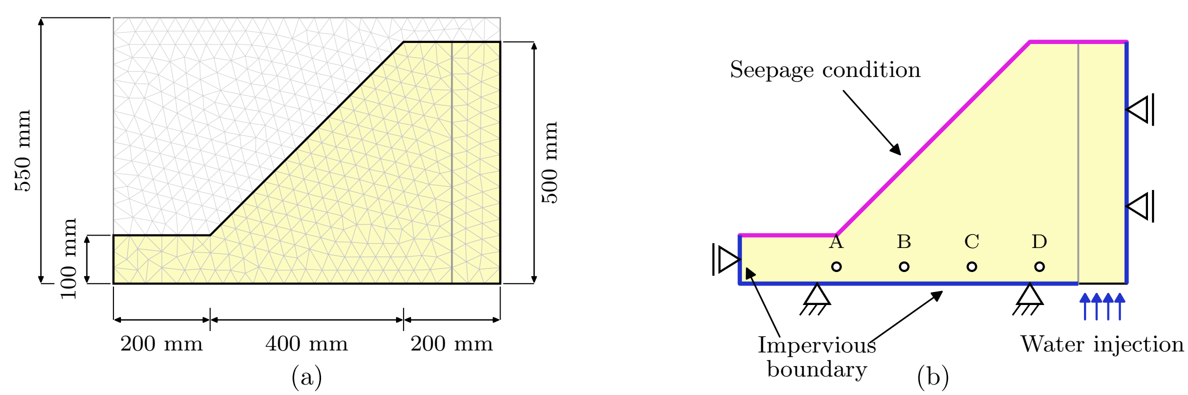

Figure 4.13: Numerical model of the unreinforced centrifuge test. (a) Computational grid and dimensions at model scale. (b) Boundary conditions, water-injection location, and pore-pressure transducer positions.

Boundary conditions follow the test configuration. Displacements are fixed in both directions along the base and in the normal direction along the lateral boundaries, and these fixities hold throughout the calculation. All outer boundaries are initially impervious. Injection is then activated along the base segment beneath the inlet column, $700 \leq x \leq 800$ mm, where liquid pressure is prescribed, while every other boundary remains impervious. A seepage condition on the free surface permits outflow only where computed pore pressure becomes compressive. Physical drains are consequently not discretized, since a drain imposes a head and prescribing that head reproduces its function directly.

One set of material parameters describes the whole domain, including the gravel column footprint. Di Carluccio et al. (2025) adopted this simplification in an MPM analysis of a comparable centrifuge test, arguing that the column has a limited mechanical effect while its role is hydraulic. Two consequences are anticipated. Nothing arrests retrogression at the column face, and computed pressures near the omitted thin base drainage layer can run high.

Matching measured pore pressures is not straightforward in the coupled formulation. Pore pressure is not a primary unknown of the velocity-based scheme, so measured records cannot be imposed as essential boundary conditions. Prescribed values enter as tractions on the liquid phase, and the resulting field continues to evolve as water diffuses and the soil deforms. Each stage is therefore held until pressures approach a steady state, and agreement with the measurements is assessed afterward.

Loading mirrors the staged procedure of the test. Spin-up establishes equilibrium under the measured initial water table, which rises from 78 mm above the base at the toe to 118 mm at the upstream wall. Injection then proceeds through the baseline level and four raises, with prescribed pressures of 17.7, 43.0, 50.6, 64.5, and 74.5 kPa, all quoted as positive in compression here and in the comparisons that follow. The first value is hydrostatic for the 0.12-m baseline level. Raised values carry a single factor of 1.35, calibrated once at the first raise and held constant, which represents head loss between the supply standpipe and the slope base.

Saturated conductivity is increased by four orders of magnitude, from the measured 1.5×10^{-8} m/s to 1.5×10^{-4} m/s, because explicit two-phase analysis at the measured value would require prohibitive durations. Wetting is correspondingly faster, and the model is compared with the experiment at matching water levels rather than matching times, as in Di Carluccio et al. (2025). Mass scaling of 100 and local damping of 0.05 during spin-up and 0.02 during injection accelerate convergence to the quasi-static state of each stage.

Material parameters are listed in Tables 4.4 and 4.5. The measured density of solid grains and initial void ratio are used directly, while $M_0 = 0.94$ is obtained from the measured friction angle. Poisson's ratio is taken as 0.30. In a comparable centrifuge analysis, Di Carluccio et al. (2025) calibrated suction-dependent compressibility against the measured settlement of a confined soil column during wetting. No equivalent settlement record or compression and swelling data were reported for the present test, so the same procedure could not be used. The reported coefficient of consolidation and saturated conductivity constrain the one-dimensional compressibility through $m_v = k_s/(c_v \gamma_w)$, but do not uniquely determine the Cam-clay parameters. Consequently, $\lambda = 0.15$ is adopted and $\kappa = 0.0225$ is taken as 0.15λ. A preconsolidation ratio of $R_0 = 2.5$ is used, based on the response during spin-up and the baseline stage.

No SWRC measurements were reported. The value $S_{min} = 0.60$ was selected slightly below the measured initial saturation of $S_w = 0.65$, while $p_{ref} = 8.5$ kPa and $\lambda_{VG} = 0.43$ were assumed. Unsaturated hydraulic conductivity follows the exponential law of Hillel (1971),

$$k = k_s \, S_w^r \tag{4.17}$$

where $r = 2.3$. Root parameters in Table 4.4 apply only to the simulation with root reinforcement. They have no effect in the unreinforced analysis because $m_r^{\mathrm{ini}} = 0$.

4.5.3 MPM Simulation Results

Figure 4.14 compares the computed failure sequence of the unreinforced slope with the centrifuge photographs. Deformation first concentrates near the toe during the hold at the third

Parameter	Description	Value
ρ_s	Density of solid grains [kg/m^3]	2650
ν	Poisson's ratio [–]	0.30
e_0	Initial void ratio [–]	1.14
R_0	Preconsolidation ratio [–]	2.5
λ	Plastic compressibility [–]	0.15
κ	Elastic compressibility [–]	0.0225
M_0	Slope of the critical-state line [–]	0.94
b	Parameter for partial saturation [–]	14
R_p	Root characteristic parameter [–]	0.4
R_a	Root parameter [–]	0.18
m_r^{ini}	Initial root content [%]	0 / 0.5

Table 4.4: Mechanical and root parameters for the centrifuge slope analysis.

Hydraulic property	Description	Value
ρ_w	Density of water [kg/m^3]	1000
K_w	Bulk modulus of water [kPa]	45000
μ_d	Dynamic viscosity [kPa·s]	1×10^{-6}
S_{min}	Minimum saturation [–]	0.60
S_{max}	Maximum saturation [–]	1.0
p_{ref}	SWRC parameter [kPa]	8.5
λ_{VG}	SWRC parameter [–]	0.43
k_s	Saturated conductivity [m/s]	1.5×10^{-4}
r	Hillel conductivity exponent [–]	2.3

Table 4.5: Hydraulic parameters for the centrifuge slope analysis.

water level. Shortly after the fourth raise, the first block releases from the lower slope, followed by two further blocks that develop progressively upslope. Consistency is evident across all three snapshots: the computed displacement and deviatoric-strain fields reproduce the three-block sequence, its toe-to-crest progression, and the accumulation of displaced soil at the toe. This correspondence shows that the calculation captures the observed retrogressive mechanism rather than only the final configuration.

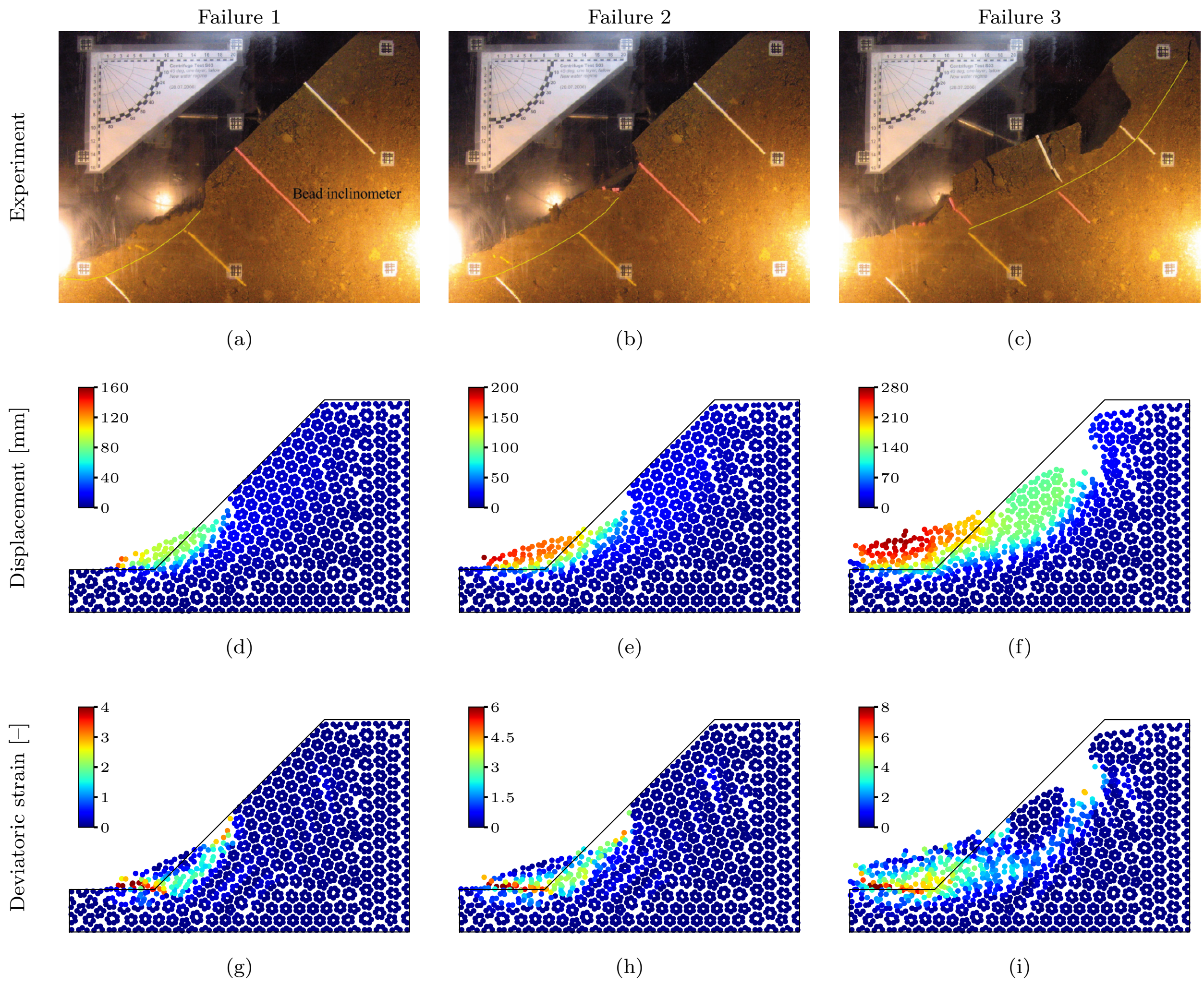

Figure 4.14: Failure sequence of the unreinforced slope. (a–c) Snapshots of the three successive block failures (reprinted from Sonnenberg et al. (2010) with permission of Canadian Science Publishing). MPM results at the corresponding states: (d–f) displacement and (g–i) deviatoric strain.

Measured and computed pore-water pressures are compared in Table 4.6 for the initial

	Measured				Computed			
	A	B	C	D	A	B	C	D
Initial	7.0	8.0	12.0	12.5	10.5	12.1	13.4	13.8
Rise 1	8.0	9.75	20.5	26.5	12.1	17.4	22.2	26.7
Rise 2	8.25	10.75	24.75	32.15	12.8	20.0	26.4	32.2
Rise 3	8.75	14.25	32.75	42.75	13.6	22.6	31.2	40.1
Rise 4	8.9	15.6	37.6	50.0	25.9	32.2	38.3	47.3
Failure	9.1	15.1	32.2	43.6	16.6	24.2	32.7	43.6

Table 4.6: Measured and computed pore-water pressures [kPa] at pore-pressure transducers A to D at the initial water level, after each of the four water-table rises, and at failure.

condition, the four water-level raises, and failure. Values at C and D remain close to the measurements throughout the loading sequence. At failure, the computed pressure at C is 32.7 kPa compared with the measured 32.2 kPa, while D reproduces the measured 43.6 kPa exactly. By contrast, the higher computed values at A and B are consistent with omission of the thin drainage layer along the base of the physical model, as anticipated in Section 4.5.2. Despite this localized overprediction, failure occurs at the same loading stage as in the experiment, immediately after the fourth raise. Because conductivity was increased to accelerate the calculation, the comparison emphasizes the hydraulic state at failure rather than the elapsed time to failure.

Root reinforcement is introduced by assigning the soil–root formulation to the surface layer shown in Figure 4.15(a). By the end of the analysis, deviatoric strain localizes along a shear surface beneath the rooted layer, as shown in Figure 4.15(b). A similar tendency was reported in the reinforced centrifuge tests, where an emerging second shear plane appeared likely to pass beneath the roots (Sonnenberg et al., 2012).

Figure 4.16 compares displacement of the monitored point near the toe for the fallow and rooted slopes. Movement of the fallow slope begins immediately after the fourth raise and stabilizes near 245 mm. For the rooted slope, movement starts about 25 s later on

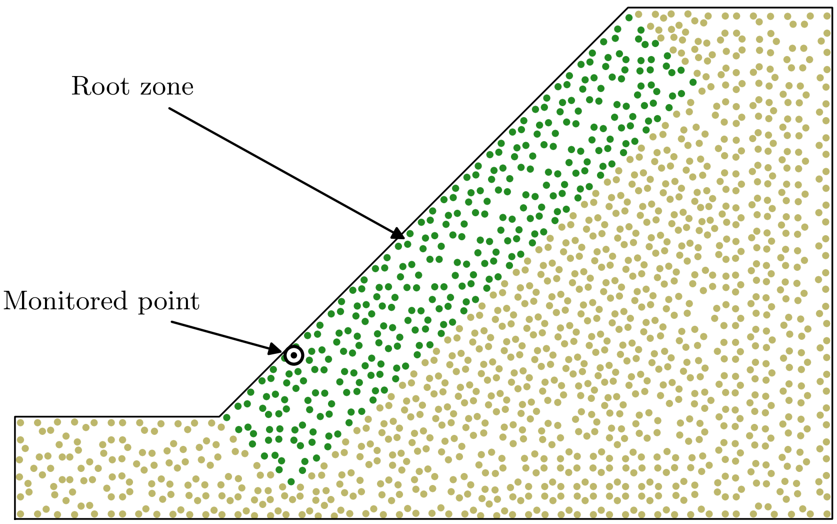

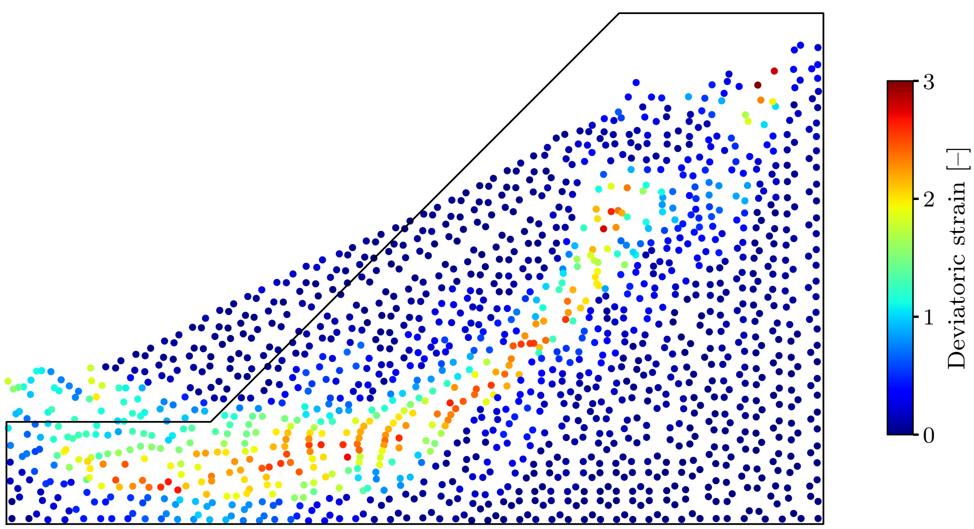

Figure 4.15: Rooted slope model. (a) Root zone and the monitored material point near the slope toe. (b) Deviatoric strain at the end of the analysis.

the accelerated numerical time scale, increases more gradually, and stabilizes near 135 mm. Together, the strain and displacement results show that, with continuum reinforcement, localization develops beneath the reinforced layer, movement begins later at the monitored point, and final displacement is roughly half that of the fallow slope.

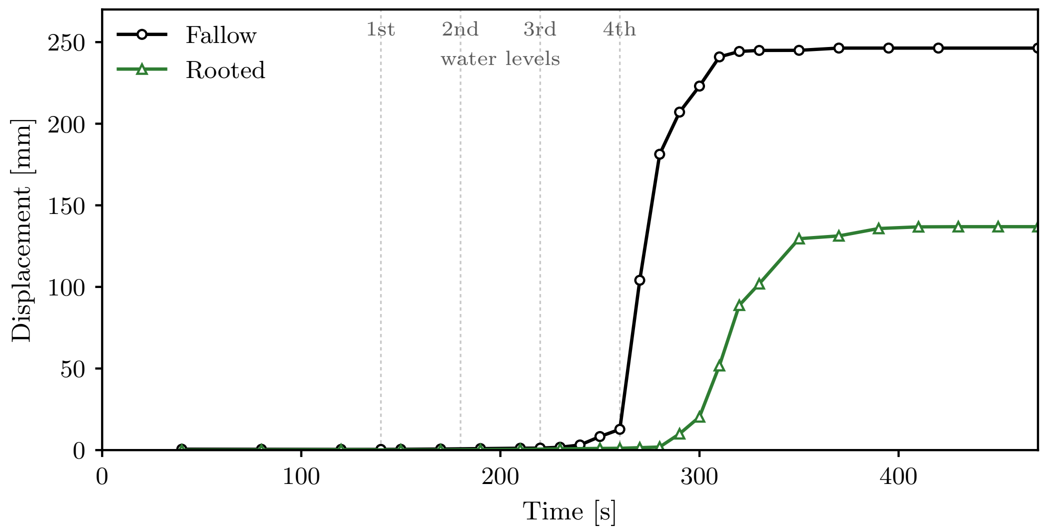

Figure 4.16: Displacement magnitude of the monitored material point near the slope toe (Figure 4.15a) for the fallow and rooted slopes; dashed lines mark the four water-table rises.

4.6 Summary

This chapter implemented the multiple-hardening rooted-soil model of Świtała et al. (2018) as a UMAT within the fully coupled two-phase MPM formulation in Anura3D. In the homogenized soil–root continuum, reinforcement increases the critical-state stress ratio and contributes additional hardening that develops with root activation strain, while partial saturation provides a separate hydraulic-hardening mechanism. Single-element analyses reproduced the reference drained and undrained triaxial simulations of Świtała et al. (2019). Validation against tests on woody-root-reinforced loess (Alam et al., 2022) also captured the increase in strength with biomass at three confining pressures. A remaining limitation is that the modified Cam-clay formulation cannot reproduce a response that is both contractive and strain softening.

Application to an idealized slope under sustained rainfall compared a bare slope with three root mass fractions using the herbaceous-root data of Kang et al. (2026). Increasing root content delayed movement, reduced upper-slope displacement by roughly one-half, and changed toe-initiated retrogression into movement of a more coherent mass above a localized basal shear band. Continued infiltration eventually produced large movement in every case and similar final runout. Root reinforcement therefore delayed and contained deformation without preventing failure under sustained wetting.

A second application considered the unreinforced centrifuge slope subjected to staged increases in water level. The coupled MPM analysis consistently reproduced the observed toe-initiated sequence of three block failures and the accumulation of displaced soil at the toe. Computed pore-water pressures at transducers C and D remained close to the measurements and reproduced the hydraulic state at failure. With a rooted surface layer, the shear surface developed beneath the reinforced zone, movement began later at the monitored toe point, and final displacement decreased from approximately 245 to 135 mm. The shift in shear localization is qualitatively consistent with observations from the discrete-root centrifuge tests. Because hydraulic response was accelerated in both slope applications, reported times are interpreted comparatively rather than as field predictions.

Chapter 5

Conclusion

5.1 Summary and Principal Findings

This dissertation examined the Material Point Method for the analysis of slope failures. The method was first evaluated for the stability of dry and unsaturated slopes through the strength reduction technique. It was then applied to the effect of vegetation on the initiation and runout of rainfall-induced failures. Starting from the governing balance laws of poromechanics, the one-phase and coupled two-phase formulations were developed, implemented, and assessed through problems of increasing difficulty, from classical benchmarks to the failure of root-reinforced slopes. The principal findings are summarized below.

First, the coupled two-phase formulation reproduces the fundamental response of saturated porous media. Undrained wave-propagation and Terzaghi consolidation benchmarks agreed closely with analytical solutions, providing a verified basis for the slope-scale analyses.

Second, MPM is a capable tool for slope stability analysis, not only for post-failure dynamics. Slip surfaces obtained with the strength reduction technique matched finite element solutions for dry and unsaturated slopes, and factors of safety of 1.58 and 1.28 fell within about ten percent of the finite element values, the difference reflecting the criteria by which each method identifies failure. Because MPM does not suffer the mesh entanglement that halts FEM once a slip surface forms, the same model that locates the onset of failure also follows the subsequent large deformation.

Third, vegetation reinforcement can be represented within this coupled framework. A multiple-hardening Cam-clay model for root-reinforced soil was implemented as a user-material subroutine, verified against published numerical triaxial results, and validated against drained triaxial tests on root-reinforced loess, reproducing the measured strength gain most accurately at the low confining stresses that characterize shallow failures.

Applied to an idealized slope under rainfall, the model showed that roots delay the onset of failure, roughly halve the displacement of the upper slope, and change the failure from a retrogressive slide beginning at the toe to the sliding of a single intact block. Under continued rainfall, however, reinforcement did not prevent failure, and the final deposit extent was comparable in all cases, showing that vegetation delays failure and limits deformation rather than guaranteeing stability.

Finally, validation against a documented centrifuge test strengthened these findings. The coupled model reproduced the observed toe-first retrogressive block failure of the unreinforced slope, with failure occurring at the correct point of the loading history and at the measured pore pressures. A rooted counterpart delayed failure, roughly halved the movement near the toe, and pushed the shear surface beneath the reinforced layer, consistent with observations from the reinforced tests. Taken together, these results establish MPM as a single framework spanning slope stability and post-failure runout, and provide a physically based route to including vegetation in the analysis of rainfall-induced landslides.

5.2 Limitations and Future Work

Several limitations qualify these findings. Explicit time integration is well suited to dynamic post-failure simulation but computationally demanding in the quasi-static regime. Slope analyses in Chapter 3 assumed steady-state seepage, whereas many failures are driven by transient infiltration. The rooted-soil model treats the composite as a homogenized continuum, which suits finely and densely rooted soils but does not resolve root architecture, root growth, or evapotranspiration. Surface runoff is not accounted for, and all rainfall is assumed to infiltrate the soil.

These limitations point to clear directions. Numerically, implicit time integration and GPU-based computing would reduce the cost of the pre-failure regime. Physically, transient infiltration would allow specific storm histories to be simulated, and enriching the rooted-soil model with root growth, decay, and evapotranspiration would capture the seasonal evolution of reinforcement. Extending the analyses to three dimensions and to instrumented field slopes would further test the framework against field observations.

Beyond these extensions, vegetation-based slope protection is a growing area of practice. Living plants offer a low-cost, sustainable alternative to hard engineering measures, and interest in such nature-based solutions is rising as rainfall-induced landslides become more frequent under a changing climate (DiBiagio et al., 2024; Stokes et al., 2009). Physically based tools that quantify how much reinforcement a planting provides, and how a vegetated slope behaves once it fails, are needed to move this practice from empirical rules toward rational design.

One promising application lies in southwestern Saudi Arabia. Mountainous terrain in the Asir and Jizan regions experiences recurrent rainfall-induced landslides (Youssef & Pourghasemi, 2021), and rapid expansion of roads and infrastructure through these highlands has increased susceptibility (Alqadhi et al., 2024). Slopes there are natural candidates for vegetation-based stabilization, and the framework developed in this dissertation offers a means to quantify the protection a given planting supplies and to assess how a vegetated slope behaves if it fails.

Bibliography

Abe, K., Soga, K., and Bandara, S. (2014). Material Point Method for Coupled Hydromechanical Problems. *Journal of Geotechnical and Geoenvironmental Engineering*, *140*(3), 04013033. https://doi.org/10.1061/(ASCE)GT.1943-5606.0001011

Alam, M., Jiang, Y.-J., Umar, M., Su, L.-j., Rahman, M., and Ullah, F. (2022). Influence of drainage and root biomass on soil mechanical behavior in triaxial tests. *Acta Geotechnica*, *17*(7), 2875–2893. https://doi.org/10.1007/s11440-021-01380-w

Al-Kafaji, I. K. J. (2013). *Formulation of a dynamic material point method (MPM) for geomechanical problems*. PhD thesis, University of Stuttgart.

Alonso, E. E., Gens, A., and Josa, A. (1990). A constitutive model for partially saturated soils. *Géotechnique*, *40*(3), 405–430. https://doi.org/10.1680/geot.1990.40.3.405

Alqadhi, S., Mallick, J., Hang, H. T., Al Asmari, A. F. S., and Kumari, R. (2024). Evaluating the influence of road construction on landslide susceptibility in Saudi Arabia's mountainous terrain. *Environmental Science and Pollution Research*, *31*. https://doi.org/10.1007/s11356-023-31352-4

Anand, L., and Govindjee, S. (2020). *Continuum Mechanics of Solids*. Oxford University Press.

Anura3D MPM Research Community. (2025). *Anura3D Version 2025 Source Code*.

Bandara, S., and Soga, K. (2015). Coupling of soil deformation and pore fluid flow using material point method. *Computers and Geotechnics*, *63*, 199–214. https://doi.org/10.1016/j.compgeo.2014.09.009

Bardenhagen, S. (2002). Energy Conservation Error in the Material Point Method for Solid Mechanics. *Journal of Computational Physics*, *180*(1), 383–403. https://doi.org/10.1006/jcph.2002.7103

Beuth, L., Wieckowski, Z., and Vermeer, P. A. (2011). Solution of quasi-static large-strain problems by the material point method. *International Journal for Numerical and Analytical Methods in Geomechanics*, *35*(13), 1451–1465. https://doi.org/10.1002/nag.965

Biot, M. A. (1956a). Theory of Propagation of Elastic Waves in a Fluid-Saturated Porous Solid. I. Low-Frequency Range. *The Journal of the Acoustical Society of America*, *28*(2), 168–178. https://doi.org/10.1121/1.1908239

Biot, M. A. (1956b). Theory of Propagation of Elastic Waves in a Fluid-Saturated Porous Solid. II. Higher Frequency Range. *The Journal of the Acoustical Society of America*, *28*(2), 179–191. https://doi.org/10.1121/1.1908241

Bishop, A. W. (1955). The use of the Slip Circle in the Stability Analysis of Slopes. *Géotechnique*, *5*(1), 7–17. https://doi.org/10.1680/geot.1955.5.1.7

Bonet, J., and Wood, R. D. (2008). *Nonlinear Continuum Mechanics for Finite Element Analysis* (2nd ed.). Cambridge University Press.

Borja, R. I., and Lee, S. R. (1990). Cam-clay plasticity, part I: Implicit integration of elasto-plastic constitutive relations. *Computer Methods in Applied Mechanics and Engineering*, *78*(1), 49–72. https://doi.org/10.1016/0045-7825(90)90152-C

Brackbill, J., Kothe, D., and Ruppel, H. (1988). Flip: A low-dissipation, particle-in-cell method for fluid flow. *Computer Physics Communications*, *48*(1), 25–38. https://doi.org/10.1016/0010-4655(88)90020-3

Burgess, D., Sulsky, D., and Brackbill, J. U. (1992). Mass matrix formulation of the FLIP particle-in-cell method. *Journal of Computational Physics*, *103*(1), 1–15. https://doi.org/10.1016/0021-9991(92)90323-Q

Ceccato, F. (2015). *Study of large deformation geomechanical problems with the Material Point Method* [PhD thesis]. University of Padova. http://paduaresearch.cab.unipd.it/7478/

Ceccato, F., and Simonini, P. (2019). Numerical Features Used in Simulations. In J. Fern, A. Rohe, K. Soga, and E. Alonso (Eds.), *The Material Point Method for Geotechnical Engineering* (1st ed., pp. 101–124). CRC Press. https://doi.org/10.1201/9780429028090-6

Ceccato, F., Yerro, A., and Di Carluccio, G. (2024). Simulating landslides with the material point method: Best practices, potentialities, and challenges. *Engineering Geology*, *338*, 107614. https://doi.org/10.1016/j.enggeo.2024.107614

Ceccato, F., Yerro, A., Girardi, V., and Simonini, P. (2021). Two-phase dynamic MPM formulation for unsaturated soil. *Computers and Geotechnics*, *129*, 103876. https://doi.org/10.1016/j.compgeo.2020.103876

Cheng, Y., Lansivaara, T., and Wei, W. (2007). Two-dimensional slope stability analysis by limit equilibrium and strength reduction methods. *Computers and Geotechnics*, *34*(3), 137–150. https://doi.org/10.1016/j.compgeo.2006.10.011

Chiu, C. F., and Ng, C. W. W. (2003). A state-dependent elasto-plastic model for saturated and unsaturated soils. *Géotechnique*, *53*(9), 809–829. https://doi.org/10.1680/geot.2003.53.9.809

Courant, R., Friedrichs, K., and Lewy, H. (1928). Über die partiellen Differenzengleichungen der mathematischen Physik. *Mathematische Annalen*, *100*(1), 32–74. https://doi.org/10.1007/BF01448839

Cuomo, S., Di Perna, A., Moscariello, M., and Martinelli, M. (2024). Possible remediation of impact-loading debris avalanches via fine long rooted grass: An experimental and material point method (MPM) analysis. *Landslides*, *21*(4), 679–696. https://doi.org/10.1007/s10346-023-02178-5

Dawson, E. M., Roth, W. H., and Drescher, A. (1999). Slope stability analysis by strength reduction. *Géotechnique*, *49*(6), 835–840. https://doi.org/10.1680/geot.1999.49.6.835

de Boer, R. (1996). Highlights in the Historical Development of the Porous Media Theory: Toward a Consistent Macroscopic Theory. *Applied Mechanics Reviews*, *49*(4), 201–262. https://doi.org/10.1115/1.3101926

De Boer, R., and Kowalski, S. J. (1983). A plasticity theory for fluid-saturated porous solids. *International Journal of Engineering Science*, *21*(11), 1343–1357. https://doi.org/10.1016/0020-7225(83)90132-5

Detournay, C., and Dzik, E. (2006). Nodal mixed discretization for tetrahedral elements [Paper 07-02]. *Proceedings of the 4th International FLAC Symposium on Numerical Modeling in Geomechanics*.

Di Carluccio, G., Aviles, L. A., Pinyol, N. M., and Alonso, E. E. (2025). Modelling wetting collapse, failure and deposition of an unsaturated slope with material point method. *International Journal for Numerical and Analytical Methods in Geomechanics*, *49*, 4526–4551. https://doi.org/10.1002/nag.70075

DiBiagio, A., Capobianco, V., Oen, A., and Tallaksen, L. M. (2024). State-of-the-art: Parametrization of hydrological and mechanical reinforcement effects of vegetation in slope stability models for shallow landslides. *Landslides*, *21*(10), 2417–2446. https://doi.org/10.1007/s10346-024-02300-1

Fellenius, W. (1936). Calculation of the stability of earth dams. *Proc. of the Second Congress on Large Dams*, *4*, 445–463.

Feng, Z.-K., and Xu, W.-J. (2021). GPU material point method (MPM) and its application on slope stability analysis. *Bulletin of Engineering Geology and the Environment*, *80*, 5437–5449. https://doi.org/10.1007/s10064-021-02265-8

Froude, M. J., and Petley, D. N. (2018). Global fatal landslide occurrence from 2004 to 2016. *Natural Hazards and Earth System Sciences*, *18*(8), 2161–2181. https://doi.org/10.5194/nhess-18-2161-2018

Gens, A., Sánchez, M., and Sheng, D. (2006). On constitutive modelling of unsaturated soils. *Acta Geotechnica*, *1*(3), 137–147. https://doi.org/10.1007/s11440-006-0013-9

Girardi, V., Yerro, A., Ceccato, F., and Simonini, P. (2021). Modelling deformations in water retention structures with unsaturated material point method. *Proceedings of the Institution of Civil Engineers - Geotechnical Engineering*, *174*(5), 577–592. https://doi.org/10.1680/jgeen.21.00059

Griffiths, D. V., and Lane, P. A. (1999). Slope stability analysis by finite elements. *Géotechnique*, *49*(3), 387–403. https://doi.org/10.1680/geot.1999.49.3.387

Haque, U., da Silva, P. F., Devoli, G., Pilz, J., Zhao, B., Khaloua, A., Wilopo, W., Andersen, P., Lu, P., Lee, J., Yamamoto, T., Keellings, D., Wu, J.-H., and Glass, G. E. (2019). The human cost of global warming: Deadly landslides and their triggers (1995–2014). *Science of The Total Environment*, *682*, 673–684. https://doi.org/10.1016/j.scitotenv.2019.03.415

Hillel, D. (1971). *Soil and water: Physical principles and processes*. Academic Press.

Jeremić, B., Cheng, Z., Taiebat, M., and Dafalias, Y. (2008). Numerical simulation of fully saturated porous materials. *International Journal for Numerical and Analytical Methods in Geomechanics*, *32*(13), 1635–1660. https://doi.org/10.1002/nag.687

Jiang, Y.-J., Alam, M., Su, L.-J., Umar, M., Sadiq, S., Jia, L.-J., and Rahman, M. (2022). Effect of root orientation on the strength characteristics of loess in drained and undrained triaxial tests. *Engineering Geology*, *296*, 106459. https://doi.org/10.1016/j.enggeo.2021.106459

Kang, X., Wang, S., Zou, X., Świtała, B., and Wu, W. (2026). Hydro-mechanical response of herbaceous root-reinforced soils and its implications for vegetated-slope stability. *Engineering Geology*, *361*, 108501. https://doi.org/10.1016/j.enggeo.2025.108501

Khalili, N., and Khabbaz, M. H. (1998). A unique relationship for χ for the determination of the shear strength of unsaturated soils. *Géotechnique*, *48*(5), 681–687. https://doi.org/10.1680/geot.1998.48.5.681

Kohler, M., and Puzrin, A. M. (2022). Mechanism of co-seismic deformation of the slow-moving La Sorbella landslide in Italy revealed by MPM analysis. *Journal of Geophysical Research: Earth Surface*, *127*(7), e2022JF006618.

Lewis, R. W., and Schrefler, B. A. (1998). *The finite element method in the static and dynamic deformation and consolidation of porous media* (2nd ed.). John Wiley & Sons.

Loret, B., and Khalili, N. (2002). An effective stress elastic–plastic model for unsaturated porous media. *Mechanics of Materials*, *34*(2), 97–116. https://doi.org/10.1016/S0167-6636(01)00092-8

Macedo, J., Yerro, A., Cornejo, R., and Pierce, I. (2024). Cadia TSF Failure Assessment Considering Triggering and Posttriggering Mechanisms. *Journal of Geotechnical and Geoenvironmental Engineering*, *150*(4), 04024011. https://doi.org/10.1061/JGGEFK.GTENG-11660

Mašín, D., and Khalili, N. (2008). A hypoplastic model for mechanical response of unsaturated soils. *International Journal for Numerical and Analytical Methods in Geomechanics*, *32*(15), 1903–1926. https://doi.org/10.1002/nag.714

Matsui, T., and San, K.-C. (1992). Finite Element Slope Stability Analysis by Shear Strength Reduction Technique. *Soils and Foundations*, *32*(1), 59–70. https://doi.org/10.3208/sandf1972.32.59

Mieremet, M. M. J., Stolle, D. F., Ceccato, F., and Vuik, C. (2016). Numerical stability for modelling of dynamic two-phase interaction. *International Journal for Numerical and Analytical Methods in Geomechanics*, *40*(9), 1284–1294. https://doi.org/10.1002/nag.2483

Nairn, J. A. (2003). Material point method calculations with explicit cracks. *Computer Modeling in Engineering and Sciences*, *4*(6), 649–664.

Ng, C. W. W., Kamchoom, V., and Leung, A. K. (2016). Centrifuge modelling of the effects of root geometry on transpiration-induced suction and stability of vegetated slopes. *Landslides*, *13*(5), 925–938. https://doi.org/10.1007/s10346-015-0645-7

Ng, C. W. W., Ni, J. J., Leung, A. K., and Wang, Z. J. (2016). A new and simple water retention model for root-permeated soils. *Géotechnique Letters*, *6*(1), 106–111. https://doi.org/10.1680/jgele.15.00187

Nguyen, T. S., Yang, K.-H., Wu, Y.-K., Teng, F., Chao, W.-A., and Lee, W.-L. (2022). Post-failure process and kinematic behavior of two landslides: Case study and material point analyses. *Computers and Geotechnics*, *148*, 104797. https://doi.org/10.1016/j.compgeo.2022.104797

Ni, J. J., Leung, A. K., Ng, C. W. W., and Shao, W. (2018). Modelling hydro-mechanical reinforcements of plants to slope stability. *Computers and Geotechnics*, *95*, 99–109. https://doi.org/10.1016/j.compgeo.2017.09.001

Pinyol, N. M., Alvarado, M., Alonso, E. E., and Zabala, F. (2018). Thermal effects in landslide mobility. *Géotechnique*, *68*(6), 528–545. https://doi.org/10.1680/jgeot.17.P.054

Pollen, N., and Simon, A. (2005). Estimating the mechanical effects of riparian vegetation on stream bank stability using a fiber bundle model. *Water Resources Research*, *41*(7). https://doi.org/10.1029/2004WR003801

Schwarz, M., Cohen, D., and Or, D. (2010). Root-soil mechanical interactions during pullout and failure of root bundles. *Journal of Geophysical Research: Earth Surface*, *115*(F4). https://doi.org/10.1029/2009JF001603

Sidle, R. C., and Bogaard, T. A. (2016). Dynamic earth system and ecological controls of rainfall-initiated landslides. *Earth-Science Reviews*, *159*, 275–291. https://doi.org/10.1016/j.earscirev.2016.05.013

Soga, K., Alonso, E., Yerro, A., Kumar, K., and Bandara, S. (2016). Trends in large-deformation analysis of landslide mass movements with particular emphasis on the material point method. *Géotechnique*, *66*(3), 248–273. https://doi.org/10.1680/jgeot.15.LM.005

Sonnenberg, R., Bransby, M. F., Bengough, A. G., Hallett, P. D., and Davies, M. C. (2012). Centrifuge modelling of soil slopes containing model plant roots. *Canadian Geotechnical Journal*, *49*(1), 1–17. https://doi.org/10.1139/T11-081

Sonnenberg, R., Bransby, M. F., Hallett, P. D., Bengough, A. G., Mickovski, S. B., and Davies, M. C. (2010). Centrifuge modelling of soil slopes reinforced with vegetation. *Canadian Geotechnical Journal*, *47*(12), 1415–1430. https://doi.org/10.1139/T10-037

Spencer, E. (1967). A Method of analysis of the Stability of Embankments Assuming Parallel Inter-Slice Forces. *Géotechnique*, *17*(1), 11–26. https://doi.org/10.1680/geot.1967.17.1.11

Steffen, M., Kirby, R. M., and Berzins, M. (2008). Analysis and reduction of quadrature errors in the material point method (MPM). *International Journal for Numerical Methods in Engineering*, *76*(6), 922–948. https://doi.org/10.1002/nme.2360

Stokes, A., Atger, C., Bengough, A. G., Fourcaud, T., and Sidle, R. C. (2009). Desirable plant root traits for protecting natural and engineered slopes against landslides. *Plant and Soil*, *324*(1), 1–30. https://doi.org/10.1007/s11104-009-0159-y

Sulsky, D., Chen, Z., and Schreyer, H. L. (1994). A particle method for history-dependent materials. *Computer Methods in Applied Mechanics and Engineering*, *118*(1), 179–196. https://doi.org/10.1016/0045-7825(94)90112-0

Sulsky, D., Zhou, S.-J., and Schreyer, H. L. (1995). Application of a particle-in-cell method to solid mechanics. *Computer Physics Communications*, *87*(1–2), 236–252. https://doi.org/10.1016/0010-4655(94)00170-7

Świtała, B. M., Askarinejad, A., Wu, W., and Springman, S. M. (2018). Experimental validation of a coupled hydro-mechanical model for vegetated soil. *Géotechnique*, *68*(5), 375–385. https://doi.org/10.1680/jgeot.16.P.233

Świtała, B. M., and Wu, W. (2018). Numerical modelling of rainfall-induced instability of vegetated slopes. *Géotechnique*, *68*(6), 481–491. https://doi.org/10.1680/jgeot.16.P.176

Świtała, B. M. (2020). Numerical Simulations of Triaxial Tests on Soil-Root Composites and Extension to Practical Problem: Rainfall-Induced Landslide. *International Journal* *of Geomechanics*, *20*(11), 04020206. https://doi.org/10.1061/(ASCE)GM.1943-5622.0001845

Świtała, B. M., Wu, W., and Wang, S. (2019). Implementation of a coupled hydro-mechanical model for root-reinforced soils in finite element code. *Computers and Geotechnics*, *112*, 197–203. https://doi.org/10.1016/j.compgeo.2019.04.015

Tamagnini, R. (2004). An extended Cam-clay model for unsaturated soils with hydraulic hysteresis. *Géotechnique*, *54*(3), 223–228. https://doi.org/10.1680/geot.2004.54.3.223

Terzaghi, K. (1925). *Erdbaumechanik auf bodenphysikalischer Grundlage*. F. Deuticke.

Thomas, R. E., and Pollen-Bankhead, N. (2010). Modeling root-reinforcement with a fiber-bundle model and Monte Carlo simulation. *Ecological Engineering*, *36*(1), 47–61. https://doi.org/10.1016/j.ecoleng.2009.09.008

van Esch, J. M., Stolle, D. F. E., and Jassim, I. (2011). Finite element method for coupled dynamic flow-deformation simulation [[CHECK: page range against the COMGEO II proceedings]]. *2nd International Symposium on Computational Geomechanics (COMGEO II)*.

Verruijt, A. (2010). Dynamics of Porous Media. In A. Verruijt (Ed.), *An Introduction to Soil Dynamics* (pp. 91–112). Springer Netherlands. https://doi.org/10.1007/978-90-481-3441-0_5

Waldron, L. J. (1977). The Shear Resistance of Root-Permeated Homogeneous and Stratified Soil. *Soil Science Society of America Journal*, *41*(5), 843–849. https://doi.org/10.2136/sssaj1977.03615995004100050005x

Wang, H., Chen, R., Leung, A. K., Garg, A., and Jiang, Z. (2025). Pore-Based Modeling of Hydraulic Conductivity Function of Unsaturated Rooted Soils. *International Journal for Numerical and Analytical Methods in Geomechanics*, *49*(7), 1790–1803. https://doi.org/10.1002/nag.3958

Wang, J., Xiang, W., and Wu, Y. (2015). Study on the Seepage Field and Underground Erosion of a Loess Pipeline Foundation. *Journal of Pipeline Systems Engineering and Practice*, *6*(3), A4013001. https://doi.org/10.1061/(ASCE)PS.1949-1204.0000151

Wang, J.-H., and Xu, W.-J. (2025). Slope stability and failure dynamics of rainfall-induced landslide: Algorithm and applications. *Computers and Geotechnics*, *177*, 106919. https://doi.org/10.1016/j.compgeo.2024.106919

Wu, T. H., McKinnell III, W. P., and Swanston, D. N. (1979). Strength of tree roots and landslides on Prince of Wales Island, Alaska. *Canadian Geotechnical Journal*, *16*(1), 19–33. https://doi.org/10.1139/t79-003

Xu, Z., Li, C., Fang, F., and Wu, F. (2022). Study on the stability of soil-rock mixture slopes based on the material point strength reduction method. *Applied Sciences*, *12*(22), 11595. https://doi.org/10.3390/app122211595

Yerro, A., Alonso, E., and Pinyol, N. (2015). The material point method for unsaturated soils. *Géotechnique*, *65*(3), 201–217. https://doi.org/10.1680/geot.14.P.163

Yerro, A., Soga, K., and Bray, J. (2019). Runout evaluation of Oso landslide with the material point method. *Canadian Geotechnical Journal*, *56*(9), 1304–1317. https://doi.org/10.1139/cgj-2017-0630

Youssef, A. M., and Pourghasemi, H. R. (2021). Landslide susceptibility mapping using machine learning algorithms and comparison of their performance at Abha Basin, Asir Region, Saudi Arabia. *Geoscience Frontiers*, *12*(2), 639–655. https://doi.org/10.1016/j.gsf.2020.05.010

Zabala, F., and Alonso, E. (2011). Progressive failure of Aznalcóllar dam using the material point method. *Géotechnique*, *61*(9), 795–808. https://doi.org/10.1680/geot.9.P.134

Zhang, C.-B., Chen, L.-H., Liu, Y.-P., Ji, X.-D., and Liu, X.-P. (2010). Triaxial compression test of soil–root composites to evaluate influence of roots on soil shear strength. *Ecological Engineering*, *36*(1), 19–26. https://doi.org/10.1016/j.ecoleng.2009.09.005

Zhang, P., Liu, L.-L., Zhang, S.-H., Cheng, Y.-M., and Wang, B. (2022). Material point method-based two-dimensional cohesive-frictional slope stability analysis charts considering depth coefficient effect. *Bulletin of Engineering Geology and the Environment*, *81*, 206. https://doi.org/10.1007/s10064-022-02695-y

Zienkiewicz, O. C. (1982). Basic Formulation of Static and Dynamic Behaviour of Soil and other Porous Media. In J. B. Martins (Ed.), *Numerical Methods in Geomechanics* (pp. 39–55). Springer Netherlands. https://doi.org/10.1007/978-94-009-7895-9_2

Zienkiewicz, O. C., Chan, A. H. C., Pastor, M., Paul, D. K., and Shiomi, T. (1990). Static and Dynamic Behaviour of Soils: A Rational Approach to Quantitative Solutions. I. Fully Saturated Problems. *Proceedings of the Royal Society of London. Series A, Mathematical and Physical Sciences*, *429*(1877), 285–309. https://doi.org/10.1098/rspa.1990.0061

Zienkiewicz, O. C., Chang, C. T., and Bettess, P. (1980). Drained, undrained, consolidating and dynamic behaviour assumptions in soils. *Géotechnique*, *30*(4), 385–395. https://doi.org/10.1680/geot.1980.30.4.385

Zienkiewicz, O. C., Humpheson, C., and Lewis, R. W. (1975). Associated and non-associated visco-plasticity and plasticity in soil mechanics. *Géotechnique*, *25*(4), 671–689. https://doi.org/10.1680/geot.1975.25.4.671

Zienkiewicz, O. C., and Shiomi, T. (1984). Dynamic behaviour of saturated porous media; The generalized Biot formulation and its numerical solution. *International Journal for Numerical and Analytical Methods in Geomechanics*, *8*(1), 71–96. https://doi.org/10.1002/nag.1610080106

Zienkiewicz, O., Taylor, R., and Govindjee, S. (2025). Chapter 3 - Weak forms and approximate solutions: 1-D field problems. In *The Finite Element Method (Eighth Edition)* (pp. 29–40). Butterworth-Heinemann. https://doi.org/10.1016/B978-0-44-316044-8.00012-0

Zou, X., Li, D., Wang, S., Gu, S., and Wu, W. (2024). Instability and deformation behaviors of root-reinforced soil under constant shear stress path. *Engineering Geology*, *343*, 107762. https://doi.org/10.1016/j.enggeo.2024.107762